THE UNIVERSITY OF CHICAGO

CHEMICAL BIOLOGY APPROACHES TO STUDY AND MANIPULATE TRANSLATION AND POST-TRANSLATIONAL MODIFICATIONS

A DISSERTATION SUBMITTED TO
THE FACULTY OF THE DIVISION OF THE PHYSICAL SCIENCES
IN CANDIDACY FOR THE DEGREE OF
DOCTOR OF PHILOSOPHY

DEPARTMENT OF CHEMISTRY

BY
YANG CAO

CHICAGO, ILLINOIS
AUGUST 2023

To my beloved parents, whose hard work and sacrifices allowed me to embark on this journey. Their continuous love and support made this work possible.

TABLE OF CONTENTS

LIST OF FIGURES

LIST OF TABLES

ACKNOWLEDGEMENTS

I wish to take this opportunity to extend my appreciation to all of the people that have offered me help, guidance, kindness, hugs and love; to those who brought me food, Boba tea, laughter and happiness; and also to those who have taught me lessons, during this PhD journey. They all made it a meaningful and valuable memory.

First of all, I would like to thank my advisor Prof. Bryan Dickinson, for his guidance and supports. I always know his door is open, or slack is online, whenever help is needed. Thanks for choosing me, in the March of 2016, in the summer visiting program; and for choosing me again, in 2017, to join Dickinson Lab as a graduate student. During PhD, Bryan granted me opportunities to explore and learn about science, supported my research and personal growth, respected my decisions, and always encourage me no matter I fail or succeed. He taught me everything about academic research, from email drafting, paper writing, grant applications to pipette fixing and drilling a hole on the fridge. I will always appreciate his encouragement and support.

Pausing here, I would like to thank Prof. Chuan He, Prof. Peng Chen, Melinda Moore and all other faculties and staff who worked hard to launch that first undergraduate student rotation program between the Chemistry Department of PKU and Uchicago. It was a life-changing event for many of us. Regrettably, that program was canceled since COVID-19 happened, which is one of all the wonderful things that have been taken away by the pandemic.

I would like to express my deepest gratitude to all current and past Dickinson lab members, who truly made my PhD experience special and memorable. My first mentor is Dr. Jinyue Pu. In the summer of 2016. She warmly welcomed me to this alien country, guided me how to do experiments and live a life here. My second mentor is Dr. Rahul Kathayat, who has laid a solid foundation for research in *S*-palmitoylation, and always being helpful, encouraging, and kind. I am so fortunate to have be mentored by these

two wonderful persons and skillful scientists. I also would like to thank Dr. Simone Rauch who instructed me in RNA experiments; to Dr. Huachun Liu and Shannon Lu for working together on taRNA projects; to Daniel Ahn and Lingjie (Jason) Chen, who has worked with me as undergraduates; and to Dr. Somayeh Ahmadiantehrani for placing orders everyday and for editing all my manuscripts. Thanks to Rachel Chan, Armor Rupanaya and Sandrine Legault for all the happy weekends we shared about good foods. I also want to thank Sandrine's dogy, Daisy, for being a cute and friendly 'pet therapist'. Special thanks to my Yogurt Lunch team-members, Tong Lan and Riley Sinnott. I enjoyed all our funny conversations about science and life, cherished all the laughter we shared and deeply appreciated your supports for my life and research during hard times. Especially, thanks for taking time to read and edit this dissertation manuscript. There are so many lab members that I didn't name here, I would like to thank all of them for being supportive during my doctoral studies.

I would like to sincerely thank all of my collaborators, without whose hard work, none of the projects were possible. Thanks to Prof. Phoebe Rice who taught me everything about XRD data analysis. Thanks to Dr. Anitha Govind, Dr. Okunola Jeyifous, Dr. Christine Simmons, Dr. Mark Berney, Aleksandar Radakovic, and Runwei Yang, for their help and contributions to taRNA project.

Thanks to my neighboring lab, He lab, for all the instruments, reagents and consumables that I borrowed, and for all the members who shared precious experiment techniques with me. Thanks to Dr. Lulu Hu who taught me crystallization of proteins; to Dr. Caraline Sepich-Poore who taught me polysome profiling assay; to Dr. Fan Yang who taught me dimethyl-labeling proteomics; to Dr. Linda Zhang who shared tips and tricks about mouse experiments. Thanks to Dr. Chang Liu, Dr. Yun Gao, Dr. Yu Xiao and Dr. Xiaoyang Dou, for being encouraging and supportive friends to me.

I would like to thank my dissertation committee, Prof. Weixin Tang and Prof. Joseph

Piccirilli, for their guidance on my research and dissertation defense. Weixin has offered valuable suggestions for my project at very early stage. Graduate classes taught by Joe benefited me a lot in understanding basics in RNA and chemical biology.

At last, heartfelt thanks go to my beloved families. Thanks to my boyfriend, Bo Lei, for his caring, company, supports and love all the way since 2014. Thank him for always being there and holding my hand whatever happens. Thanks to my father and mother, who love me wholeheartedly and support all of my decisions, even that means their only child is faraway on another continent. Their love is the most precious thing in my life.

ABSTRACT

Gene expression in mammalian systems is carefully tuned through transcriptional, post-transcriptional, and translation processes. This thesis focuses on the study of one post-translational chemical mark, *S*-palmitoylation, using chemical biology approaches, and the exploitation of translation regulation for therapeutic purposes, using synthetic biology approaches. *S*-Palmitoylation is a reversible post-translational lipid modification that has been observed on mitochondrial proteins, but both the regulation and functional consequences of mitochondrial *S*-palmitoylation are poorly understood. In this thesis, we first developed new members of the fluorogenic depalmitoylation probes (DPPs), DPP-5 and mitoDPPs. The DPP-5 features improved water solubility and incorporates the natural lipid substrate for enhanced *S*-depalmitoylases selectivity. The mitoDPPs preferentially localize to mitochondria to measure the level of mitochondrial activity of depalmitoylases in live cells. Using these probes, we discovered a new depalmitoylase, ABHD10, in mitochondria, and characterized this enzyme by biochemical and structural analyses. We showed that peroxiredoxin-5 (PRDX5), a key antioxidant protein, is a target of ABHD10, and discovered that ABHD10 regulates the *S*-palmitoylation status of the nucleophilic active site residue of PRDX5, providing a direct mechanistic connection between ABHD10-mediated *S*-depalmitoylation of PRDX5 and its antioxidant capacity.

To address the therapeutic need for diseases caused by insufficient gene expression, we developed “translation-activating RNAs” (taRNAs), a bifunctional RNA-based molecular technology that binds to a specific mRNA of interest and directly upregulates its translation. We show that we can construct taRNAs from a variety of viral or mammalian RNA internal ribosome entry sites (IRESs) and demonstrate that taRNAs can activate gene expression from a suite of target mRNAs. We minimized the taRNA scaffold to 94 nucleotides, identified two translation initiation factor proteins responsible for taRNA activity, and validated the technology by amplifying SYNGAP1 expression, a target of haploinsuffi-

ciency disease, in patient-derived cells. Finally, we show that taRNAs can be delivered as RNA molecules by lipid nanoparticles (LNPs) to cell lines, primary neurons, and mouse liver in vivo. taRNAs provide a compact and general nucleic acid-based technology to upregulate protein production from endogenous mRNAs, opening up new possibilities for therapeutic RNA research.

LIST OF PUBLICATIONS BASED ON WORK IN THIS THESIS†

1. Qiu, T.*, Kathayat, R. S.*, **Cao, Y.***, Beck, M. W., and Dickinson, B. C. A fluorescent probe with improved water solubility permits the analysis of protein *S*-depalmitoylation activity in live cells. *Biochemistry*, **2018**, *57(2)*, 221-225.

2. Kathayat, R.S., **Cao, Y.**, Elvira, P.D., Sandoz, P.A., Zaballa, M.E., Springer, M.Z., Drake, L.E., Macleod, K.F., van der Goot, F.G. and Dickinson, B.C. Active and dynamic mitochondrial *S*-depalmitoylation revealed by targeted fluorescent probes. *Nature communications*, **2018**, *9(1)*, 334.

3. **Cao, Y.***, Qiu, T.*, Kathayat, R.S.*, Azizi, S.A., Thorne, A.K., Ahn, D., Fukata, Y., Fukata, M., Rice, P.A. and Dickinson, B.C. ABHD10 is an *S*-depalmitoylase affecting redox homeostasis through peroxiredoxin-5. *Nature chemical biology*, **2019**, *15(12)*, 1232-1240.

4. **Cao, Y.**, Liu, H., Lu, S. S., Jones, K. A., Govind, A. P., Jeyifous, O., Simmons, C. Q., Tabatabaei, N., Green, W. N., Holder, J. L., Jr., Tahmasebi, S., George, A. L., Jr., and Dickinson, B. C. RNA-based translation activators for targeted gene upregulation. *Submitted*, **2023**.

†. The following chapters of this dissertation contain sections and figures adopted from the listed publications with modifications. Chapter 2: publication 1, 2 and 3; Chapter 3 and 4: publication 4.

⋆. Denotes equal contribution

CHAPTER 1

INTRODUCTION

Gene expression is regulated through both translation and post-translational modification (PTM) pathways. In this chapter, I will focus on one type of protein PTM, *S*-palmitoylation, to introduce its regulation, biological implications, and existing chemical biology tools to measure this PTM. Subsequently, I will outline new technologies aimed at gene-expression activation, demonstrating the development, mechanism elucidation, and application scopes. This chapter provides a background for understanding the challenges and opportunities for the development of chemical biology technologies in these two research areas, which are ultimately motivated by understanding the biology systems and the development of novel therapeutics.

1.1 Probing the dynamic *S*-Palmitoylation

1.1.1 S-Palmitoylation is an important post-translational modification

S-palmitoylation, the acylation of cysteine residues by a C_{16} saturated lipid palmitate, is an abundant post-translational modification (PTM) in mammalian systems, which was identified in about 10% of the human proteome[1]. The addition of hydrophobic palmitate alters the biochemical and biophysical properties of modified proteins, affecting their stability, subcellular trafficking, localization, activity, and signaling[2–5], with consequences for the pathogenesis of cancer[6], neurodegenerative diseases[7], and microbial infection[8].

1.1.2 Writer and eraser enzymes regulate reversible S-Palmitoylation

Unlike many lipid PTMs, some *S*-palmitoylation is reversible, dynamically regulated by writer protein acyl transferases (PATs) and eraser acyl protein thioesterases (APTs)

(**Figure 1.1**). In humans, there are 23 Asp-His-His-Cys (DHHC) domain-containing PATs, known to be associated with the Golgi, the endoplasmic reticulum (ER) and plasma membranes[9]. In contrast, there are only 7 identified APTs, localized primarily in lysosomes (PPT1 and 2) and the cytosol (APT1 and 2, ABHD17A, B, and C)[10–13].

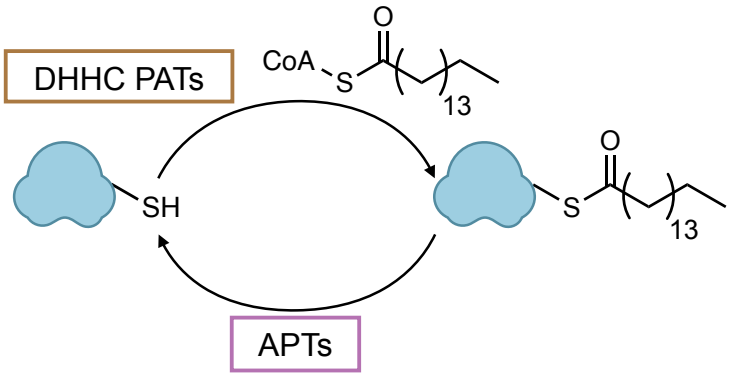

Figure 1.1 Schematic of reversible *S*-palmitoylation on protein.
Schematic showing the chemical structure of palmitoylation modification on cysteine, and dynamic regulation by writer DHHC PATs (protein acyl transferases) and eraser APTs (acyl protein thioesterases). Blue shape indicates a protein substrate susceptible to *S*-palmitoylation.

1.1.3 Chemical biology tools to evaluate S-Palmitoylation

Assessing the palmitoylation status of proteins can be achieved through a variety of chemical biology methods such as acyl-biotin exchange (ABE)[14], acyl-RAC[15], masss hift assays[16], and metabolically labeling with clickable palmitate analogs[17–19]. All these techniques directly measure changes of the palmitoylation level of target proteins and do not report the activities of PATs or APTs. Additionally, these proteomic-based methods have difficulty measuring spatial and dynamic changes of palmitoylation level responding to cell signaling.

To probe the dynamic activity levels of APTs in live cells at real time, our lab developed depalmitoylation probes (DPPs)[20,21] and ratiometric depalmitoylation probes (RDPs)[22]. The DPPs feature a profluorescent molecule tethered to an *S*-acylated pep-

tide substrate through a carbamate linkage. Thioesterase activity on the substrate results in a reaction cascade that leads to carbamate cleavage and release of a brightly fluorescent product (**Figure 1.2**). Importantly, the substrate portion of the DPPs utilizes a natural peptide-based substrate with a modified cysteine residue. We found that DPPs can measure endogenous levels of *S*-depalmitoylases in a range of cell types. Moreover, the DPPs were utilized to uncover rapid growth factor-mediated alterations in the *S*-depalmitoylases, revealing connections between receptor tyrosine kinases and dynamic lipidation signaling[20].

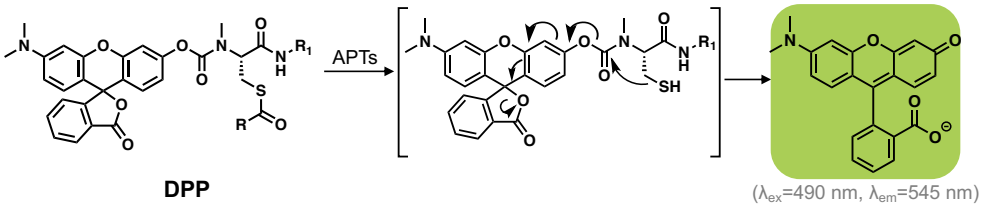

Figure 1.2 Structure and mechanism of depalmitoylation probes (DPPs).
Schematic representing the chemical structure and mechanism of DPPs to detect deacylase (APTs) activity. The thiol acyl modification (R) and the peptide substrate (R1) can be varied.

1.1.4 Current challenges and opportunities

Although the DPPs have provided handy tools for studying dynamic depalmitoylation, the further development of next-generation DPPs will offer diverse probes for studying more precise and specific biological questions. For example, the simplest depalmitoylation probe (DPP-1), with a palmitoylated cysteine, failed in live cell experiments due to poor water solubility. The successful first-generation probes, DPP-2 and DPP-3, use a non-natural surrogate acylation substrate mimetic, *S*-octanoylation (a C_8 lipid), instead[20]. Although this shorter lipid modification increases water solubility and cell permeability, it potentially also detects false-positive signals generated by other thioesterases beyond depalmitoylases, which act on shorter lipid modified cysteines. Thus, the utility and speci-

ficity of the DPPs could be dramatically enhanced if they utilized a natural palmitoyl lipid modification as a substrate.

The proteomic analysis of the *S*-palmitoylated proteome found that *S*-palmitoylated proteins are present across a range of cellular compartments, including the lysosome, nucleus, endoplasmic reticulum and mitochondria[23]. Development of DPPs localized to specific cellular compartments can reveal the localization of depalmitoylation activity, and facilitate the discoveries and characterization of depalmitoylation enzymes restricted to such cellular compartments.

Considering the large population and diverse localizations of palmitoylated proteins and intricate regulation of the lipidation status of the proteome in response to cell signaling, we hypothesized that there may be other, yet unannotated, APTs. For example, the generic inhibition of depalmitoylases by Palmostatin B (Palm B) or HDFP triggers the inactivation of G protein-regulated inwardly rectifying potassium (GIRK) channel, which cannot be reproduced by knockdown of either known APTs[24]. The DPPs can be utilized to monitor depalmitoylation activity of enzymes *in vitro* and *in cellulo*, which can lead to the identification of novel depalmitoylases.

1.2 Nucleic acid-based therapeutic approaches to amplify targeted gene expression

Insufficient expression of critical proteins, triggered by gene deletions, mutations, or downregulation of expression by pathological conditions, drive a large swath of human diseases, including cancer[25], neurodegeneration[26], metabolic disorders[27], and rare genetic disease[28,29]. Despite the great demand, therapeutic technologies to amplify gene expression have been under-developed compared to therapeutics with inhibitory or degradation effects. Recent advances in chemical modifications[30] and delivery methods[31]

of nucleic acid-based therapeutics (NBTs) drove monumental clinical success[32], and opened new possibilities for gene-activation technologies[33]. These gene-activating technologies can be broadly classified by mechanistic functions into NBTs to increase productive mRNA abundance, including mRNA delivery[34], splicing modulators[32,35], transcripts stabilizers[36] and activators[37,38]; and translation activating NBTs[39–42] (**Figure 1.3**). Each technology possesses important strengths for disease treatments, but also has defined limitations due to diverse pathological mechanisms and different characteristics of target transcripts.

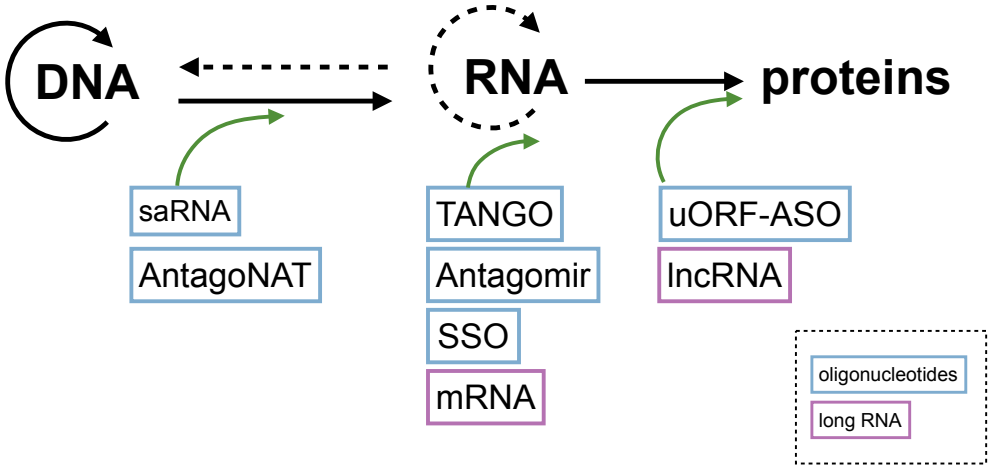

Figure 1.3 Nucleic acid-based therapeutics for gene activation.
Schematic of nucleic acid-based therapeutics (NBTs) mentioned in this chapter. Green arrows indicate the process or targets activated by the NBTs along the central dogma. NBTs in blue square are oligonucleotide-based, and in purple square are long RNAs.

1.2.1 NBTs to increase productive transcript abundance

Therapeutic mRNA delivery

Several technologies have been developed to activate gene expression by increasing productive mRNA levels. The most direct method is to introduce exogenous mRNA into cells, which encodes the desired functional protein[34]. The mRNA delivery ensures the

functional protein to be localized to correct cell compartments and added necessary post-translational modifications, which is advantageous compared to direct protein delivery. The mRNAs with adequate chemical modifications are deliverable by lipid nanoparticles (LNPs), which are overall less immunogenic compared to gene therapies delivered by viral particles[43]. Continuous development of therapeutic mRNAs has resulted in the success of the most impactful mRNA vaccines, COVID-19 vaccines; and several other mRNA therapeutics into clinical trials[44–46]. Limitations of mRNA therapies are the difficulty in high-fidelity manufacturing and low stability during storage. They are also not suitable for protein replacement in some contexts, due to the toxicity of high levels of overexpression of the target gene, similar to the issues with gene therapies.[47,48]; The uncontrolled delivery of exogenous mRNAs in addition to target cells can also be problematic.

Transcription activating RNAs

To achieve a controllable level of gene activation, researchers developed synthetic short double-stranded oligonucleotides to induce target-specific gene expression. Although short double-stranded RNAs (dsRNAs), which are typically 21 nucleotides with two overhanging nucleotides at the 3' end of each strand, are better known to degrade homologous mRNAs[49], some short dsRNAs complementary to promoter or enhancer regions of a target gene are able to induce gene expression, named as small activating RNAs (saRNA) or RNA activation (RNAa)[37,38]. A leading saRNA therapy developed by MiNA Therapeutics, called MTL-CEBPA[50], is currently in Phase II clinical trials. MTL-CEBPA increases the protein level of liver transcription factor, CCAAT/enhancer-binding protein alpha (CEBPA), about 2 fold, to enhance the efficacy of standard-of-care cancer drugs[51], validating the exciting therapeutic potentials of transcription activating NBTs. However, the complete molecular mechanisms of RNA activation is still disputed[52,53], thus it is unknown whether any particular disease-associated gene can be targeted by

saRNAs before a considerable scale screening of the effective saRNAs were carried out. Therefore, the scope and breadth of this technology is unclear.

RNA splicing modulators

Both introducing exogenous mRNAs and saRNA technologies themselves offer no cell-type specificity, resulting in increased proteins in all cells, which in some cases is problematic due to adverse effects and toxicity when the protein is produced in the wrong cell context. To increase the productive transcripts based on mRNAs already present in the target cell, thus providing cell-type specificity, splicing modulators have been developed.

Alternative splicing (AS) is an important cellular process for gene regulation, which generates diverse mature transcripts by joining different combinations of exons from a single gene[54]. Genetic mutations can trigger aberrant splicing to decrease productive mRNAs, which can be corrected by splice-switching antisense oligonucleotides (ASOs)[55]. These synthetic splice-switching ASOs, termed SSOs, either base-pair to splicing enhancer elements for exon-skipping[56], or block splicing silencer elements to achieve exon-inclusion[57]. The well-known SSO, Nusinersen, inhibits the skipping of exon 7 in Survival of Motor Neuron 2 (SMN2) transcripts, thus supplements the desired SMN protein to treat spinal muscular atrophy (SMA)[32]. Nusinersen has been approved by FDA and tremendously improved patients' life quality since 2016.

Another example of splice-switching ASOs is TANGO (targeted augmentation of nuclear gene output) platform. More than one third of alternative splicing isoforms are non-productive, which contain a premature stop codon (PTC), and are degraded via the nonsense-mediated mRNA decay (NMD) pathway[58]. TANGO modulates the splicing to skip the PTC-containing exon, thus transforms naturally occurring non-productive AS isoforms, into full-length productive transcripts, to increase functional protein amount[35]. This

novel technology has been applied to several targets[35,59–61], among which the *SCN1A*-targeting TANGO (STK-001), developed by Stoke Therapeutics, which is currently in phase I/IIa clinical trials for Dravet syndrome, which is one type of childhood epilepsy caused by heterozygous mutations on *SCN1A* (Sodium Voltage-Gated Channel Alpha Subunit 1)[62]. These splice-switching ASOs are ideal for mRNA targets that can be corrected to the functional transcript from an endogenous alternative splicing isoforms, but are not suitable for all other cases.

Antagonist for inhibitory elements on gene expression

Gene expression is downregulated when mRNAs are bound by microRNAs[63] or natural antisense transcripts (NATs)[64]. Single-stranded NAT-specific oligonucleotides, termed AntagoNAT, and Antagomirs[65] target these inhibitory non-coding RNAs to prevent them from binding mRNAs, thus upregulate target gene expression. None of the clinically tested Antagomirs have entered Phase III trials yet because of the toxicity, but there are still some on-going efforts to develop antagomirs for cancer treatment[66]. Researchers are also pushing forward AntagoNAT to upregulate *SCN1A* for clinical trials[67].

1.2.2 NBTs to activate translation on endogenous target mRNAs

Translation activators, which upregulate protein production from cellular mRNAs, do not rely on specific transcriptional regulatory properties, therefore should be suitable for a broad range of mRNAs. However, existing translation activation NBTs have very limited applicable target scope, and are not as well-developed as NBTs that increase mRNA abundance, in all aspects.

ASO-based translation activators

The translation activators based on ASOs function either by blocking upstream open reading frame (uORF) to increase translation efficiency of downstream ORF[40], or by binding to inhibitory RNA elements in 5' UTRs to accelerate translation initiation[39]. For example, a 18-mer uORF-ASO (ASO-761933) targeting the *Lrpprc* uORF increased LRPPRC protein levels in by approximately 82% in mouse with two doses. These platforms have valuable potentials, but cannot be flexibly applied to most targets, unless the targeted transcripts contain a specific translation inhibitory element. The uORF-blocking ASOs not only require the transcript has an upstream ORF, but also require that uORF inhibits downstream ORF translation. However, at most 49% of human mRNAs contain uORF and only about 30 of them have been experimentally validated to regulate translation[68]. Some of the uORFs encode functional protein isoforms, such as uORFs in VEGF-A[69], therefore are not suitable to be blocked by ASOs. Some uORFS have important biological functions, the inhibition of which are dangerous and cause disease[70–72]. As a consequence, these ASOs are not widely recognized or used.

long-noncoding RNA-based translation activators

Another group of translation activators takes advantage of a long noncoding RNA (lncRNA) based on the SINEB2 domain[73], which upregulates translation without affecting mRNA abundance. These technologies, termed SINEUP or RNAe, consist of a binding domain (BD) to bind a target mRNA and effector domain (ED) to increase translation. Synthetic SINEUPs or RNAe have been created by swapping binding domains to target an RNA of interest[42,74–76]. However, these therapeutic RNAs are generally long (250-1200 nt)[42,77], hindering their manufacture, delivery, and stability, therefore limiting them to viral-delivery approaches. Importantly, lncRNA-based translation activators strictly require binding domains overlapping the translation initiation sites on target transcripts[77], thus not

applicable for transcripts with no suitable binding sites near start codon, possibly due to short 5' UTRs or critical off-targets generated by the mismatches from the binding domain.

1.2.3 Current challenges and opportunities

As described above, gene activation by chemical biology approaches has attracted substantial interest in academia and the pharmaceutical industry, because of its tremendous potential for disease treatments[33]. Gene activation is not just suitable for genetic disorders, but also needed to increase beneficial proteins under pathological conditions in other contexts. For example, wild-type *PTEN* expression is known to be downregulated by several RNA regulation pathways, including by overactive microRNAs, to promote cancer[78]. In such case, successful expression increase of PTEN in cancer cells could suppress tumor growth, as demonstrated by direct PTEN mRNA delivery to tumors[79]. Given the extensive gene targets in diverse diseases, there exists a considerable scope for the development of novel gene activation technologies.

New gene activation therapeutics are also needed because of the complexity of some of the most important pathological conditions that currently lack treatments. An example this thesis will focus in on later is *SYNGAP1* haploinsufficiency-related disorders. Heterozygous mutations on this gene are one of the most common causes of intellectual disability with epilepsy[80], but no treatments are available. This is a difficult target for existing gene activation approaches. The *SYNGAP1* gene is too long for AAV-based gene replacement therapy[81], and is not suitable for mRNA delivery, since the overexpression of SYNGAP1 protein is also damaging[82]. Moreover, data indicate that endogenous SYNGAP1 transcript levels vary across different types of neurons and brain regions[83,84], thus requiring cell-type specific upregulation. Recent attempts were taken using splice-switching oligonucleotides (TANGO)[60,61] to correct NMD-containing transcripts to boost mRNA abundance. Although effective *in vitro*, these ASOs generated only marginal in-

crease in SYNGAP1 mRNA level, with unreported effects on protein levels, possibly due to the low abundance of NMD transcripts in neurons[60].

All the aforementioned nucleic-acid based therapeutic technologies have great value, but every approach has its specific set of applicable gene targets because of its technical and/or biological limitations. Development of innovative gene activation technologies can open up new opportunities to correct difficult targets. Moreover, several distinct technologies can also be applied in combination, such as combining transcription activators with translation activators, to generate higher level of target protein production and extra layers of control. Collectively, additional nucleic-acid based gene activation approaches, especially those that modulate different cell regulatory pathways, will open new opportunities for biological study and disease treatments.

1.3 Scope of this thesis

In this thesis, I will focus on chemical biology technology development in two areas, to probe the *S*-depalmitoylase activity for biological discoveries; and to activate translation of target mRNA-of-interest in mammalian systems as potential therapeutics.

Chapter 2 presents the development of new fluorescent probes for *S*-depalmitoylase activities, followed by discovery and characterization of a new *S*-depalmitoylase member.

Chapter 3 describes the development of "translation activating RNA" (taRNA), a platform of RNA molecules that activate the translation of a wide range of mRNAs of interest in mammalian cells.

Chapter 4 explores the viral and non-viral delivery options for taRNA, showcases the engineering of a compact version with improved activity, and validated its function in gene-haploinsufficient cells from patient.

Chapter 5 summarizes this dissertation and provides a broader perspective and outlook based on the discoveries in this dissertation.

CHAPTER 2

DEPALMITOYLATION PROBES FACILITATE DISCOVERY OF A NOVEL MITOCHONDRIAL *S*-DEPALMITOYLASE

2.1 Introduction

As described in **Chapter 1.1.4**, our lab developed depalmitoylation probes (DPPs), a new family of fluorescent probes that permits the analysis of *S*-depalmitoylases in real time and in live cells[21]. Previous DPPs adopted a non-natural acylation substrate mimetic[20], which potentially probes other thioesterases besides the desired depalmitoylases. Therefore, development of new DPPs, which utilize the natural palmitoyl lipid modification, will improve the specificity of the DPPs.

Unbiased mass spectrometry-based protein profiling approaches have revealed that many resident mitochondrial proteins are *S*-palmitoylated[23], including those involved in fatty acid transport and metabolism, electron transport chain, ATP synthesis, and antioxidant defense and redox signaling[85,86]. The presence of *S*-palmitoylated mitochondrial proteins is particularly interesting because the enzymatic machinery for the installation and removal of protein lipidation in the mitochondria is, to-date, mostly unclear. Barring reports implicating DHHC8 and 13 in mitochondrial function[87,88], there were no demonstrations of enzyme-mediated *S*-depalmitoylation in this organelle.

This chapter presents DPP-4 and DPP-5, two new fluorescent probes for monitoring *S*-depalmitoylase activities with improved water solubility and cell permeability; and mitochondrial-targeted *S*-depalmitoylation probes (mitoDPPs), a toolkit of small molecule-based fluorescent probes that are selectively targeted to the mitochondria and measure *S*-deacylase activity within this compartment. Using mitoDPPs, we discovered *S*-depalmitoylation activity in mitochondria and discovered that APT1, which was previously annotated primarily as a cytosolic protein[10], is also localized to mitochondria. Through

a fluorescence imaging-based screening in cells, we identified ABHD10, a putative mitochondrial resident protein related to APT1 that belongs to the metabolic serine hydrolase (mSH) superfamily[12], as a novel mitochondrial depalmitoylase. We characterized ABHD10 through *in vitro* biochemical and cell-based assays, as well as high-resolution structural studies, which revealed that ABHD10 has peptide *S*-depalmitoylase activity. Finally, we discovered that the antioxidant activity of PRDX5[89], a key player in the mitochondrial antioxidant machinery, is regulated by ABHD10 via *S*-depalmitoylation of its active site, providing a connection between lipidation-regulated ABHD10 activity and mitochondrial redox homeostasis.

2.2 Results

2.2.1 A S-depalmitoylase probe with improved water solubility

To allow a palmitoyl modification on DPPs, we increased the solubility of the probe scaffold and generated two new molecules, DPP-4, which has an acetyl-amide modification on the piperazine; and DPP-5, which has a succinylated amide and therefore features a carboxylic acid (**Figure 2.1**).

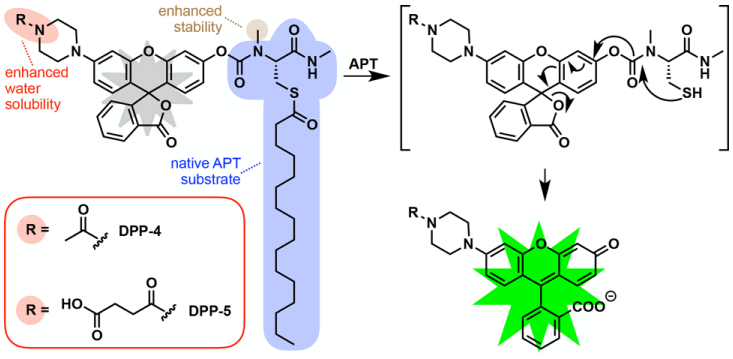

Figure 2.1 Schematic illustration of DPP-4 and DPP-5.
An *S*-palmitoylated peptide substrate is used in both DPPs. Thioesterase (APT) activity will generate fluorescence. Additional functional groups (R) enhanced water solubility.

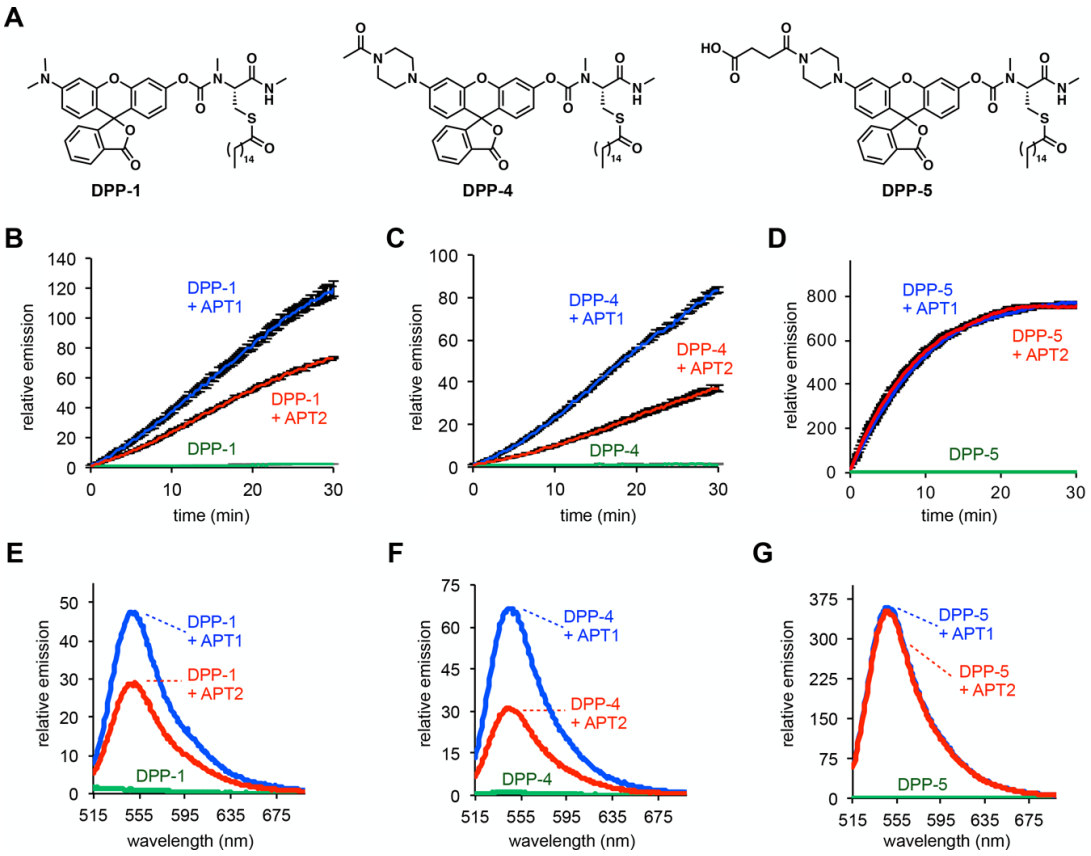

Figure 2.2 *In vitro* characterization of DPP-4 and DPP-5.
(A) Structures of DPP-1 (first-generation probe) and the two new probes, DPP-4 and DPP-5. *In vitro* assays of 1 μM **(B)** DPP-1, **(C)** DPP-4, and **(D)** DPP-5 in HEPES (20 mM, pH 7.4, 150 mM NaCl) with or without 50 nM purified APT1 or 50 nM APT2 (λ_{ex} 490/20 nm; λ_{em} 545/20 nm). Error bars are ±SEM (n = 4). Fluorescence emission spectra of **(E)** DPP-1, **(F)** DPP-4, and **(G)** DPP-5 in HEPES (20 mM, pH 7.4, 150 mM NaCl) after treatment for 30 min with or without 50 nM APT1 or 50 nM APT2 (λ_{ex} 485 nm). All data normalized to the background of the probe alone.

We compared the new probes with DPP-1 in *in vitro* assays with recombinantly expressed human APT1 and APT2 (**Figure 2.2A**). Both DPP-1 (**Figure 2.2B**) and DPP-4 (**Figure 2.2C**) display very slow kinetics with APT1 and APT2 in the absence of detergents. After incubation for 30 min with 1 μM probe and 50 nM APT1 or APT2, DPP-1 and DPP-4 showed only 50- or 30-fold and 70- or 30-fold enhancement in the intensities of their fluorescence signals, respectively (**Figure 2.2E and F**). DPP-5, however, showed a rapid turn-on response to both APT1 and APT2 (**Figure 2.2D**), with a 350-fold increase

in the intensity of the fluorescent signal with both enzymes (**Figure 2.2G**), likely due to enhanced water solubility afforded by the additional carboxylate. Indeed, LogP analysis of DPP-1, -4, and -5 corroborates the higher water solubility of DPP-5 compared to those of DPP-1 and DPP-4 (**Figure 2.3A**). Kinetic analysis revealed DPP-5 has kinetic parameters comparable to those of previously reported N-Ras-based semisynthetic substrates for APT1 and APT2 (**Figure 2.3B-D**).

A

	LogP
DPP-1	1.57
DPP-4	1.74
DPP-5	0.79

B

	K_M (μM)	k_{cat} (s^{-1})	k_{cat}/K_M (s^{-1} M^{-1})
APT1	1.6	0.044	2.8×10^4
APT2	2.1	0.066	3.1×10^4

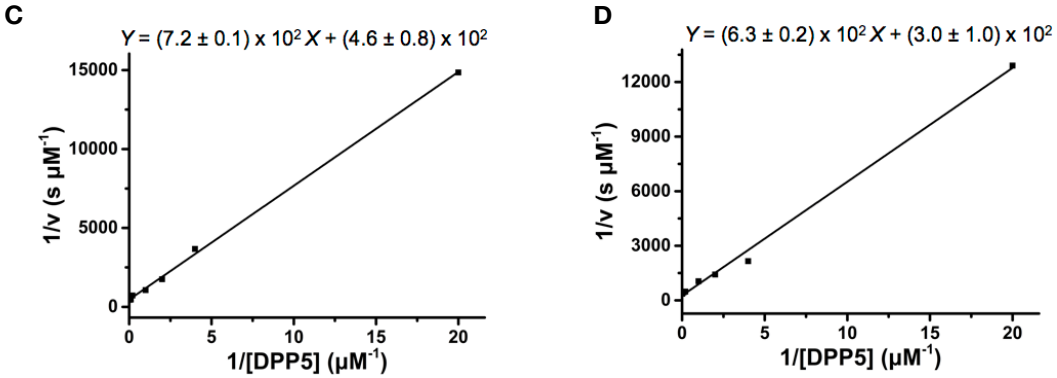

Figure 2.3 *In vitro* characterization of DPP-4 and DPP-5.
(A) Kinetic parameters of APT1 and APT2 with DPP-5. **(B)** LogP values presenting the water solubility of DPP-1, DPP-4 and DPP-5. Lineweaver–Burk plot of DPP-5 with **(C)** 50 nM APT1 **(D)** 50 nM APT2 to generate kinetic parameters in (B).

Finally, we performed imaging experiments in HEK293T cells to compare the signal obtained with DPP-5 to DPP-1 and DPP-4 in live cells. Using the same concentrations of each probe and the same microscope settings, DPP-5 treatment resulted in a robust fluorescent signal, while DPP-1 and DPP-4 displayed very low, almost undetectable levels of fluorescence (**Figure 2.4**). Collectively, these results indicate that the additional carboxylate functional group generates a robust DPP probe carrying the natural palmitoy-

lated substrate, DPP-5, with great water solubility and dramatically improved performance in live cells.

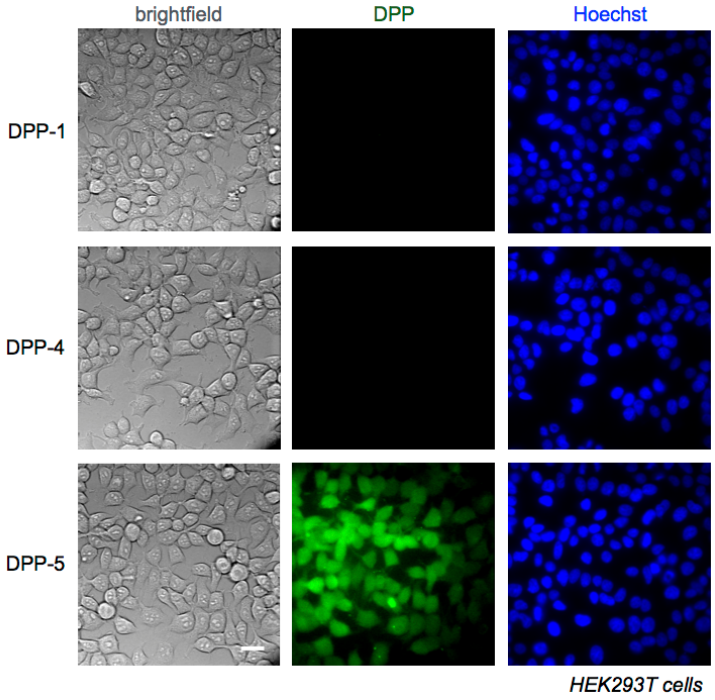

Figure 2.4 Comparison of DPP-1, DPP-4 and DPP-5 *in cellulo*.
HEK293T cells treated for 30 min with 1 µM Hoechst 33342, washed, loaded with 1 µM of either DPP-1, DPP-4 or DPP-5 for 20 min, and then analyzed by epifluorscence microscopy. Images for brightfield, DPP-1/DPP-4/DPP-5, Hoechst 33342 nuclear stain, and an overlay of DPP-1/DPP-4/DPP-5 and Hoechst 33342 are shown for each set of conditions. 20 µm scale bar shown.

2.2.2 Targeted DPPs reveal mitochondrial S-depalmitoylation activity

To experimentally test whether there is active *S*-depalmitoylation in the mitochondria of mammalian cells, we generated mitochondrial-targeted *S*-deacylase probes, mitoDPP-2 and mitoDPP-3 (**Figure 2.5**). A mitochondrial delivery group, lipophilic cation triphenylphosphonium (TPP), was added to the probe scaffold of original DPP-2 and DPP-3, which can shuttle cargo to the mitochondria based on the electrochemical gradient[90] and has been successfully deployed to deliver probes to mitochondria[91].

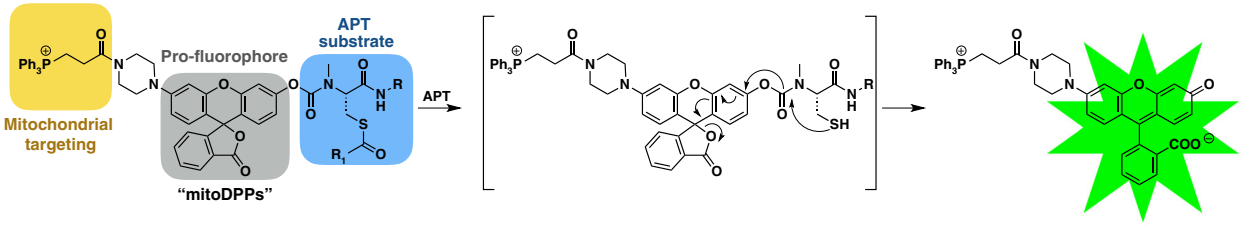

Figure 2.5 Design and activation of mitoDPPs.
MitoDPPs localize to the mitochondria via an appended triphenylphosphonium group. Cleavage of the thioester by reaction with an APT rapidly generates a fluorescent product.

We tested whether mitoDPP-2 (**Figure 2.6A**) and mitoDPP-3 (**Figure 2.6B**) respond to recombinant human APTs *in vitro*. Both mitoDPP-2 and mitoDPP-3 display very low fluorescence in buffer, but have a dramatic increase in fluorescence upon incubation with purified human APT1 or APT2 enzymes (**Figure 2.6C-F**).

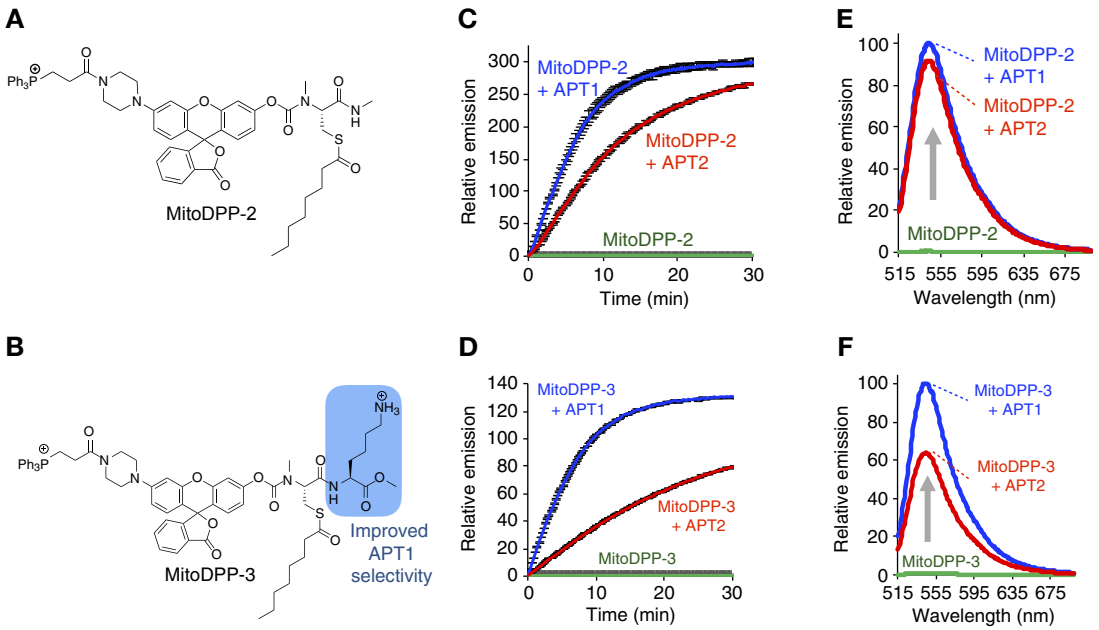

Figure 2.6 *In vitro* activity of mitoDPP-2 and mitoDPP-3.
(A-B) Chemical structure of MitoDPP-2 (A) and MitoDPP-3 (B). **(C-D)** *In vitro* fluorescence assay of mitoDPP-2 (C) or mitoDPP-3 (D) at 1 μM in HEPES (20 mM, pH 7.4, 150 mM NaCl, 0.1% Triton X-100) with either 50 nM purified APT1 or APT2 (λ_{ex} 490/20 nm; λ_{em} 545/20 nm). Error bars are ± SEM (n = 3). **(E-F)** Fluorescence emission spectra at 30 min from probes as treated in (C) or in (D).

Through careful characterization by my collaborators, we validated both mitoDPP-2 and mitoDPP-3 are predominantly localized to mitochondria, and has robust response to mitochondrial depalmitoylation activity in live cells[92]. Surprisingly, we found APT1, which has been considered solely as a cytosolic protein, is an active mitochondrial *S*-deacylase. Using mitoDPP-3, which has improved APT1 selectivity (**Figure 2.6B and D**), we show inhibition of APT1 activity by genetic perturbation (**Figure 2.7A**) or selective inhibitor (ML348) (**Figure 2.7B**) decreased mitoDPP-3 signal in live cells by 20% or 40% respectively, proving APT1 is active in mitochondria. Furthermore, the pan-inhibitor for all *S*-depalmitoylases, Palmostatin B (PalmB)[2], decreased mitoDPP-3 signal by more than 80% (**Figure 2.7C**). Considering mitoDPP-3 only measures the depalmitoylation activity in mitochondria, this indicates some other proteins(s) besides APT1 also has depalmitoylation activity in mitochondria (**Figure 2.7D**).

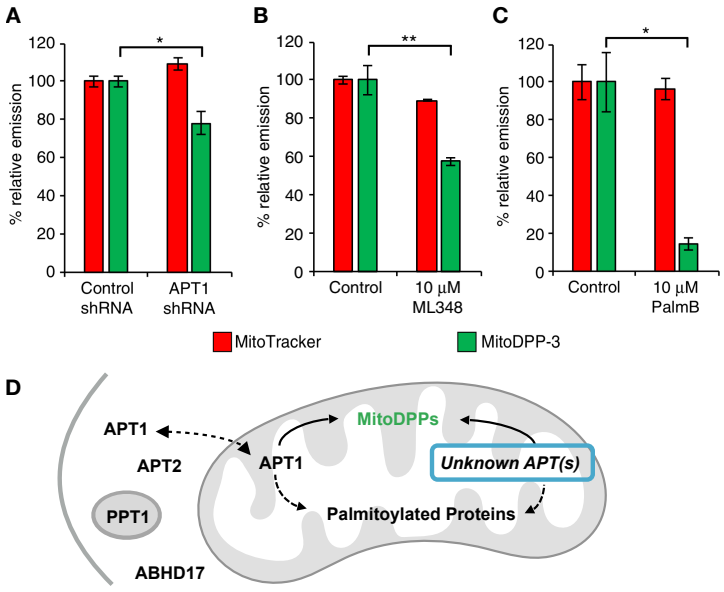

Figure 2.7 MitoDPP-3 imaging in live cells reveals mitochondrial depalmitoylases. Quantification of the relative fluorescence intensity from mitoDPP-3 (green) and MitoTracker (red) in HEK293T cells treated with either control or APT1 shRNA **(A)**; APT1 inhibitor, ML348 **(B)**; pan-inhibitor, PalmB **(C)**. n = 4 for (A) and (B). n = 3 for (C). Error bars are ± SEM. Statistics by Student's t-test. $*P < 0.05$, $**P < 0.01$. **(D)** Schematic presenting unknown depalmitoylase(s), besides APT1, is accountable for the depalmitoylation activity detected by mitoDPPs. APT2, PPT1 and ABHD17 are known depalmitoylases.

2.2.3 ABHD10 is identified as a new depalmitoylase in mitochondria

To identify the potential mitochondrial *S*-depalmitoylase, we used the probe DPP-2[20] and performed a fluorescence imaging-based screening in HEK293T cells overexpressing a library of α/β-hydrolase domain-containing protein (ABHD) family members[13] related to APT1 and APT2 (**Figure 2.8A**). As expected, we observed an increase in the DPP-2 fluorescence signal in cells overexpressing known *S*-depalmitoylases, such as APT1, APT2 and PPT1 (**Figure 2.8B**). Strikingly, overexpression of ABHD10 resulted in an enhancement of DPP-2 fluorescence similar to that of APT1, suggesting that ABHD10 has peptide *S*-deacylase activity (**Figure 2.8B**). ABHD10 is a putative mitochondrial protein[93] annotated as a lipase for acyl glucuronide (AcMPAG) deglucuronidation[94,95], but has no identified endogenous substrates yet. Thus, given that ABHD10 possessed peptide *S*-deacylase activity in live cells and is purportedly mitochondrial, it became the candidate for further investigation.

To test the deacylation activity of ABHD10 in the mitochondria in live cells, we expressed ABHD10 in HEK293T cells and measured mitochondrial APT activity using probe mitoDPP-2, the mitochondria-targeted APT activity probe. Overexpression of wild-type human ABHD10 results in increased mitoDPP-2 signal, signifying higher *S*-deacylase activity, as compared with both overexpression of the empty vector (**Figure 2.8C and D**) or the catalytically inactive ABHD10 (S152A) mutant (**Figure 2.8E and F**), confirming ABHD10 is an active deacylase in mitochondria.

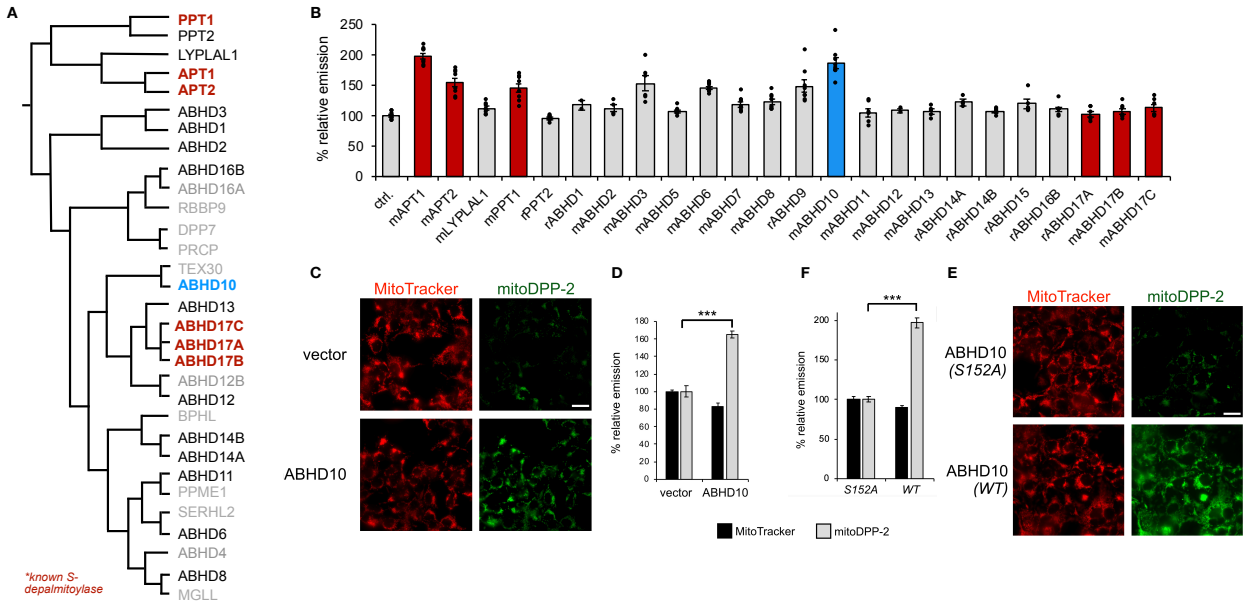

Figure 2.8 ABHD10 has mitochondrial *S*-deacylase activity in live cells.
(A) Dendrogram adapted from the literature14 depicting known *S*-depalmitoylases (red) and members of the mSH family screened for potential peptide *S*-deacylase activity in HEK293T cells. Additionally, ABHD5, ABHD7, ABHD9 and ABHD15 were included in the screen. **(B)** Epifluorescence-based screening with *S*-deacylase probe DPP-2 in HEK293T cells overexpressing a library of proteins related to the known APTs. Letters 'm' and 'r' indicate mouse and rat, respectively. Data were normalized to control cells treated with empty vector. Each column contains more than 2 images from two biological replicates. **(C)** Representative images confirming mitochondrial *S*-deacylation activity of ABHD10 (WT vs. empty vector) in HEK293T cells as measured using mitoDPP-2, a mitochondrial APT probe. Scale bar, 25 µm. **(D)** Quantification of relative fluorescence intensities from mitochondrial marker MitoTracker (black) and mitoDPP-2 (gray) in each set of conditions shown in (C). (n = 8 images from two biological replicates). **(E)** Representative images of *S*-deacylation activity of ABHD10 (WT vs. S152A mutation) in HEK293T cells as measured using mitoDPP-2. **(F)** Quantification of (C). (n = 8). Data expressed as mean ± SEM. Statistical analyses performed with two-tailed Student's t-test with unequal variance.

2.2.4 Biochemical characterization of ABHD10

Given that ABHD10 expression resulted in enhanced APT activity in live cells, we continued to characterize its *S*-depalmitoylase activity *in vitro*. We purified the mature form of human ABHD10[95] (**Figure 2.9A**) and its active site- mutated variant (S152A) for

in vitro *S*-depalmitoylation assay with DPP-5. As mentioned in **Chapter 2.2.1**, DPP-5 uses a native cysteine *S*-palmitoyl substrate, and therefore directly reports on peptide *S*-depalmitoylase activity instead of deacylase activity. Enzymatic assays with DPP-5 revealed that ABHD10 indeed possesses *S*-depalmitoylation activity (**Figure 2.9B**). Kinetic analysis also showed that ABHD10 has a slower turnover rate compared with APT1, but a lower K_M (**Figure 2.9C and D**), indicating ABHD10 has improved substrate affinity.

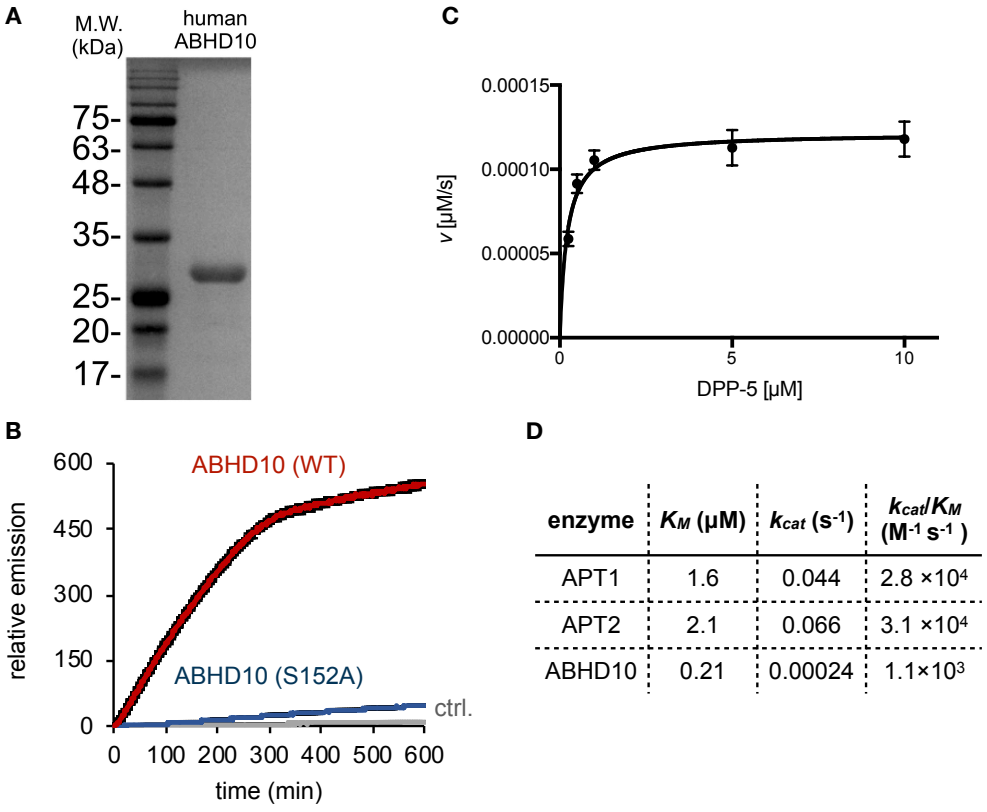

enzyme	K_M (µM)	k_{cat} (s^{-1})	k_{cat}/K_M (M^{-1} s^{-1})
APT1	1.6	0.044	2.8×10^4
APT2	2.1	0.066	3.1×10^4
ABHD10	0.21	0.00024	1.1×10^3

Figure 2.9 Characterization of ABHD10 *S*-depalmitoylase activity *in vitro*.
(A) SDS-PAGE analysis of purified mature human ABHD10 protein. **(B)** *In vitro* kinetic assay showing *S*-depalmitoylation activity of recombinant mature ABHD10 (500 nM, red) and S152A variant (500 nM, blue) compared to control without added enzyme (gray) as measured using the peptide *S*-depalmitoylase probe DPP-5 (5 µM). Data were normalized to relative emission of control (gray) at t = 0. n = 4 biological replicates. **(C)** Michaelis-Menten kinetics regression of ABHD10 (500 nM) enzymatic kinetics at 37 ℃ with DPP-5 as its substrate. **(D)** Kinetic parameters of ABHD10 calculated based on (C), with comparison to APT1, APT2. Data expressed as mean ± SEM. Statistical analyses performed with two-tailed Student's t-test with unequal variance.

My collaborators developed a mitochondria-targeted inhibitor for depalmitoylases, mitoFP (**Figure 2.10A**). We confirmed *in vitro* that mitoFP inhibits APT1 using DPP-5 and observed a dose-dependent inhibition of APT1 (**Figure 2.10B**), as expected. The *S*-depalmitoylation activity of ABHD10 was subject to inhibition by both mitoFP and PalmB (**Figure 2.10C**). Compared to APT1, ABHD10 is more sensitive to mitoFP inhibition *in vitro* (**Figure 2.10D and E**).

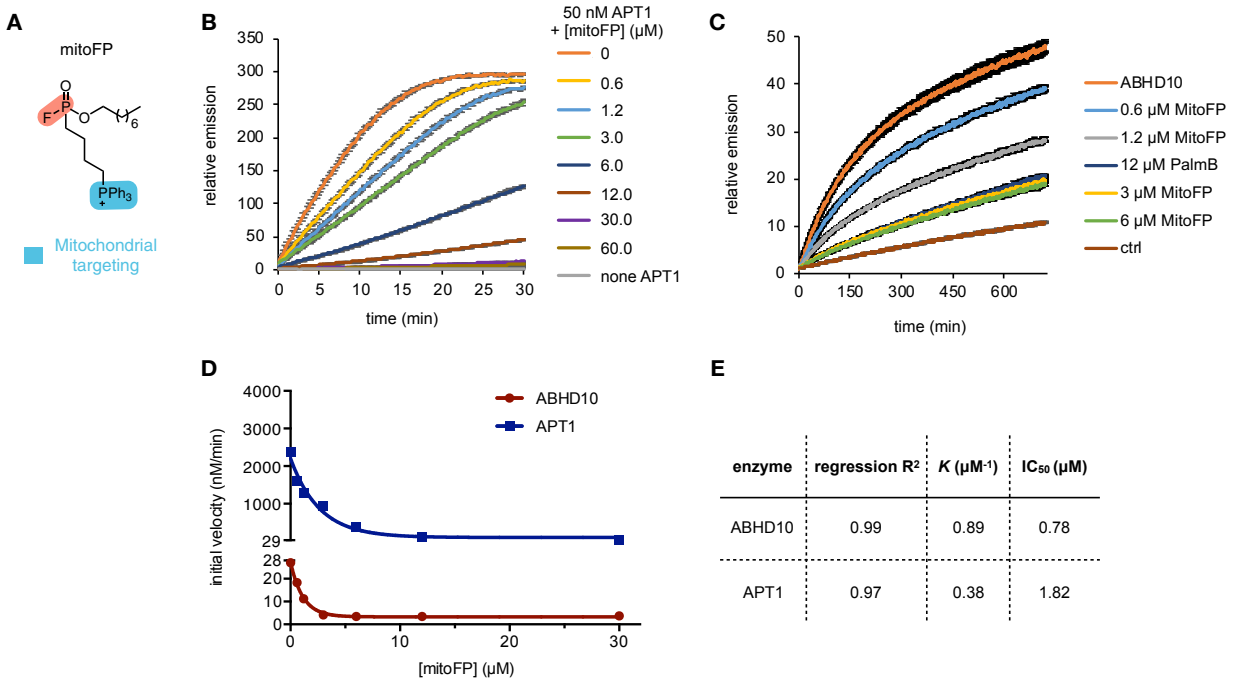

enzyme	regression R^2	K (μM^{-1})	IC_{50} (μM)
ABHD10	0.99	0.89	0.78
APT1	0.97	0.38	1.82

Figure 2.10 Characterization of ABHD10 *S*-depalmitoylase activity *in vitro*.
(A) SDS-PAGE analysis of purified mature human ABHD10 protein. **(B-C)** *In vitro* fluorescence-based kinetic assay showing mitoFP-dose-dependent inhibition of (B) recombinant APT1 (50 nM), and (C) mature human ABHD10 (50 nM) activities measured using DPP-5 (1 μM). Data expressed as mean ± SEM (n = 4) and normalized to relative emission of control at t = 0. **(D)** One phase exponential decay regression of initial enzyme reaction velocity in (B)) and (C) vs varying concentrations of mitoFP. **(E)** Parameters calculated from regression shown in (D).

2.2.5 Structural characterization of ABHD10

During kinetic characterization of ABHD10, we observed a higher substrate affinity (K_M) but much slower catalytic conversion rate (k_{cat}) of ABHD10 with DPP-5, compared to APT1 *in vitro* (**Figure 2.9D**). ABHD10 is also more sensitive to mitoFP inhibition (**Figure 2.10E**). These interesting differences suggest ABHD10 used a different structure to carry out its depalmitoylation function. To gain insights into the molecular basis of ABHD10 *S*-depalmitoylase activity, we therefore sought to structurally characterize this mitochondrial APT.

We purified the mature form of both human and mouse ABHD10 protein (**Figure 2.11A**) to a quality suitable for crystallization. However, only mouse ABHD10 protein yielded suitable crystals in our screens (**Figure 2.11B**), which was validated to exhibit *S*-depalmitoylation activity *in vitro* by DPP-5 (**Figure 2.11C**). These crystals produced X-ray diffraction patterns at a resolution of 1.66Å, and initial phases were determined by molecular replacement, using a predicted structure as a search model. The structure was refined to R_{work} and R_{free} of 0.195 and 0.218, respectively (Table 2.1), and revealed the unknown mouse ABHD10 structure at high resolution (**Figure 2.11D**). As expected, mature ABHD10 possesses a canonical α/β hydrolase domain with a catalytic triad formed by S100–H227–D197 (**Figure 2.11E**). Notably, the catalytic serine points directly toward the junction of two pockets, one of which is covered by a 'cap' domain and is presumably for lipid chain insertion (binding pocket) on the basis of the hydrophobicity of its interior surface and the incorporation of a methyl pentanediol (MPD) from the crystallization buffer (**Figure 2.11F and G**). Nearby, there is another pocket open to the solvent, potentially for substrate binding (**Figure 2.11H**). Additionally, alignment of the structures for ABHD10 and APT1 shows that APT1 has a flexible loop instead of the lipase 'cap' domain in ABHD10(**Figure 2.11I**)[96,97]. The size and flexibility difference of 'cap' versus loop is likely to affect the accessibility of the catalytic serine, therefore explains the

slower turnover rate that we observed. Overall, these structural elements characterized that ABHD10 is suited for *S*-depalmitoylase activity.

Table 2.1 Data collection and refinement statistics of crystallization.

	mouse ABHD10 (6NY9)
Data collection	
Space group	P 63 2 2
Cell dimensions	
a, b, c (Å)	99.388, 99.388, 149.597
α, β, γ (°)	90, 90, 120
Resolution (Å)	56.46 - 1.657 (1.717 - 1.657) [1]
R_{sym} or R_{merge}	0.1082 (2.72)
I / σI	20.82 (1.60)
Completeness (%)	92.82 (76.98)
Redundancy	12.9 (12.8)
Refinement	
Resolution (Å)	56.46 - 1.657
No. reflections	1879
R_{work} / R_{free}	0.1957 / 0.2187
No. atoms	
Protein	1954
Ligand/ion	12
Water	206
B-factors	
Protein	23.92
Ligand/ion	51.33
Water	34.38
R.m.s. deviations	
Bond lengths (Å)	0.011
Bond angles (°)	1.32

[1] Values in parentheses are for highest-resolution shell.

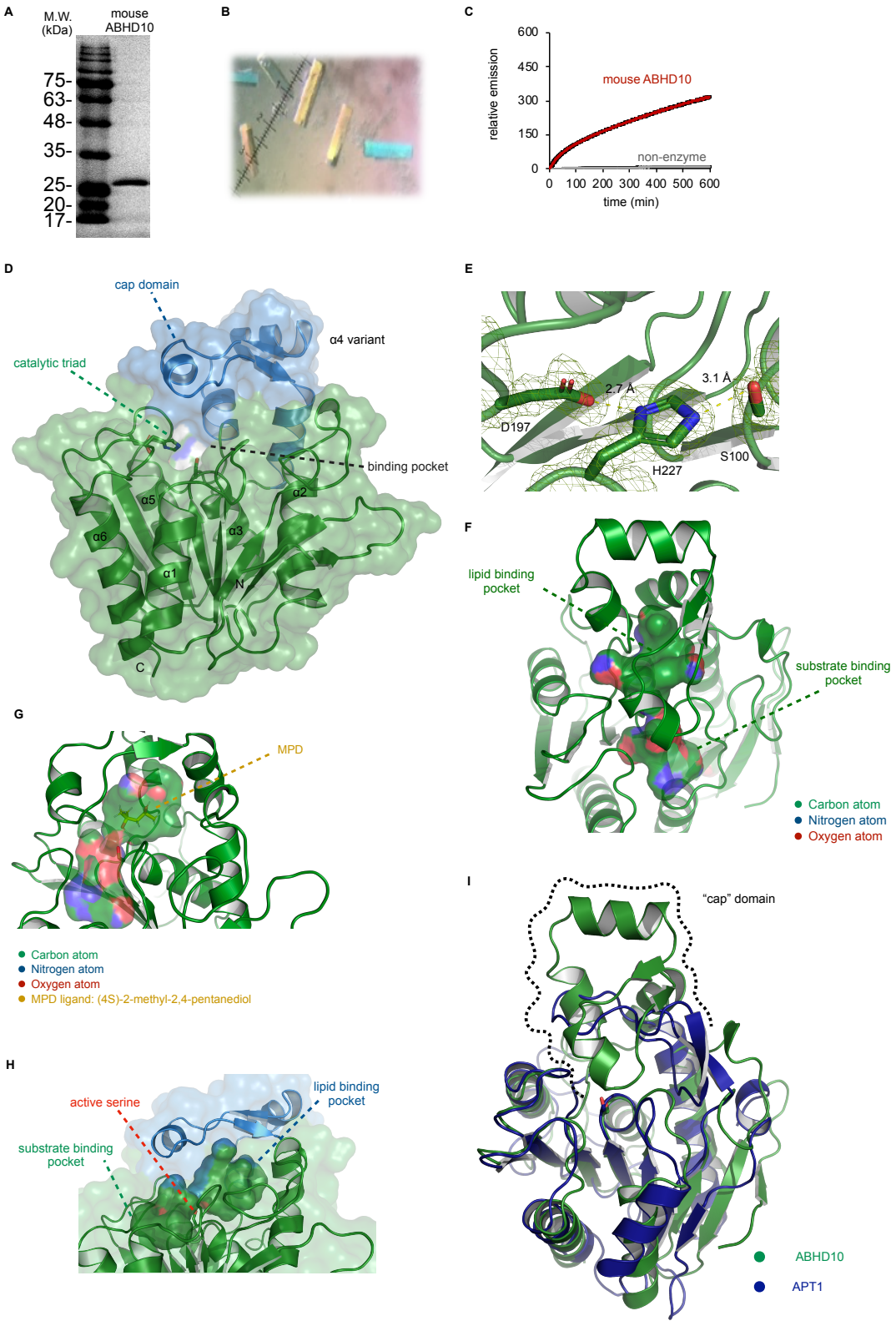

Figure 2.11 Structural characterization of ABHD10 and comparison with APT1.

Figure 2.11 (continued) Structural characterization of ABHD10 and comparison with APT1.
(A) SDS-PAGE analysis of purified mouse ABHD10 protein. **(B)** Crystals of mouse ABHD10 protein for X-ray diffraction. **(C)** fluorescence-based kinetic assay showing *S*-depalmitoylation activity of mouse ABHD10 (500 nM, red) compared to control without enzyme (grey), measured using DPP-5 (5 μM). Data expressed as mean ± SEM (n = 4) and normalized to relative emission of control at t = 0. **(D)** X-ray diffraction structure of mature ABHD10 from *Mus musculus* (PDB: 6NY9). The 'cap' domain (blue) sits above the catalytic triad (shown as sticks) and forms pockets. **(E)** Enlarged view of the Asp–His–Ser catalytic triad shown with weighted $2F_O$ - F_C electron density map (carve = 1.5). Length of hydrogen bonds between Asp and His (2.7 Å) and His and Ser (3.1 Å) is shown. **(F)** Binding pockets of mouse ABHD10, shown with green as carbon atoms, blue as nitrogen atoms and red as oxygen atoms. The putative lipid binding pocket has more surrounding hydrophobic residues than the putative substrate binding pocket. **(G)** Zoomed-in view showing the bound MPD ligand (yellow) in putative lipid binding pocket from the crystallization liquor. **(H)** The surface of two major cavities within the mouse ABHD10 crystal structure is shown, along with the hydroxyl group of the active serine (shown in sticks), which points towards the junction of the two cavities. **(I)** Structure alignment of mouse ABHD10 (green) and human APT1 (blue, PDB: 1FJ2). The dotted black line indicates the cap domain of ABHD10, which is replaced with a loop in APT1. Both active site serines of ABHD10 and APT1 are shown in sticks.

2.2.6 ABHD10 regulates PRDX5 palmitoylation at its active site cysteine

Having characterized the activity and structure of ABHD10, we proceeded to determine its biological role as a mitochondrial *S*-depalmitoylase by identifying its natural substrates. In HEK293T cells, we found peroxiredoxin-5 (PRDX5) showed increased output signal in acyl–biotin exchange (ABE) assay[14] when ABHD10 was knocked down, and showed decreased signal when ABHD10 was overexpressed, demonstrating that ABHD10 regulates PRDX5 lipidation levels (**Figure 2.12A and B**). At the same time, knockdown of ABHD10 had no significant effect on the lipidation levels of PRDX3 or ALDH6A1, other lipidated mitochondrial proteins (**Figure 2.12A**), indicating ABHD10 has selectivity towards this substrate, potentially related to its large 'cap' domain which offers more surface area for substrate recognition. We also found APT1 knockdown has

no effect on PRDX5 or PRDX3 lipidation levels (**Figure 2.12C**), proving the PRDX5 is selectively regulated by ABHD10.

The mature form of PRDX5 contains three cysteine residues at amino acid positions 100, 125 and 204 (**Figure 2.12D**). Among these, Cys 100 and Cys 204 participate in the catalytic cycle of PRDX5 in mitochondria[89]. Identifying which cysteines are the palmitoylated sites will reveal the effects and mechanism of ABHD10 regulation. We expressed wild-type PRDX5-Flag and all three cysteine-to-serine single point mutants in HEK293T cells and analyzed their *S*-acylation levels by ABE (**Figure 2.12E**). We observed a complete abrogation of signal for PRDX5 (C100S), while the C125S and C204S PRDX5 all showed persistent *S*-acylation levels comparable to WT PRDX5, indicating that Cys 100 is the primary *S*-acylation site of PRDX5. We confirmed that this observed *S*-acylation is indeed in the form of palmitoylation using metabolic labeling with clickable palmitate analogue, 17-octadecynoic acid (17-ODYA)[98], again found complete abrogation of signal enrichment for PRDX5^{C100S} (**Figure 2.12F**).

2.2.7 ABHD10 modulates mitochondria redox homeostasis and cell viability under stress

Given that PRDX5 is a key mitochondrial antioxidant protein as the first-responder to H_2O_2[99], we reasoned the ABHD10 is important to regulate mitochondria redox homeostasis. To measure mitochondrial antioxidant buffering capacity, we used mitoPY1, a turn-on fluorescent probe, whose signal reflects H_2O_2 levels in mitochondria[91]. When HEK293T cells were exposed to H_2O_2 as oxidative stress, knockdown of ABHD10 resulted in a striking increase in mitochondrial H_2O_2 levels compared to control (**Figure 2.13A and B**), demonstrating that ABHD10 plays an important role in modulating mitochondrial redox homeostasis in response to oxidative stress. We also substantiated the preservation of mitochondrial integrity upon ABHD10 knockdown by evaluating mem-

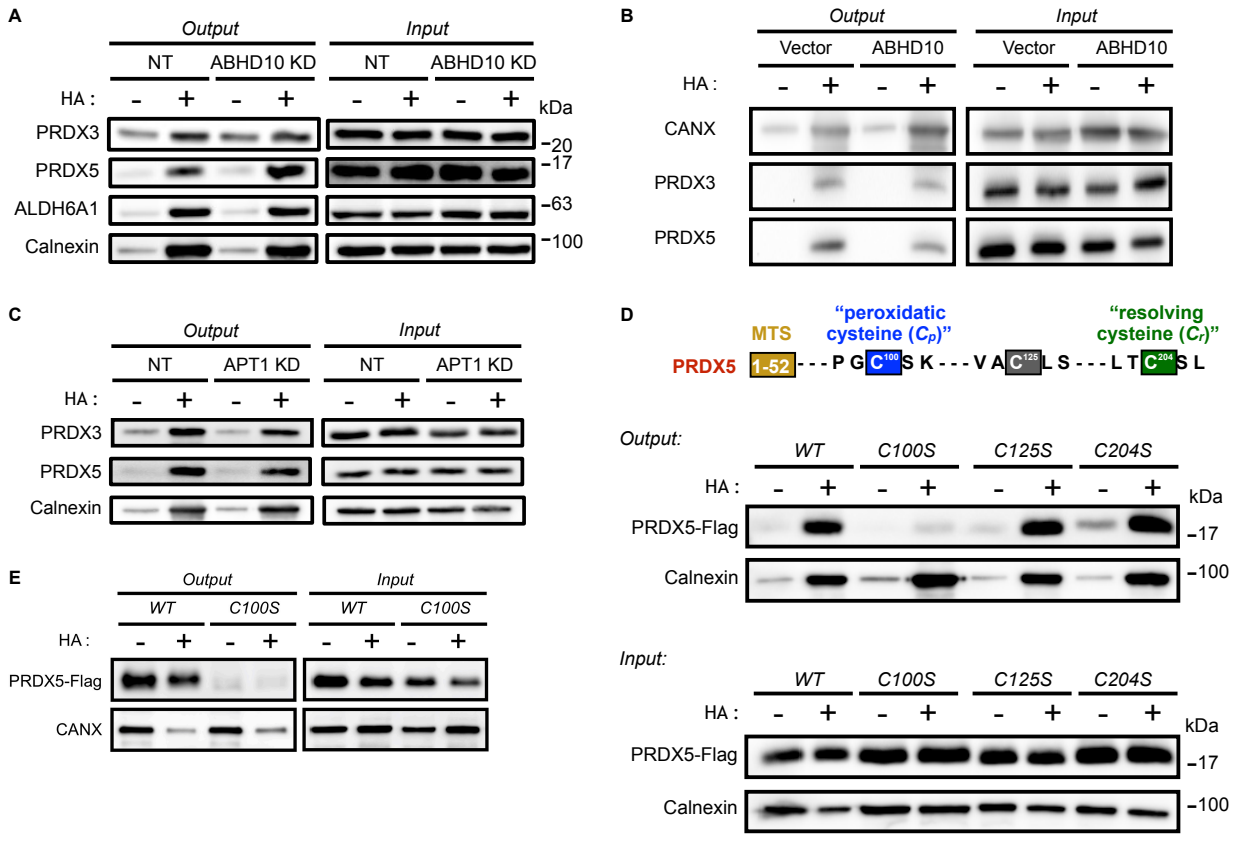

Figure 2.12 ABHD10 regulates *S*-palmitoylation of PRDX5 active site.
(A) ABE assay in HEK293T cells for PRDX5, PRDX3 and ALDH6A1 *S*-palmitoylation level upon ABHD10 knockdown. **(B)** ABE assay in HEK293T cells with ABHD10 overexpression compared to empty pcDNA3 vector transfected cells. **(C)** ABE assay in HEK293T cells measuring *S*-palmitoylation level of PRDX3 and PRDX5 unpon APT1 knockdown. HEK293T cells were transfected with NT siRNA or APT1 siRNA, grown for 44h before the experiments. n = 3 biological replicates. **(D)** Protein map showing the three cysteine residues in mature PRDX5 (upper panel). Lower panel shows ABE assay in HEK293T cells expressing various PRDX5-Flag constructs (WT and three Cys to Ser mutants). n = 2 biological replicates. **(E)** Metabolic labeling with 17-ODYA in HEK293T cells expressing PRDX5-Flag (WT or C100S mutant). Two biological replicates with were performed and produced similar results. Calnexin (CANX) is shown as a persistent *S*-palmitoylated protein control across this panel.

brane potential, which precludes the possibility that ABHD10 knockdown itself damaged mitochondria (**Figure 2.13C and D**).

Inspired by importance of ABHD10 in redox regluation, we further tested whether perturbation of ABHD10 affects cell viability under various oxidative stress conditions. ABHD10 knockdown resulted in a more severe reduction of cell viability in HEK293T triggered with H_2O_2 (E), or paraquat, a potent mitochondrial ROS inducer (F), compared to control cells. Together, these data show that reduced ABHD10 level enhances PRDX5 lipidation at active cysteine, thus rendering cells more vulnerable to oxidative stress, established the model of ABHD10 regulates mitochondrial redox homeostasis via tuning PRDX5 palmitoylation (**Figure 2.14**).

2.3 Conclusion and Discussion

In summary, this chapter presents new generations of *S*-depalmitoylation probes, DPP-5 and mitoDPPs. DPP-5 improves upon the previously developed DPPs to utilize a natural lipid substrate, rather than a surrogate synthetic substrate. DPP-5 is capable of measuring *S*-depalmitoylase activity robustly *in vitro* and in live cells because of the enhanced solubility. MitoDPPs dominantly target to mitochondria and measure the *S*-palmitoylation activity in live cells, which were utilized to prove the *S*-palmitoylase APT1 is localized and active within mitochondria. Using both probes, we also discovered ABHD10 as a new member of *S*-palmitoylases, and characterized its activity in live cells, *in vitro* and by crystal structure.

ABHD10 is different from the other APTs thus far identified. While PPT1 is located in lysosomes, APT2 in the cytosol and the Golgi[13], ABHD17A, B and C in membranes[11] and APT1 in the cytosol, membrane, Golgi and the mitochondria[10,100], ABHD10 appears to be exclusively located in the mitochondria. Additionally, unlike APT1, our structural and biochemical data indicate that ABHD10 has an extensive 'cap' domain and also pos-

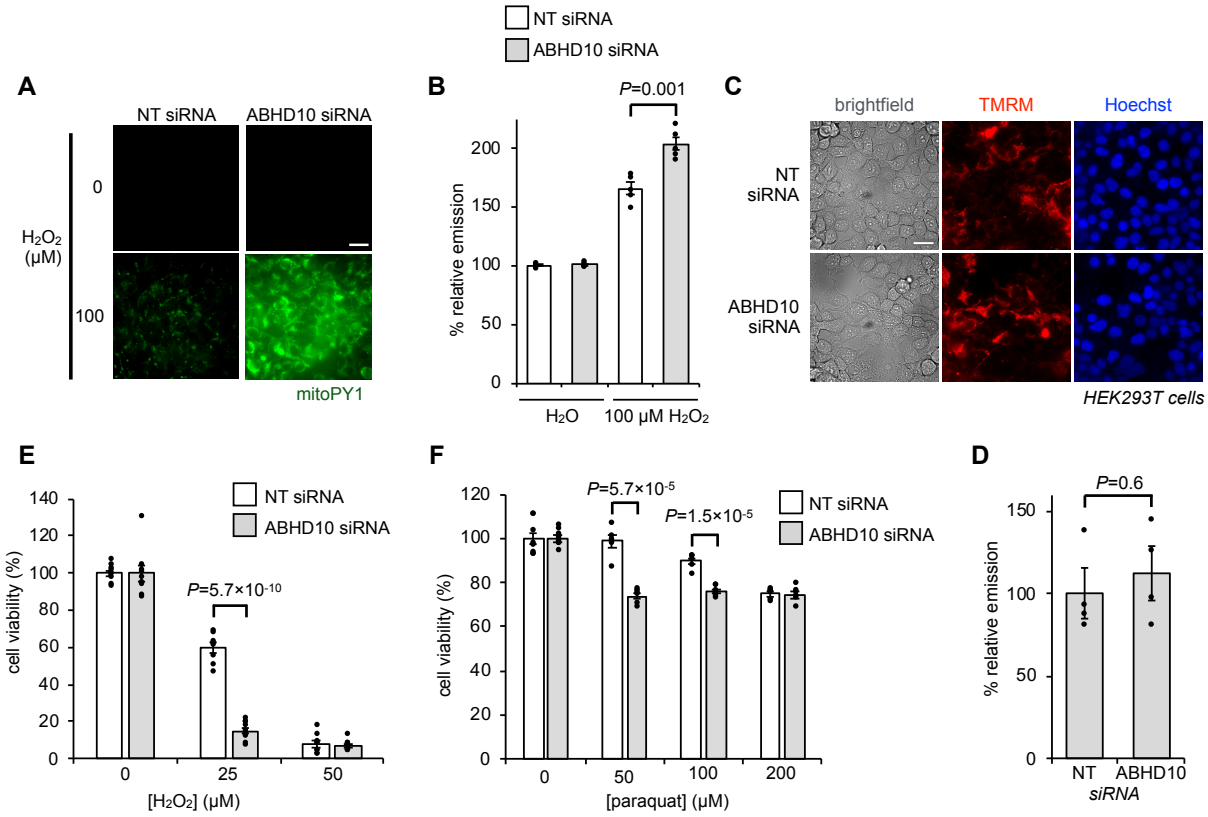

Figure 2.13 ABHD10 regulates *S*-palmitoylation of PRDX5 active site.
(A) Representative images showing ABHD10 knockdown diminishes the mitochondrial redox buffering capacity in HEK293T cells exposed to H_2O_2 as measured by epifluorescence microscopy using mitoPY1. 25 μm scale bar shown. **(B)** Quantification of the relative fluorescence intensity from mitoPY1 in each set of conditions shown in (A). n = 5 images. **(C)** HEK293T cells transfected with control or ABHD10 siRNA were stained by tetramethylrhodamine methyl ester (TMRM) to compare membrane potentials. 25 μm scale bar shown. n = 3 biological replicates. **(D)** Quantification of the relative fluorescence intensity from TMRM in each set of conditions shown in (C)). n = 4 images. **(E-F)** HEK293T cells transfected with either NT siRNA or ABHD10 siRNA were challenged with varying concentrations of H2O2 (E) or paraquat (F), and then analyzed for viability by the MTS assay. n is more than 6 biological replicates. Data expressed as mean ± SEM and normalized to control cells treated with NT siRNA. Statistical analyses performed with a two-tailed Student's t-test with unequal variance.

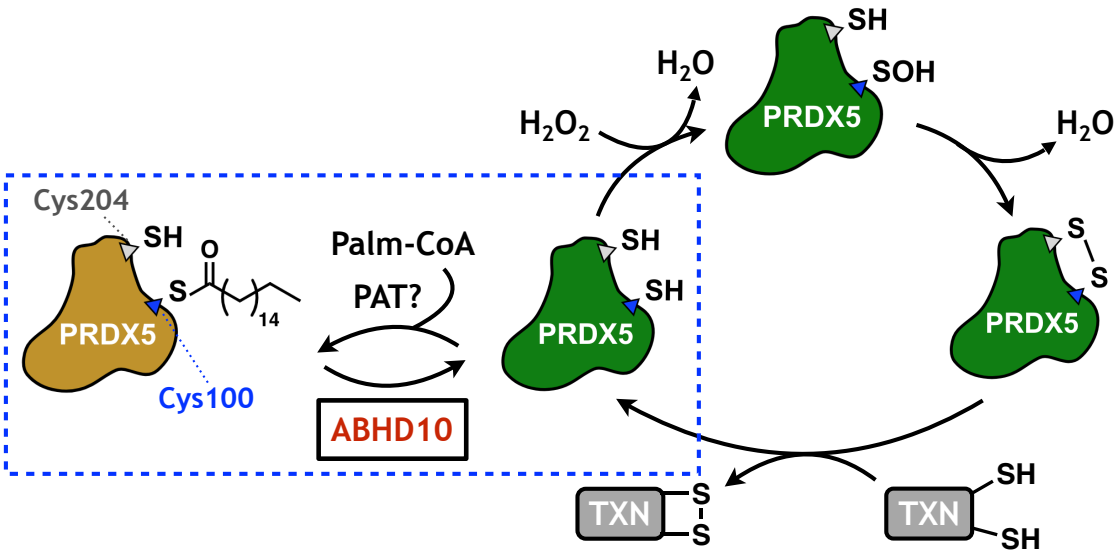

Figure 2.14 Schematic illustrating regulation of PRDX5 via ABHD10.
The active site cysteine of PRDX5 (Cys100) is blocked by *S*-palmitoylation, which is required to quench H_2O_2 for antioxidant activity. ABHD10-mediated *S*-depalmitoylation releases the active form of PRDX5, which then reacts with H_2O_2 in a disulfide-mediated redox cycling mechanism. TXN: thioredoxin.

sesses slower kinetic parameters than APT1 *in vitro*, suggesting more specific substrate recognition mechanisms. While we identified one substrate for ABHD10, it potentially has additional mitochondrial substrates. Recently developed libraries of synthetic palmitoylated peptide substrates could provide powerful methods to study the substrate specificity of ABHD10[101]. Although assigning natural substrates to APTs is often a challenge due to compensation between APTs and an incomplete understanding of regulatory elements, the addition of ABHD10 to the APT family could make this process now easier.

Mitochondria generate ROS byproducts, which can be both advantageous and deleterious[102]. Therefore, maintaining mitochondrial redox homeostasis is crucial for cellular health. Peroxiredoxins are the major regulators of H_2O_2 levels, due to their high reactivity towards peroxides. Since H_2O_2 is necessary at low levels but toxic at high levels, the PRDXs are tightly regulated by a variety of processes, such as phosphorylation, oxidation and nitrosylation[99]. Our finding that PRDX5 is regulated by *S*-palmitoylation modifica-

tion at the active site cysteine not only represents another direct mechanism for regulating PRDX activity, but is also a distinct example of *S*-palmitoylation directly modifying an enzyme active site[103]. Future work will involve identifying additional consequences of PRDX5 lipidation, including its impact on PRDX5 stability, trafficking and membrane localization. Our data presented here showed that PRDX3, another mitochondrial peroxiredoxin, is also lipidated, but is not regulated by ABHD10. This suggests that additional regulatory APTs exist along these pathways, warranting extensive further interrogation. This work focuses entirely on the erasers of *S*-palmitoylation, the APTs. However, equally important to the regulation of PRDX5 is the lipid installation. Although perturbation of both DHHC8 and 13 disrupts mitochondrial metabolic functions[87,88], no known writers have definitively been localized to the mitochondria. It is possible that PRDX5 is lipidated before mitochondrial import and then released in an active form once in the mitochondria. In this scenario, the lipid modification could be regulating PRDX5 trafficking to the mitochondria, as was previously observed for BAX[104]. However, there may also be DHHCs, or as yet undiscovered acyltransferases, present in or at the mitochondria that mediate PRDX5 lipidation. Future work exploring acyltransferase activity on these mitochondrial targets, likely involving the development of better chemical probes and inhibitors, will help to complete the regulatory picture of mitochondrial proteome *S*-palmitoylation.

2.4 Material and Methods

Reagents DMEM GlutaMAX (Gibco), Fetal Bovine Serum (FBS; Gibco/Life Technologies, Qualified US origin or Gemini Benchmark 100-106), Live Cell Imaging Solution (Molecular Probes), Opti-MEM (Gibco), Lipofectamine 3000 reagent (Invitrogen), Lipofectamine RNAiMAX transfection reagent (Invitrogen), polyethylenimine (PEI) (Sigma; average Mw 25,000 by LS, average Mn 10,000 by GPC, branched), Dynabead Protein G magnetic beads (Invitrogen) MitoTracker Deep Red FM (Invitrogen), Hoechst 33342

(Fisher), 2-BP (Sigma), MitoPY1 (Sigma), PY1 (Sigma), Palmostatin B (PalmB) (EMD Millipore), Charcoal-filter FBS (A3382101, Thermo Fischer), MTS (BioVision), Phenazine methosulfate (Sigma) were purchased as mentioned in parenthesis. siRNAs targeting human ABHD10 (SI04229519), human APT1/LYPLA1 (SI03246586) and human PRDX5 (SI00096971, SI02638888, SI02638902), as well as non-targeting (NT) control siRNA (SI03650325), were purchased from Qiagen. Silica gel P60 (40-63 µm, 230-400 mesh; SiliCycle) was used for column chromatography. Analytical thin layer chromatography was performed using precoated 60 F254 silica gel sheets (0.25 mm thick; SiliCycle). DPP-2[20], DPP-5[105] and mitoDPP-2[92] were synthesized as previously reported. All chemicals for synthesis were purchased from Sigma-Aldrich or Fisher Scientific and used as received. ML348 was purchased from Tocris (Bristol, UK).

Imaging For fluorescence microscopy, an inverted epifluorescence microscope (Lieca DMi8) equipped with a Hamamatsu Orca-Flash 4.0 camera, a 63x oil objective (N/A 1.4), and a 300 W Xenon light source (Sutter Lamda XL) was used. Leica LASX software was used to obtain images for mitoPY1/DPPs (YFP filter cube 1525306), Hoechst 33342 (ET 402/15x, Quad-S, ET 455/50m), MitoTracker (ET 645/30x, Quad-S, ET 705/72m) and brightfield.

Western Blotting After SDS-PAGE, proteins were transferred onto Immobilon-P PVDF membranes (pore size 0.45 µm; Milipore) using a semi-dry transfer cell (Bio-Rad). After transfer, the membranes were blocked for 1 hr with TBST wash buffer (20 mM Tris, pH 7.5, 150 mM NaCl, 0.1% Tween-20) containing 3% Bovine Serum Albumin (BSA; Fischer or Thermo Scientific). Consider the long procedure of the assay, we cut each membrane into several small membranes contains the target protein band based on the molecule weight. Each membrane was then incubated with primary antibody in 3% BSA-TBST. The membrane was washed with TBST 5 times for 5 min (5 x 5min) followed by 1 hr incubation

with either anti-rabbit IgG HRP or anti-mouse IgG_k BP-HRP in 3% BSA-TBST, washed 5x5min with TBST, and then visualized using SuperSignal West Pico PLUS chemiluminescent substrate (Thermo Scientific) and recorded on a chemiluminescent western blot imaging system (Azure Biosystems C300). Additional Western blots in this study were performed identically. For antibody dilutions and vendor information, see Supplementary **Table 2.2**.

Cell culture Unless otherwise stated, HEK293T (ATCC), HeLa (from Prof. Chuan He, University of Chicago) and HepG2 cells (from Cellular Screening Center, University of Chicago) were plated and maintained in DMEM GlutaMAX (supplemented with 10% Fetal Bovine Serum, and 1% Penicillin/Streptomycin) at 37 ℃ and 5% CO2. For all experiments, cells had undergone fewer than 25 passages and hence mycoplasma contamination was not tested. Cells were plated the day before all experiments. For all treatments, cells were first washed with fresh growth medium, which was then replaced with fresh growth medium containing the drug and/or probe. Where indicated, treatments also included Hoechst 33342 (1 μM) and MitoTracker Deep Red (100 nM) for nuclear and mitochondrial visualization, respectively. Transfections were conducted with either PEI (for plasmids), Lipofectamine 3000 (for plasmids) or Lipofectamine RNAiMAX (for siRNAs) according to the manufacturer's recommended protocols, which were scaled according to the volume of the culture dish.

Plasmid cloning All plasmids were constructed by Gibson Assembly from PCR products generated using Q5 Hot Start DNA Polymerase (New England Biolabs) or Phusion Polymerase (generated in-house). The pcDNA3 vector was a gift from Prof. Chuan He and pET-30a was used as described previously[20]. Genes for human PRDX5, human ABHD10, mouse ABHD10 and primers were synthesized by Integrated DNA Technologies, Inc (IDT). The cDNAs for PRDX5 and ABHD10 were cloned into the pcDNA3 vector

for mammalian expression. In addition, both human and mouse ABHD10 were truncated to remove the mitochondria localization signal peptide (residues 1-52 for human ABHD10 (Q9NUJ1-1) and 1-43 for mouse (Q6PE15-1), optimized using IDT Codon Optimizing Tool, and cloned into the pET-30a vector containing a His-tag for *E. coli* expression. All newly constructed plasmids were sequence-verified at the University of Chicago Comprehensive Cancer Center DNA Sequencing and Genotyping Facility and are available upon request.

Acyl Biotin Exchange (ABE) of cell culture samples *Volumes here are representative of an experiment using cells from a 10 cm plate.* HEK293T cells were washed with DPBS, lysed with 1 mL RIPA lysis buffer containing protease inhibitors (1 mM PMSF and 50 mM N-Ethylmaleimide (NEM, Acros)), and subject to end-over-end rotation overnight at 4 ℃. The cell debris was pelleted by centrifugation at 13000 xg for 15-30 min at 4 ℃ and the supernatant collected. Protein concentration was measured using BCA assay and equal amounts of total protein from each sample was subjected to acetone precipitation for 2 hr at -20 ℃. The resulting pellet was dissolved by sonication in 100 µL/mg protein of 4% SDS buffer (resuspension buffer; 150 mM NaCl, 50 mM HEPES, 5 mM EDTA, pH 7.4) containing 50 mM NEM. 250 µL/mg protein of 0.2% Triton buffer (150 mM NaCl, 50 mM HEPES, 5 mM EDTA, pH 7.4) containing 50 mM NEM was added and protein solution was rotated end-over-end for 3 hr at 25 ℃. Two subsequent acetone precipitations were performed to remove excess NEM. The resulting protein pellet was dissolved in 105 µL of resuspension buffer by sonication. The protein sample was divided into two equal parts for ± HA (hydroxylamine (Acros)) treatment in fresh 50 µL tubes. Each sample was treated with 150 µL of either –HA buffer (0.2% Triton buffer) or +HA buffer (0.2% Triton buffer containing 1.33 mM HA, pH 7.3). Samples were first incubated at room temperature with shaking for 1 hr, and then proteins were precipitated by chloroform-methanol precipitation to remove the excess hydroxylamine. Protein pellets were dried for 20-30 min at room

temperature and resuspended by sonication in 60 µL of resuspension buffer containing 10 µM EZ-Link HPDP-Biotin (Themo, 21341). Protein solutions were diluted with 240 µL Biotin buffer (0.2% Triton buffer, 10 µM EZ-Link HPDP-Biotin) and incubated for 2 hr at room temperature with shaking. Excess biotin was removed via acetone precipitation. Protein pellets were dissolved in 30 µL/mg protein of resuspension buffer by sonicating and total volume was brought to 1200 µL with 0.2% Triton buffer. Undissolved residues were removed via centrifugation at 14000 rpm for 5 min at 4 ℃. Protein concentrations were measured using BCA assay. 35 µg of protein was transferred to a fresh tube to serve as the loading control for normalizing levels of protein of interest ("input"). 350-400 ug protein was transferred to a new tube and diluted to 0.6-0.8 mg/ml with wash buffer (0.1% SDS, 0.2% Triton X-100, 150 mM NaCl, 50 mM HEPES, 5 mM EDTA, pH 7.4). 80 µL of streptavidin-agarose beads (Thermo, 20361) per mg of protein were added to the protein solution, which was then incubated at 4 ℃ overnight with end-over-end rotation. Unbound proteins were removed by washing 6x with 1 mL washing buffer and spinning for 1 min at 6000 rpm each time. Bound proteins were eluted by boiling the beads for 10 min at 95 oC with 1X Laemelli sample buffer (containing 20-30 mM DTT). The protein was resolved on 10% or 12% SDS-PAGE gels and subjected to Western Blotting protocol using the protocol described above.

Metabolic Labeling Volumes here are representative of an experiment using cells from a 10cm plate. HEK293T cells were washed with DPBS and then treated with 50 µM 17-ODYA absorbed on 5% BSA in DMEM GlutaMAX supplemented with 10% charcoal filtered FBS. Cells were then incubated for 6 hr unless noted differently at 37 ℃ with supply of 5% CO2. Cells were washed once in DPBS, lysed with 1 mL HEPES Lysis buffer (150 mM NaCl, 50 mM HEPES, 0.2% SDS, 1% Triton-100, pH 7.4, with EDTA-free Protease Inhibitor and 1mM PMSF) and subject to end-over-end rotation overnight at 4℃. The cell debris was pelleted by centrifugation at 13000 xg for 15-30 min at 4℃ and the

supernatant collected. Protein concentration was measured using BCA assay and 1 mg of protein was placed into a new tube. First, the same volume of HEPES buffer (150 mM NaCl, 50 mM HEPES, pH 7.4) was added in order to adjust the SDS concentration to 0.1% and then all samples were diluted with the click reaction buffer (150 mM NaCl, 50 mM HEPES, 0.1% SDS, 0.5% Triton-100, pH7.4) for a final protein concentration of 1 mg/ml. 88 µL of master mix made from 22 µL of each 5 mM Azide-PEG3-biotin (Sigma), 5 mM TBTA (Combi-Blocks), 50 mM CuSO4 and 5 mM TCEP was added for a 1 mL "Click" reaction. The resulting solution was incubated for 1 hr at room temperature with shaking. 121 µL of 100 mM EDTA was added to quench the "Click" reaction and proteins were precipitated by chloroform-methanol precipitation. Protein pellet was dissolved in 50 µL of resuspension buffer by sonicating and 150 µL of 0.2% triton buffer added. Protein was further precipitated by chloroform-methanol precipitation. The resulting protein pellet was dissolved in 105 µL of resuspension buffer by sonication. Protein samples were divided into two equal parts for ± HA (hydroxylamine) treatment by placing 50 µL into fresh tubes. Each sample was treated with 150 µl of either –HA buffer (0.2% Triton buffer) or +HA buffer (0.2% Triton buffer containing 1.33 mM HA, pH 7.3). Samples were first incubated at room temperature with shaking for 1 hr, and then proteins were precipitated by Chloroform-Methanol precipitation to remove the excess hydroxylamine. Protein pellets were dried for 20-30 min at room temperature and resuspended in 30 µL of resuspension buffer per mg protein by sonicating and total volume was brought to 1200 µL with 0.2% Triton buffer. Undissolved residues were removed by centrifugation at 14000 rpm for 5 min at 4℃. Protein concentrations were measured using BCA assay. 35 µg of protein was transferred to a fresh tube to serve as the "input" sample, as described above. 450-600 µg protein was transferred to new tube and treated as described for the ABE assay.

Assessment of mitochondrial H2O2 following APT1 or ABHD10 knockdown, and ABHD10 overexpression 140,000 HEK293T cells/well were plated in four well cham-

ber slides, as detailed above. After 18-20 hr, 150 µL of media was removed from each well and the cells were transfected with 12.5 pmol of siRNA targeting either APT1 or ABHD10. Control cells were transfected with NT siRNA following manufacture's conditions. 44-48 hr post-transfection, cells were pretreated with 2 µM mitoPY1 for 30 min at 37 ℃. Cells were then washed with DPBS and treated with fresh DPBS with or without 100 µM H_2O_2 for 10 min at 37 ℃. Images were obtained on an inverted epifluorescence microscope. Data analysis was performed as described above. Data was normalized to the average fluorescence intensity of the NT siRNA-transfected control that was not treated with H2O2. Each experiment was repeated in at least two biological replicates with identical results. Similar experiments were also done in HEK293T cells transfected with 600 ng of ABHD10 vector or control vector.

Epifluorescence-based genetic overexpression screen 16,000 to 18,000 HEK293T cells per well were plated in 96 well plates as described above. After 18-22 hr, cells were transfected with 80 ng of either empty vector plasmid or individual plasmids containing the protein targets. 40-44 hr post-transfection, the media was replaced with 100 µL of fresh media containing 1 µM Hoechst 33342 and 100 nM MitoTracker Deep Red. After 30 min, the cells were washed with 100 µL of Imaging Buffer and 70 µL of 1 µM DPP-2 in fresh Imaging Buffer was added to the cells. Cell were incubated for 10 min at 37 ℃ and then imaged from 25 min onwards on an inverted epifluorescence microscope set on automated focus mode. Multiple images from two biological replicates were used for analysis. Data analysis was performed as described above, and the data was normalized to the average fluorescence intensity of the empty vector plasmid transfected control cells.

Imaging with mitoDPP-2 140,000 HEK293T cells/well were plated in four-well chamber slides as described above. After 18–20 h, the cells were transfected with 600 ng of either pcDNA3-ABHD10(WT) or -ABHD10(S152A). Control cells were transfected with

the empty pcDNA3 vector backbone. 32–35 hr post-transfection, nuclei and mitochondria were stained with Hoechst 33342 and MitoTracker Deep Red, respectively, for 30 min at 37 ℃. Cells were then briefly washed with imaging solution, and probed with 500 nM mitoDPP-2 in fresh imaging solution. After 10 min at 37 ℃, images were obtained on an inverted epifluorescence microscope, and data analyses were performed as described above. For data analysis, the average fluorescence intensity per image in each experimental condition was obtained by gating cells using the brightfield image, and applying that mask to the corresponding MitoTracker and mitoDPP-2 image. Eight images from two biological replicates were used to quantify the images, and the data was normalized to the average fluorescence intensity of the MitoTracker channel of cells transfected with the empty vector plasmid.

Measurement of mitochondria membrane potential by TMRM For assessing mitochondrial membrane integrity in HEK293T, cells were plated, treated as described above and replaced with fresh growth media containing 1 µM Hoechst 33342 and 100 nM TMRM. Cells were then incubated at 37 oC for 30 mins, washed and replaced with 400 µL imaging solution. Images were obtained on an inverted epifluorescence microscope using TRITC/RFP filter settings, and data analyses were performed as described above. Eight images from two biological replicates were used to quantify the images, and the data was normalized to the average fluorescence intensity of control cells.

***In vitro* kinetic assay of APTs following mitoFP-mediated inhibition** Biochemical assays with purified APT1 or ABHD10 enzymes were performed on a Biotek synergy Neo2 plate reader. 100 nM APT1 or ABHD10 was incubated for 30 min at 37℃ with 1.2, 2.4, 6, 12, 24, 60, or 120 µM mitoFP equal in HEPES buffer (20 mM, pH = 7.8, 150 mM NaCl). Controls were incubated with an equal volume of DMSO. At the end of 30 min, the incubated APT1 or ABHD10 solutions (150 µL) were added to a 96-well optical

bottom plate (Nunc 265301, Thermo Scientific) at room temperature. Wells containing HEPES buffer alone served as negative controls. Using a multi-channel pipette, 150 µL of a solution of 2 µM DPP-5 in HEPES buffer was added, for a final concentration of: 1 µM DPP-5; 50 nM enzyme; and 0, 0.6, 1.2, 3, 6, 12, 30, or 60 µM mitoFP. Fluorescence intensities (λex 490/20 nm, λem 545/20 nm, Gain 80, read from bottom with height 4.5 mm, and sweep method) were measured at 15-sec time intervals for 30 min at 37 ℃. Incubations of 12 µM PalmB with 100 nM APT1, and 6 µM PalmB with 100 nM ABHD10 were run in parallel and served as positive controls. The initial velocity is calculated from linear regression of first 20 data points of APT1 and first 30 data points for ABHD10 (n=4) and the one phase exponential decay analysis (*Y=Span*exp(-K*X) + Plateau*) was done using GraphPad Prism version 6.0e.

Purification of recombinant ABHD10 BL21 competent *E. coli* were transformed with both the pGro7 chaperone plasmid and plasmids encoding transit peptide cleaved human ABHD10 (either WT or S152A) or mouse ABHD10. The cells were cultured in 500 mL 2x YT media with 33 µg/ml chloramphenicol, 40 µg/ml kanamycin and 0.5 mg/ml L-arabinose in a 2 L flask shaking at 37 ℃ until OD600 reaches 0.6, at which point 1 mM IPTG was added. Cultures were then grown at 25 ℃ for an additional 20 hr. Bacteria was harvested by centrifugation and lysed by sonication in 25 mL lysis buffer (50 mM Tris, 1 M NaCl, 20% glycerol, 10 mM TCEP, pH 7.5). Cell debris was discarded and the lysis supernatant was incubated with 1 mL Takara His60 Ni Superflow Resin with gentle rotation at 4 ℃ for 1 hr. The His-tagged proteins were purified using a standard protocol of washing and eluting the resin with wash buffer-1 (20 mM imidazole, 50 mM Tris, 1 M NaCl, 20% glycerol, 10 mM TCEP, pH 7.5), wash buffer-2 (40 mM imidazole, 50 mM Tris, 1 M NaCl, 20% glycerol, 10 mM TCEP, pH 7.5) and elution buffer (300 mM imidazole, 50 mM Tris, 1 M NaCl, 20% glycerol, 10 mM TCEP, pH 7.5). The purified proteins were then desalted on GE Disposable PD-10 Desalting Columns and stored in the protein storage buffer (50 mM

Tris, 100 mM NaCl, 2 mM TCEP, 50% Glycerol, pH 7.5). The purity of the elution fractions was validated by 12% SDS–PAGE gel. Purified proteins were stored in individual aliquots in protein storage buffer at -20 °C (for more immediate use) or -80 °C (for long-term storage).

***In vitro* kinetics of recombinant human and mouse ABHD10** 150 µL of 10 µM DPP-5 in HEPES (20 mM, pH = 7.8, 150 mM NaCl) were added to the 96-well optical bottom plate. 150 µL of either HEPES buffer alone or HEPES buffer containing 1 µM proteins (human, mouse or S152A variant ABHD10, purified as described above) were added using a multi-channel pipette, resulting in a final concentration of 5 µM DPP-5 and 500 nM proteins. Fluorescence intensities (λ_{ex} 490/20 nm, λ_{em} 545/20 nm, Gain 50, read from bottom with height 4.5 mm, and sweep method) were measured at 1 min time intervals for 12 h at 37 °C. The Michaelis–Menten kinetics regression analysis was done using GraphPad Prism version 6.0e.

Crystallization of truncated mouse ABHD10 Mouse ABHD10 was purified from Ni-resin as described above. Mouse ABHD10 was solubilized in Buffer A (20 mM Tris, pH 8.0) with PD-10 Desalting Columns and loaded onto a Q Sepharose Ion-Exchange column for gradient-elution with Buffer B (1 M NaCl, 20 mM Tris, pH 8.0). Fractions were collected and verified by 12% SDS-PAGE. Pure fractions were combined and loaded onto a Superdex 200 Increase 10/300 GL column (GE Healthcare Life Sciences). The fractions eluted by SEC Buffer (10 mM Tris, 50 mM NaCl, pH 8.0) were again verified by SDS-PAGE and concentrated to 35 mg/ml. The pure protein was then aliquoted, flash frozen in liquid nitrogen and stored at -80 °C. The crystallization was performed using the hanging drop vapor diffusion technique. The high-throughput screening of crystallization conditions was set up by a Mosquito Crystallization Robot (TTP Labtech) at 4 °C using commercially available screening kits from Hampton Research Corp. The best crystals

were obtained from 25 mg/mL proteins mixed with the precipitant solution from Natrix 2 (0.08 M strontium chloride hexahydrate, 0.04 M sodium cacodylate trihydrate pH 6.0, 35% v/v (+/-)-2-methyl-2,4-pentanediol (MPD), 0.012 M spermine tetrahydrochloride). Following optimization of pH at 6.4 and precipitant concentration at 25%, crystals were grown in the 2 µL of 1:1 protein and buffer solution mixture drops hanging on siliconized glass slides, harvested by soaking the cryo buffer (same as precipitant buffer except that the MPD concentration increased to 50%), and flash-frozen in liquid nitrogen.

X-ray diffraction data collection and refinement The X-ray diffraction data were collected at the Advanced Photon Source NE-CAT section beamline 24-ID-C at 100K in Argonne National Laboratory (X-ray wavelength 0.97910 Å). All the datasets were then integrated and scaled using (https://rapd.nec.aps.anl.gov/rapd/), its on-site RAPD automated programs. The asymmetric unit contained one molecule and the structure was solved by Molecular Replacement (MR). Initial phases were obtained with Phaser[106] using a structure predicted by RaptorX (http://raptorx.uchicago.edu/)[107,108], based on template 3LLC.pdb. The structure building and refinement were completed by AutoBuild and phenix.refine in Phenix[109] and by manually modeling in the program COOT[110] according to weighted |2Fo|-|Fc| and |Fo|-|Fc| maps. Thermal parameters were handled as individual isotropic B-factors with one overall TLS (translation, libration and screw) group. One well-ordered MPD molecule was found within a pocket in the protein, and 4 strontium ions were found at the surface, 3 of them mediating crystal packing. The identity of the strontium ions was confirmed with an anomalous difference Fourier. The Ramachandran favored residues are 98% with 0% outliers.

Cell viability experiment For the H_2O_2 experiment, HEK293T or HeLa cells transfected with NT siRNA or ABHD10 siRNA for 24 hr were replated into a 96-well plate. After 24 hr, the media was replaced with 200 µL pyruvate-free DMEM GlutaMAX (10% FBS)

containing either H2O or 25 or 50 μM H_2O_2. After 36 hr incubation at 37℃, the media was replaced with 200 μL 1x MTS reagent (10x PBS stock solution containing 0.6 mM MTS and 0.033 mM Phenazine methosulfate, pH 5.2-5.4)57 in DMEM GlutaMAX, and incubated at 37 ℃ for 1-2 hr. The plate was then gently shaken and absorbance was measured at 490 nm using a plate reader. Cells treated with NT or ABHD10 siRNA and no H2O2 was set to 100% viability. Each group of cells with various concentrations of H_2O_2 is normalized to respective cells treated with H2O as follows:

$\%\ \text{Cell viability}_{(c)} = A_{(c)} / A_{(0)} * 100$

$A_{(\text{Average absorbance at concentration c})}$

$A_{(\text{Average absorbance at concentration 0})}$

For the paraquat experiment, HEK293T cells transfected with NT siRNA or ABHD10 siRNA for 24 h were replated into a 96-well plate. After 24 hr, the media was replaced with 200 μL pyruvate-free DMEM GlutaMAX (10% FBS) containing either H2O or 50, 100, or 200 μM aqueous paraquat. After 12 h at 37 ℃, the media was replaced with 200 μL of pyruvate-free DMEM GlutaMAX (10% FBS). 24 h later, the media was replaced with 200 μL 1x MTS reagent (10x PBS stock solution containing 0.6 mM MTS and 0.033 mM Phenazine methosulfate, pH 5.2-5.4) in DMEM GlutaMAX, and incubated at 37 ℃ for 1 h. The plate was then gently shaken and absorbance was measured at 490 nm using a plate reader. Quantification was performed as described above.

2.5 Supplementary Information

Table 2.2 List of the antibodies used in Chapter 2.

Protein	**Species**	**Dilution**	**Cat. No.**
Calnexin	Rabbit	1:4000	ab22595 (Abcam)
ABHD10	Rabbit	1:1000	ab214085 (Abcam)
ABHD10	Rabbit	1:1000	HPA036991 (Sigma)
APT1	Rabbit	1:1000	ab91603 (Abcam)
APT2	Rabbit	1:1000	ab151578 (Abcam)
PRDX5	Rabbit	1:1000	17724-1-AP (Proteintech)
PRDX3	Rabbit	1:1000	Ab73349 (Abcam)
FLAG	Mouse	1:1000	MA1-91878 (Invitrogen)
ALDH6A1	Mouse	1:1000	sc-365160 (Santa Cruz Biotechnology)
Streptavidin-HRP	Goat	1:2000	3999S (Cell Signalling Technology)
Alpha-Tubulin-HRP	Goat	1:2000	hrp-66031 (Proteintech)
Anti Rabbit IgG-HRP	Goat	1:4000	7074S (Cell Signalling Technology)
Anti Mouse IgGk BP-HRP	Goat	1:4000	sc-516102 (Santa Cruz Biotechnology)

CHAPTER 3

RNA-BASED TRANSLATION ACTIVATORS TO AMPLIFY TARGETED GENE EXPRESSION IN MAMMALIAN CELLS

3.1 Introduction

Insufficient expression of critical proteins, triggered by gene deletions, genetic mutations, or expression downregulation by pathological conditions, causes substantial human diseases. While technologies for the inhibition, blockade, degradation, or sequestration of overproduced gene products have established a diverse palette of therapeutic modalities, technologies to activate gene expression are comparably underdeveloped.

Recent innovations in nucleic acid-based therapeutics (NBTs) have provided new opportunities for upregulation of disease-associated proteins[33]. Technologies that increase productive RNA levels, including TANGO (targeted augmentation of nuclear gene output), which prevents the inclusion of toxic exons[62]; AntagoNATs (single-stranded NAT-specific oligonucleotides), which inhibit natural antisense transcripts[67]; and saRNAs (small activating RNAs), which activate transcription[50], are either advancing towards or have already reached clinical stages. Compared to the overall successes of mRNA-increasing technologies, those that directly modulate protein translation are comparably lagging.

Activating gene expression at the translation process – by boosting protein production from endogenous mRNAs – should be suitable for a broad range of mRNAs with different lengths and characteristics. Existing antisense oligonucleotides (ASO)-based translation activators, which block either upstream AUG regions[40] or inhibitory elements in 5' UTRs[39], have therapeutic potentials, but cannot target transcripts without such specific regulatory elements. Long-noncoding RNA (lncRNA)-based translation activators are generally too long for oligo synthesis and chemical modifications, thus presenting unsatisfactory pharmacokinetic properties. Importantly, translation activators based on lncRNA

require binding domains overlapping the translation initiation sites in target transcripts, which makes them unsuitable for many mRNA targets[77].

In this chapter, I describe the development of "translation activating RNA" (taRNA), a platform of RNA molecules that activate the translation of a wide range of mRNAs of interest in mammalian cells. taRNAs are bifunctional molecules, made from a guide sequence domain that binds to the 3' UTR of the target mRNA and an effector domain that recruits translation machinery. The effector domain can be selected from a collection of RNA elements, which we mined from viral[111] and eukaryotic natural internal ribosome entry sites (IRESs)[112]. We show that taRNAs can increase protein synthesis from a variety of mRNAs in human and mouse cells, including disease-related haploinsufficiency targets such as *SYNGAP1* and *PMP22*. Through truncation of the effector domain, we not only reduced effector size, but also revealed eIF3 and eIF4G as the key initiation factors needed to enhance targeted mRNA translation. Collectively, our taRNA technology provides a customizable RNA-based platform for elevating gene expression from various endogenous mRNAs, opening up new possibilities for therapeutic design.

3.2 Results

3.2.1 Design of a translation-activating RNA platform (taRNA)

We designed taRNAs as bimodular molecules, consisting of a programmable guide RNA domain that complements the target mRNA, and an effector domain that recruits translation machinery (**Figure 3.1**). To break away from the strict limitation for 5' UTR binding sites of the existing technologies, we proposed taRNAs to instead target the 3' UTR. The 3' UTRs of mammalian mRNAs are generally longer than 5' UTRs[113], providing more flexible choices for gRNA design and optimization, also allowing synergetic effects and potential transcript-isoform specificity.

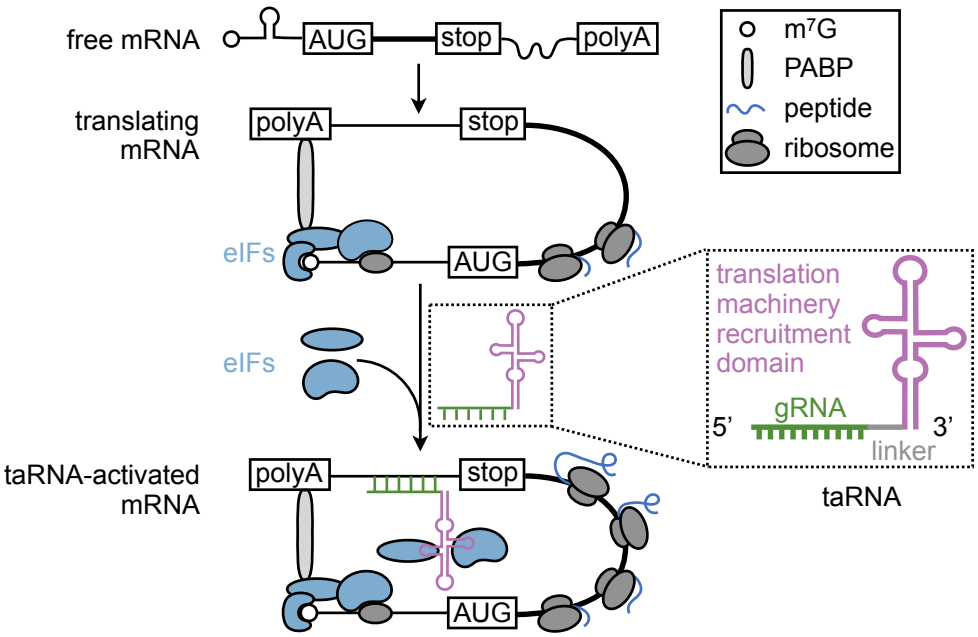

Figure 3.1 Schematic overview of taRNA technology.
The taRNA molecule is made of a target-specific guide RNA domain (gRNA, green), a translation machinery-recruitment domain (purple) and a linker (gray) in between. Initiation factors (eIFs, blue) are recruited by taRNAs to further activate targeted mRNA translation. Poly(A)-binding protein (PABP, light gray) interacts with initiation factors, and poly-A tail on mRNA.

To identify suitable RNA-based effector domains, we mined from IRESs, which can directly bind to eukaryotic initiation factors (eIFs)[114]. Initiation is the rate-limiting step for eukaryotic mRNA translation[115], and recruiting eIFs to the 3' UTR naturally[116], or artificially by RNA-targeting technologies[117–119], has been shown to enhance target protein production. Although IRESs are only found as *cis*-acting elements to initiate translation of downstream coding regions[120], there are IRES-like RNA elements, Cap-Independent Translation Enhancers (CITE), from plant virus[121], and synthetic IRES inserted into reporter vectors proved functional in the 3' UTR[122]. Thus, we reasoned that IRESs may be engineered as separately delivered therapeutics, to recruit eIFs to the 3' UTR of an mRNA of interest by a guiding sequence and boost translation.

To test initial taRNA designs, we adopted a dual-luciferase reporter (DLR) assay[117],

in which Firefly luciferase (Fluc) contains a weak Kozak sequence for an optimal response to translation initiation alteration[123] (**Figure 3.2**), and used a previously characterized guide sequence[117,118] to target the 3'UTR of the Fluc mRNA. The taRNA vector is lipofected into cell lines together with DLR to assess the upregulation efficacy of each taRNA design.

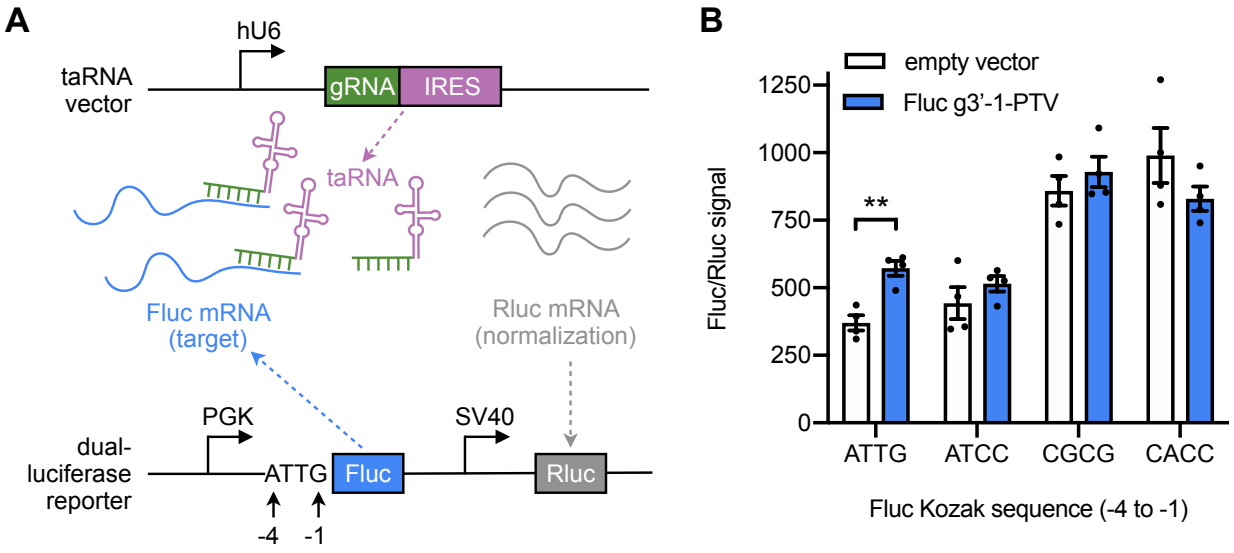

Figure 3.2 Dual-luciferase reporter assay to test taRNA activity.
(A) Schematic of vectors for taRNA and reporter used in dual-luciferase (DLR) assay. The taRNA (green and purple) targets Firefly luciferase mRNA (Fluc, blue), while Renilla luciferase (Rluc, gray) serves as the internal control. ATTG is part of the Kozak sequence of the Fluc mRNA at position -4 to -1 before the start codon. The hU6 (human U6), PGK (phosphoglycerate kinase 1) and SV40 (simian vacuolating virus 40) indicate different promoters to drive downstream transcription. **(B)** Dual-luciferase reporters containing weaker Kozak sequences for Fluc respond more significantly to activation. The Kozak sequences containing ATTG, ATCC and CGCG are listed by increasing strength. CACC is part of the canonical Kozak sequence (position -4 to -1). The Fluc g3'-1- PTV taRNA (blue), together with the empty vector control (white), was used to evaluate these reporters. n = 4 biological replicates. All bar-graph values are shown as mean ± SEM with individual data points. Statistical analyses were performed using two-way ANOVA with Sidak's multiple comparisons test. $^{*}P < 0.05$, $^{**}P < 0.01$, $^{***}P<0.001$, $^{****}P<0.0001$. No asterisk means not significant.

3.2.2 Selected IRESs can serve as effector domains for taRNAs

To evaluate the effector domain capability of IRESs, we selected representatives from each of the four major classes of viral IRESs[111] and eukaryotic IRESs[112] (**Figure 3.3**). Viral IRESs are classified by their secondary structures and recruitment patterns of ribosomes and eIFs. Briefly, the Class 1 and 2 IRESs recruit almost the entire set of translation initiation factors[124]. The Class 3 IRESs are known to directly bind to 40S ribosomal subunit and eIF3[125]. The Class 4 IRESs do not require any initiation factors[126].

IRES	Class	Length	Initiation factors recruited
CrPV IRES	4	204 nt	NA
HCV IRES	3	302 nt	eIF3, eIF2
PTV-1 IRES	3	287 nt	eIF3, eIF2
EMCV IRES	2	463 nt	eIF4G, eIF4A, eIF4B, eIF3, eIF2
FMDV IRES	2	458 nt	eIF4G, eIF4A, eIF4B, eIF3, eIF2
PV IRES	1	635 nt	eIF4G, eIF4A, eIF4B, eIF3, eIF2
c-myc IRES	endogenous	352 nt	not confirmed

Figure 3.3 IRESs tested in this chapter.
Summary of the classification, length of different IRESs, and the translation initiation factors known to be recruited by each IRES tested in this chapter.

In our first designs, we fused the aforementioned 40-nt Fluc guide RNA (g3'-1) or non-targeting gRNA (NT) and a 5-nt linker to the 5' end of each IRES element, which is often flexible and tolerant of modification[127]. We expressed each putative taRNA as vector in DLR assay in HEK293T cells and found taRNAs with IRESs derived from viral IRES Class 1, 2, and 3, and from endogenous c-myc mRNA, increase targeted Fluc

protein, when compared to the empty vector and non-targeting (NT) negative controls (**Figure 3.4A and B**). At the same time, the taRNAs didn't alter relative Fluc mRNA levels (**Figure 3.4C and D**), demonstrating activation of Fluc expression was through translation upregulation, instead of increase on mRNA abundance. Notably, a Class 4 IRES from Cricket Paralysis Virus (CrPV), which directly binds to the 40S ribosome without eIFs[128], fail to elevate Fluc expression. This indicates the recruitment of eIFs are important for the taRNA function. The putative taRNAs were tested by DLR assay again in HepG2 and MDA-MB-231 cell lines, comfirming the activity of taRNA across different cell lines (**Figure 3.4E and F**). Together, these data support the hypothesis that IRESs can be engineered to recruit eIFs in trans at the 3' UTR of a target mRNA, validate the taRNA design strategy for translation upregulation, and provide a set of RNA elements to serve as diverse taRNA scaffolds.

3.2.3 Characterization of the guide RNA domain

Based on the initial screening, the taRNA built with PTV-1 IRES (PTV) was the most effective and was therefore selected for further characterization (**Figure 3.5A**). To probe whether the 3'UTR was the most suitable gRNA landing region, we tested gRNAs targeting the 5' UTR (g5'), CDS (gCDS-1 to gCDS-5), or 3' UTR (g3'-1 and g3'-2) of Fluc mRNA. Among these, the g5', gCDS-1 and g3'-1 were previously verified to be effective binding sites for protein-based technologies[117]. Both 3' UTR-targeted taRNAs showed the most potent activation (**Figure 3.5B**), thus confirming the 3' UTR as the preferred region for taRNA targeting. Finally, different lengths of guide domain for PTV-based taRNAs were assessed, showing gRNA between 30 nt to 50 nt were effective (**Figure 3.5C**).

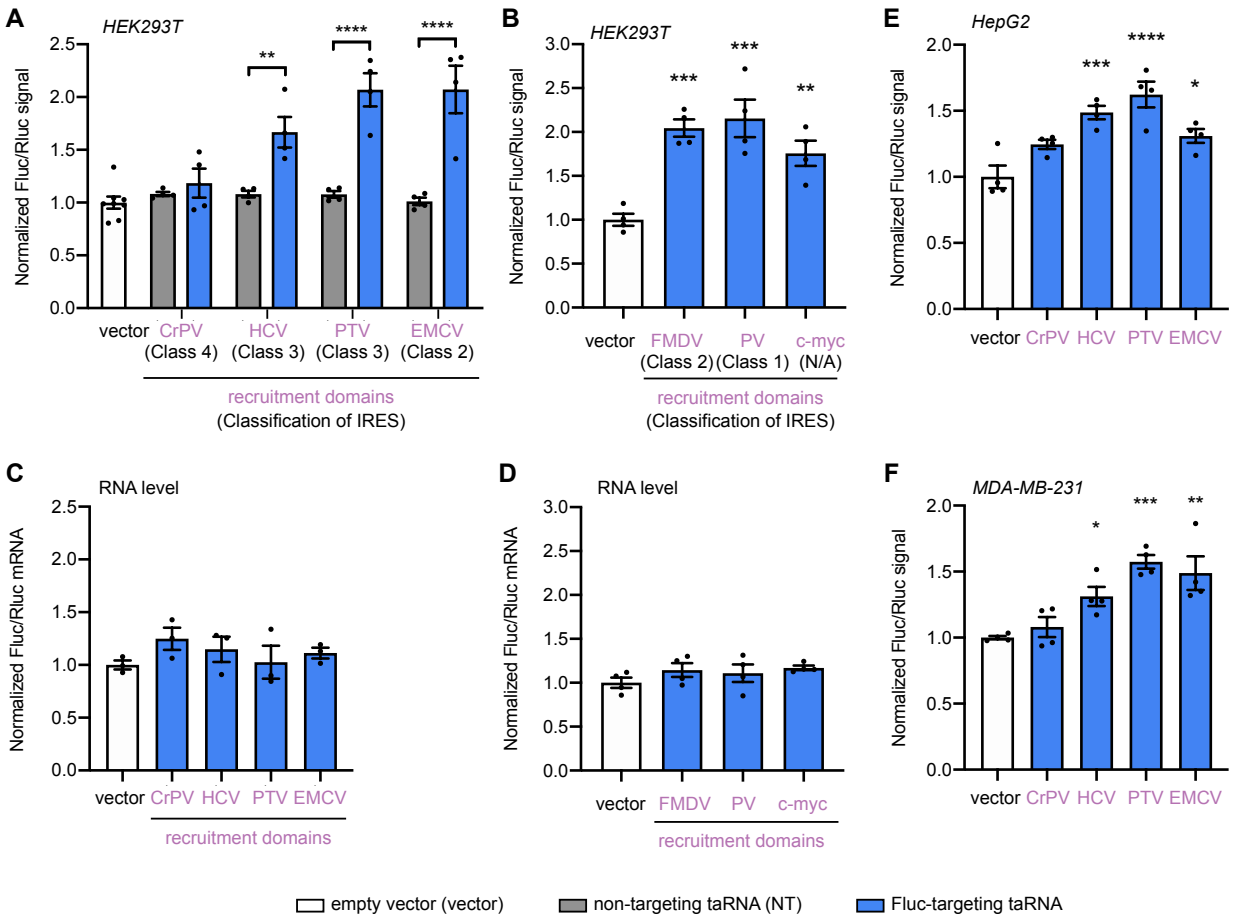

Figure 3.4 Selected IRESs tested as taRNA effector domains via DLR assay.
(A) Each IRES was tested as putative effector domain by attachment to either a non-targeting gRNA (gray) as negative control, or an Fluc-targeting gRNA (g3'-1, blue), by DLR assay in HEK293T cells. Viral origin and classification are listed for each IRES. Data were normalized to empty vector group. n = 4 biological replicates. **(B)** Additional IRESs from Class 2 (FMDV), Class 1 (PV) and human c-myc mRNA were tested by DLR assay in HEK293T cells. Data were normalized to empty vector group. n = 4 biological replicates. **(C, D)** RNA level of Fluc relative to Rluc in HEK293T cells after Flu-targeting taRNA treatment (g3' -1, blue) measured by RT-qPCR. Data were normalized to empty vector group. n = 3 biological replicates. **(E, F)** The taRNAs based on CrPV, HCV, PTV-1 and EMCV IRESs were tested by DLR assay in HepG2 cells (E) and in MDA-MB-231 cells (F). n=4 biological replicates. All bar-graph values are shown as mean ± SEM with data points. Statistical analyses: (A) two-way ANOVA with Sidak's multiple comparisons test between non-targeting and Fluc-targeting taRNA; (B-F) one-way ANOVA with Dunnett's multiple comparison test vs. vector.

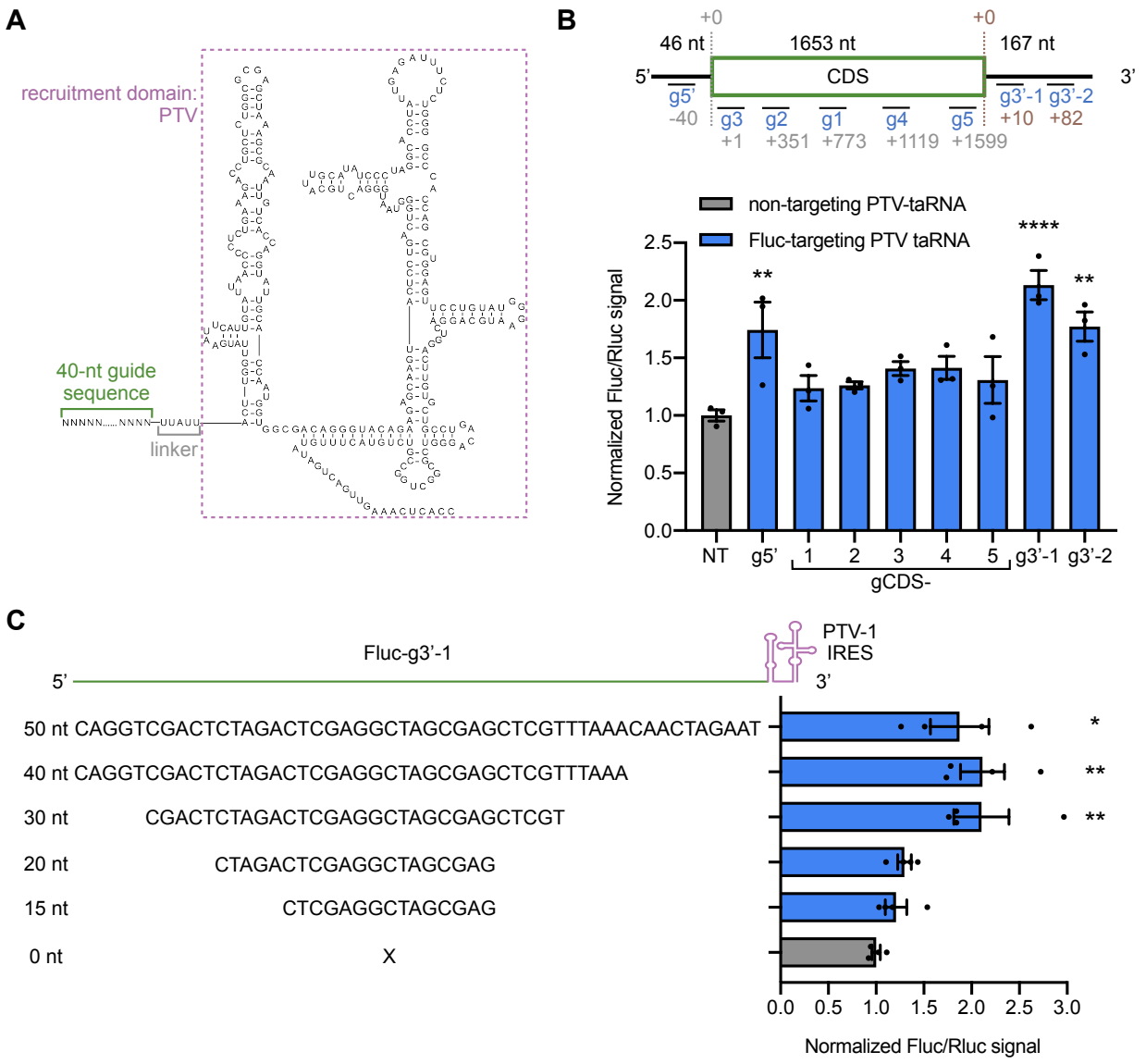

Figure 3.5 Characterization of the guide domain on PTV-based taRNA via DLR assay in HEK293T cells.

(A) Secondary structure of taRNA based on PTV-1 IRES shown as nucleotide sequence. **(B)** A panel of 5' UTR, CDS and 3' UTR-targeting gRNAs for Fluc were tested as PTV-based taRNA in DLR assay. The gRNA is annotated as where their 3' end nucleotide binds on Fluc transcript, relative to the start codon (+0, gray) or to the stop codon (+0, brown). Data were normalized to NT control. n = 4 biological replicates. **(C)** Evaluation of different lengths of Fluc-g3'-1 gRNA. Data were normalized to 0 nt (PTV alone without gRNA, gray). n = 4 biological replicates. Statistical analyses were performed using one-way ANOVA followed by Dunnett's multiple comparison test vs. control.

3.2.4 taRNAs promote the translation of target endogenous mRNAs in mammalian cells

A small panel of endogenous mRNAs in HEK293T cells was selected to validate the generality of PTV-based taRNAs. This panel of mRNAs includes: the well-studied tumor suppressor, phosphatase and tensin homolog (PTEN); the highly expressed peptidylprolyl isomerase B (PPIB); the 18kDa cell cycle regulator, Cyclin-dependent kinase inhibitor 1 (CDKN1A); and the 234 kDa transmembrane phospholipid-transporting ATPase ABCA7 (ABCA7), whose deficiency contributes to Alzheimer's disease[129]. We designed two gRNAs on or near the 3' UTR for each target, none of which contain stable internal secondary structures, predicted off-targets or RNA polymerase III termination signals. We lipofected HEK293T cells with taRNA-expressing vectors to assay the ability of the resultant taRNAs to activate target protein production by Western blotting. Across all targets, at least one of the two gRNA designs enhanced target protein production as compared to the NT control (**Figure 3.6A-D**), without affecting mRNA levels (**Figure 3.6E-H**).

To directly prove that taRNA upregulate the translation process, polysome profiling was performed on HEK293T cells lipofected with g2(PTEN)-PTV taRNA or empty vector (**Figure 3.7A**). Quantification of PTEN mRNAs in different pooled fractions – monosomes (F3-4), light polysomes (F5-7) and heavy polysomes (F8-11) – by RT-qPCR revealed taRNA treatment increased the relative number of PTEN mRNAs within the heavy polysome fractions, confirming that taRNA treatment results in more target transcripts undergoing active translation (**Figure 3.7B**). Additionally, since the total amount of PTEN mRNAs was not affected by g2(PTEN)-PTV (**Figure 3.6E**), the overall increase in the proportion of PTEN-mRNAs that are ribosome-bound suggests that taRNA treatment promotes the engagement of translational machinery with target transcripts.

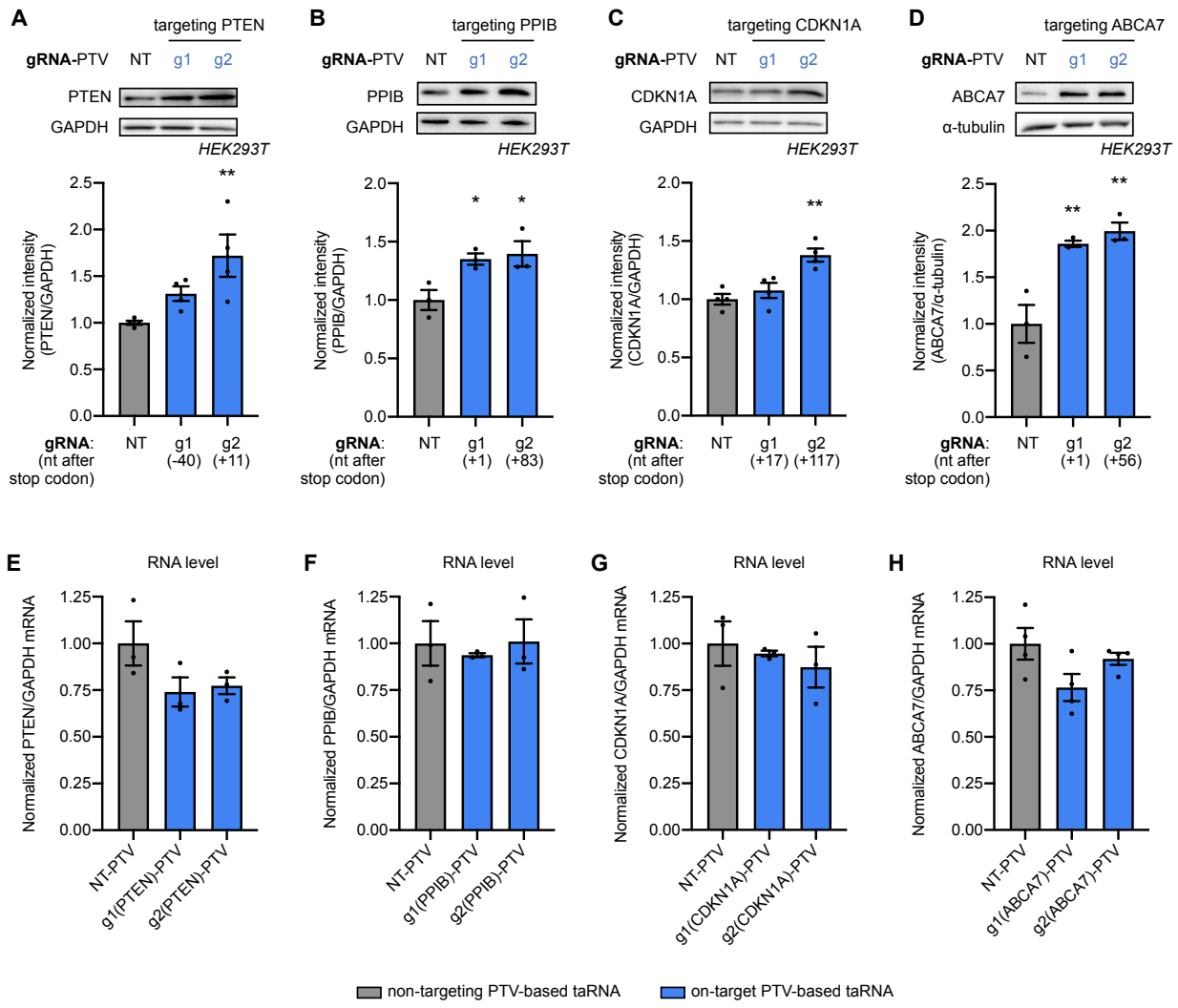

Figure 3.6 taRNAs enhance endogenous mRNA translation in HEK293T cells. **(A-D)** Two on-target gRNAs were tested in PTV-based taRNAs (blue) for each endogenous mRNA target, (A) human PTEN; (B) human PPIB; (C) human CDKN1A; (D) human ABCA7. gRNA is annotated with where their last nucleotide binds relative to the stop codon on the target transcript. Representative blots were shown as top panels with GAPDH or α-tubulin as the loading control. Quantifications of intensity were normalized to non-targeting control (NT, gray). **(E-H)** RT-qPCR measurement proved on-target taRNAs caused no significant changes on target RNA level compared to non-targeting taRNAs. n = 3-4 biological replicates. Statistical analyse were performed using one-way ANOVA followed by Dunnett's multiple comparison test vs. NT control.

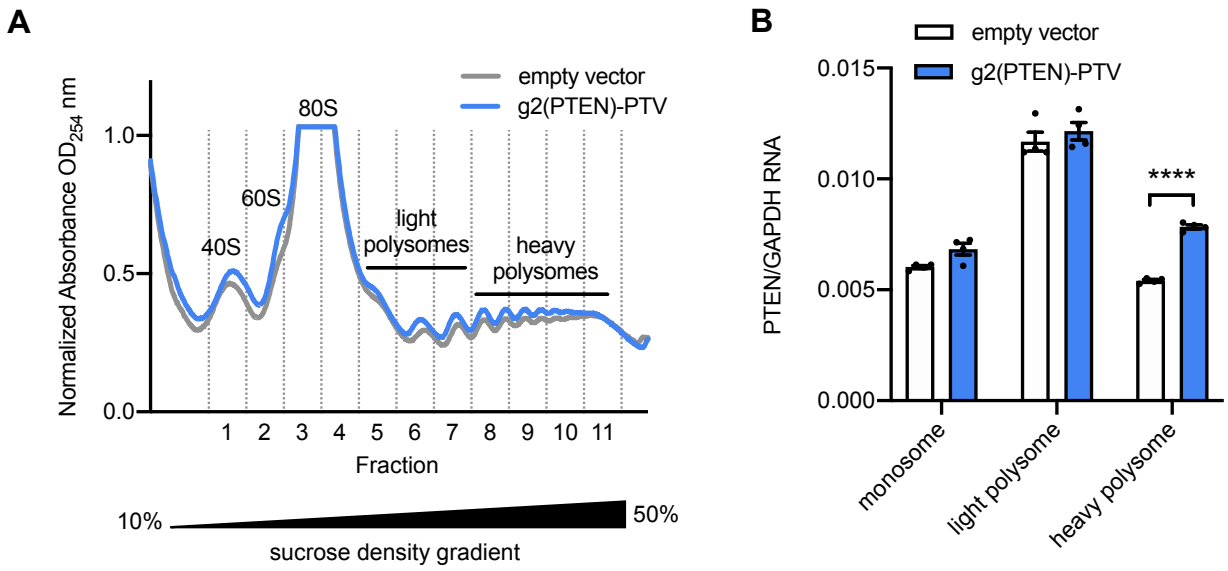

Figure 3.7 taRNAs enhance endogenous mRNA translation in HEK293T cells. **(A)** Absorption profiles of ribosomes from HEK293T cells treated with either empty vector (gray) or g2(PTEN)-PTV (blue). Sucrose gradient seperated mRNAs into fractions bound with 80S (monosome), 2-4 ribosomes (light polysomes) and 5+ ribosomes (heavy polysomes). **(B)** Pooled fractions from (A) were analyzed for PTEN RNA level by RT-qPCR, normalized to GAPDH. n = 4 technical replicates. Statistical analysis was performed using two-way ANOVA followed by Sidak's multiple comparisons test vs. empty vector.

3.2.5 Mechanistic interrogation via effector domain truncations

Although IRESs are functional effector domains, the resulting taRNAs are still relatively large (332 nt). We therefore set out to identify the core components required for the effector domain. We started with the 302-nt HCV IRES, since it belongs to the same Class 3 IRESs and follows the same eIF-recruitment pattern as PTV-1 IRES[130]. The structures and functions of HCV-IRES domains are well-characterized[131], and the IIIabc domain (HCV-IIIabc) alone has been validated to bind tightly to eIF3[125,132](**Figure 3.8A**). We truncated the HCV-IRES down to IIIabc domain (101 nt), which yielded a highly active taRNA in the DLR assay (**Figure 3.8B**), whose potency was then validated on endogenous PTEN mRNA in both HEK293T and MDA-MB-231 cells (**Figure 3.8C and D**).

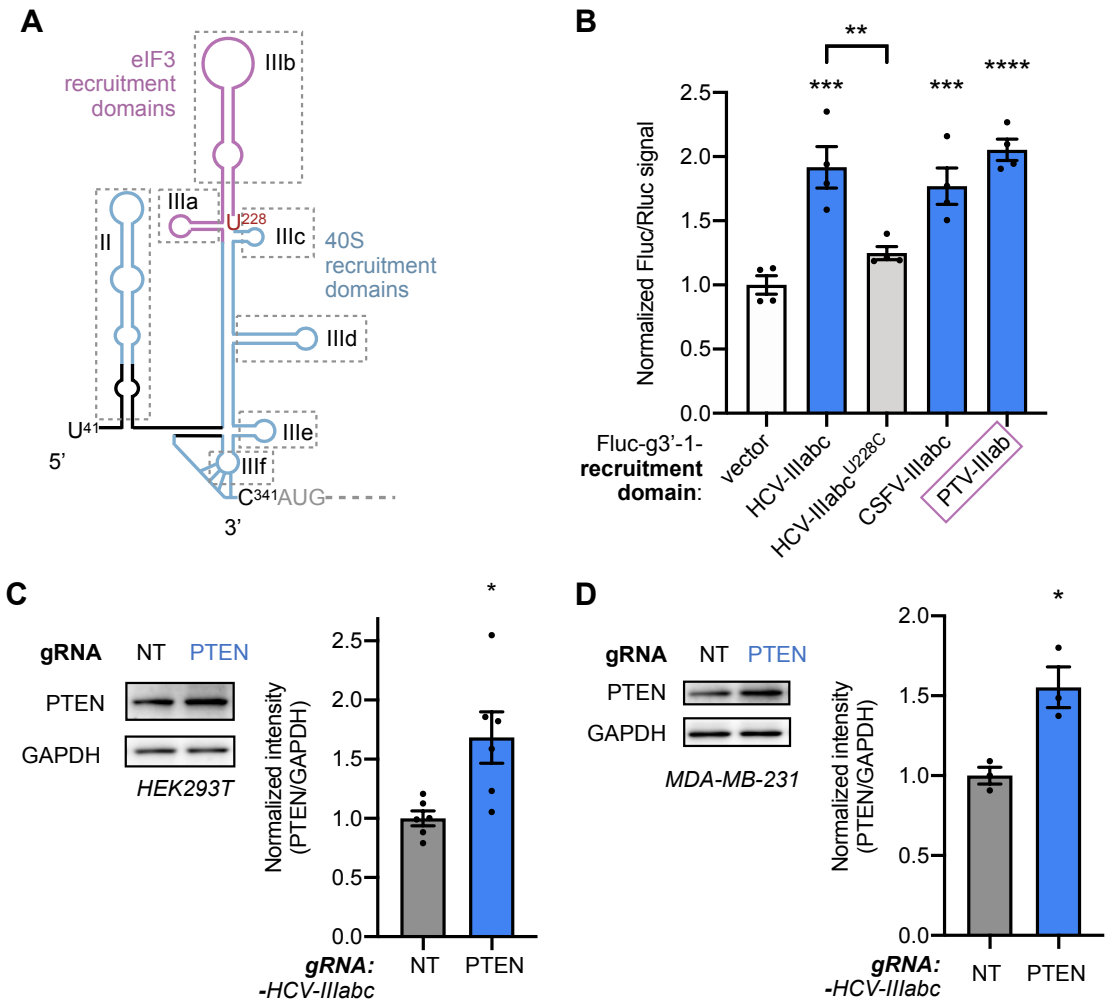

Figure 3.8 Truncated Class 3 IRESs are effective as taRNA domains in mammalian cells.

(A) Schematic of HCV IRES with annotated domains. The superscript number indicates the nucleic acid positions on the HCV genome. U228 (red) is critical for eIF3 binding. **(B)** Evaluation of truncated effector domains via DLR assay. The conserved apical domains from HCV, CSFV, and PTV-1 IRES (blue) were attached to Fluc-targeting gRNA (g3'-1). HCV-IIIabcU228C (light gray) has a single U228C inactivating mutation. Data were normalized to empty vector. n = 4 biological replicates. **(C, D)** Western blots and quantifications showing the increase of PTEN expression in HEK293T cells (C) and in MDA-MB-231 cells (D), when transfected with HCV-IIIabc based taRNA plasmid for PTEN, compared to non-targeting (NT) control. GAPDH was the loading control. n = 6 biological replicates in (C), and n = 3 biological replicates in (D). Statistical analysis was performed using one-way ANOVA followed by Sidak's multiple comparisons test between all the other groups vs. vector control, and HCV-IIIabc vs HCV-IIIabc^{U228C} in (B). Student's t test was performed in (C, D).

Based on the function of HCV-IIIabc, we postulated that eIF3 recruitment is a key mechanism utilized by Class 3 IRES-based taRNAs. To test this hypothesis, we introduced a single mutation (U228C), known to reduce eIF3 binding affinity to HCV IRES, into the HCV-IIIabc taRNA (**Figure 3.8A**)[125], which indeed diminished taRNA activity, indicating eIF3 is a key target (**Figure 3.8B**). Since Class 3 IRESs share a conserved structural domain for eIF3 binding, including domain IIIabc for classical swine fever (CSFV) IRES[133] and domain IIIab for PTV-1 IRES[134], we tested whether these isolated apical domains can also serve as taRNA effectors. Both CSFV-IIIabc and PTV-IIIab were indeed effective as taRNA effector domains (**Figure 3.8B**), providing a new set of small effectors for taRNA engineering.

Aside from eIF3, other eIFs may also be recruited by taRNAs to activate translation. We built a second truncated taRNA based on the J-K region of EMCV IRES (EMCV-JK), which directly binds eIF4G[135], but not eIF3[136]. This eIF4G-recruiting taRNA enhanced both reporter and endogenous target expression (**Figure 3.9A and B**), providing another small effector domain for taRNA, which functions through a different mechanism.

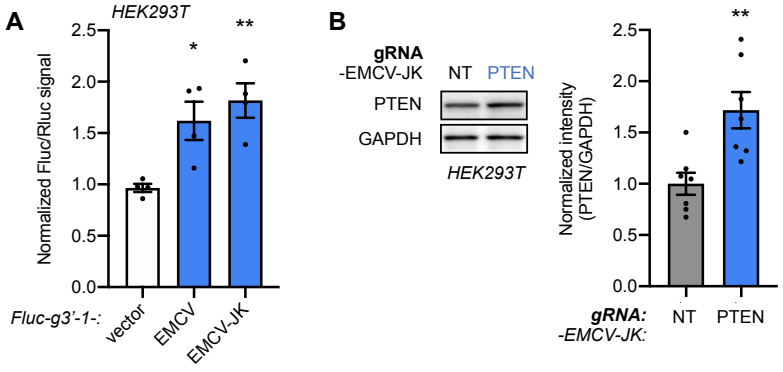

Figure 3.9 Truncated EMCV IRES serves as the effector domain in HEK293T cells. **(A)** Full EMCV IRES and its J-K region (EMCV-JK) were tested in DLR assay. n = 4 biological replicates. **(B)** Western blots and quantification showing the increase of PTEN expression from EMCV-JK-based taRNA treatment (blue), compared to non-targeting control (gray). GAPDH was the loading control. n = 7 biological replicates. Statistical analyses were performed using one-way ANOVA followed by Dunnett's multiple comparison test vs. vector in (A). Student's t test was performed in (B).

3.2.6 Small taRNAs activate disease-associated gene expression

Among the truncated effector domains tested above, the PTV-IIIab has the shortest length (**Figure 3.10A**), and offers excellent efficacy in both HEK293T cells (**Figure 3.8B**) and mouse Neuro-2a (N2a) cells (**Figure 3.10B**) in DLR assay. Thus, we advanced to further study the PTV-IIIab-based taRNA. It consists of a 40-nt gRNA, a 5-nt linker, and an 80-nt effector domain, resulting in a total length of 125 nt (**Figure 3.10C**). This PTV-IIIab-based taRNA is sensitive to gRNA-binding site mismatches, as introducing three mutations (GAG to UGU) at the center of the Fluc gRNA g3'-1 (mis-g3'-1) abolished taRNA activity in DLR assay (**Figure 3.10D**).

We confirmed the PTV-IIIab-based taRNA activity on the endogenous target, PTEN, in HEK293T cells (**Figure 3.11A**). Next, we assessed the activity of the PTV-IIIab-based taRNA to increase protein production from haploinsufficiency disease-relevant genes, including *SYNGAP1*, whose haploinsufficiency causes developmental delay, epilepsy, and autism[28]; and PMP22, whose haploinsufficiency results in Hereditary Neuropathy with Liability to Pressure Palsies (HNPP)[137]. We found the PTV-IIIab-based taRNA could upregulate the expression of both targets with two possible 3' UTR-binding gRNAs (**Figure 3.11B and C**), in NIH/3T3 and N2a mouse cells respectively. Collectively, these data demonstrate taRNAs are functional across species, and have the potential to treat haploinsufficiency-based disorders.

A

IRES domain	length	initiation factors directly recruited by domain
HCV-IIIabc	100 nt	eIF3
PTV-1-IIIab	80 nt	eIF3
CSFV-IIIabc	100 nt	eIF3
EMCV-JK	100 nt	eIF4G

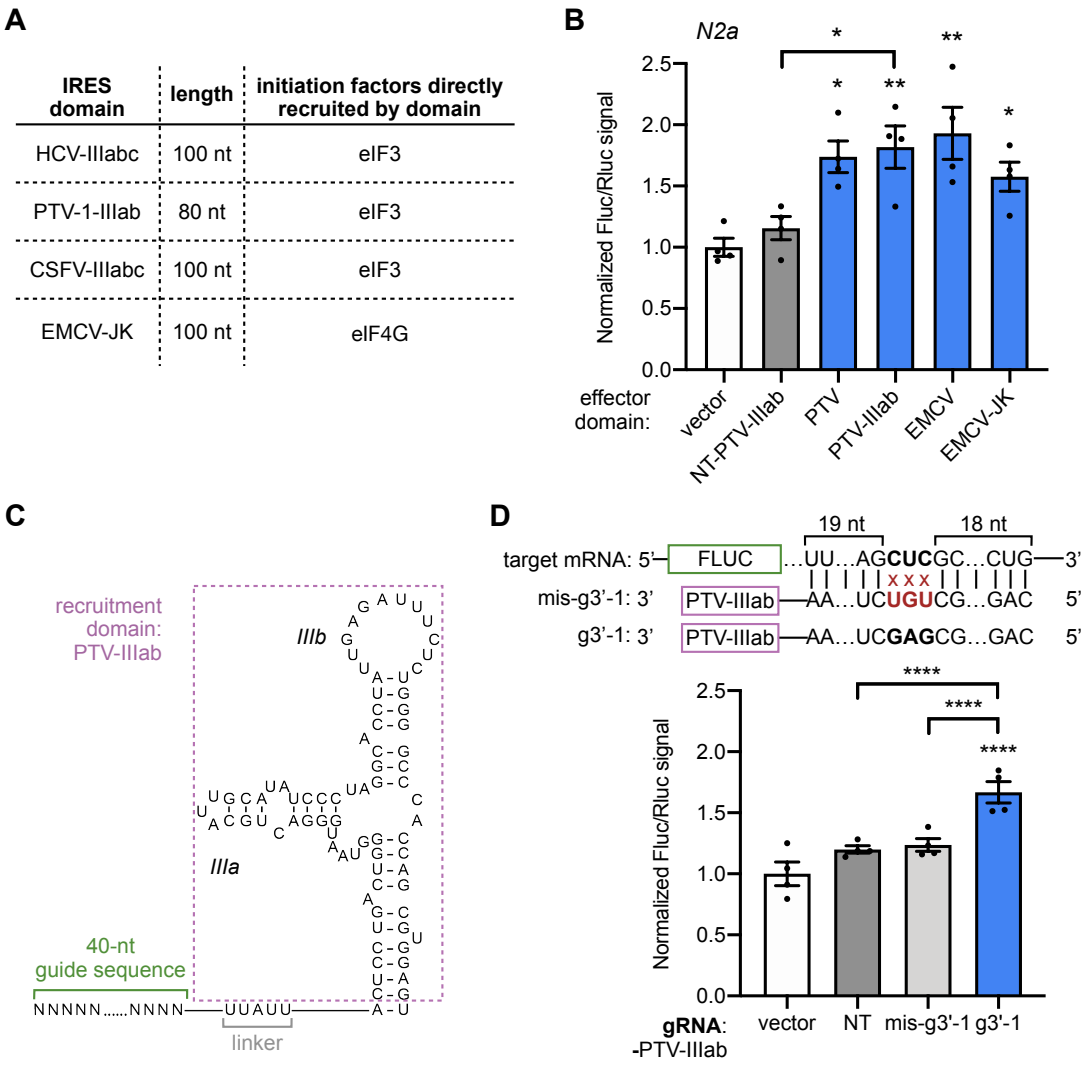

Figure 3.10 PTV-IIIab-based taRNA is selected as the leading small taRNA.
(A) The table summarizes the lengths of small effector domains and the initiation factors recruited by them. **(B)** DLR assay measured the activity of Fluc-targeting taRNAs from different recruitment domains in mouse cell line Neuro 2A (N2a). n = 4 biological replicates. **(C)** Schematic of PTV-IIIab-based taRNA, with annotated domains and nucleotide sequence. **(D)** GAG-to-UGU mutations were introduced in the middle of Fluc mRNA-targeting gRNA (g3'-1) to make mis-g3'-1, the activities of these PTV-IIIab-based taRNAs were measured by DLR assay. NT gRNAs was used as a negative control. n = 4 biological replicates. Statistical analyses were performed using one-way ANOVA followed by Sidak's multiple comparisons test in (B) and (D).

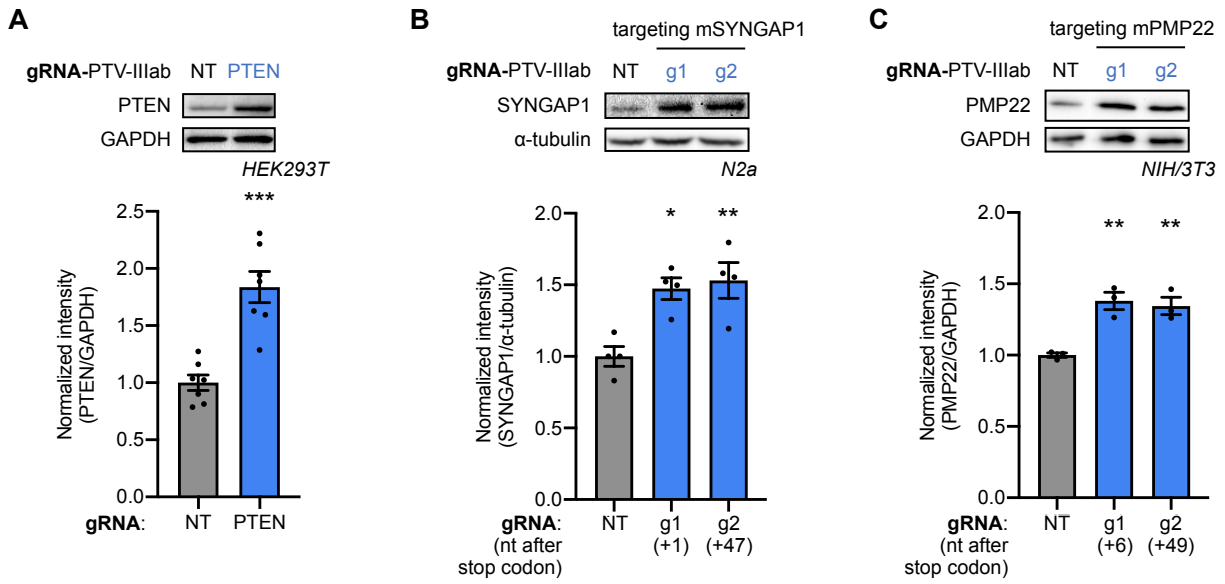

Figure 3.11 PTV-IIIab-based taRNA is selected as the leading small taRNA.
(A) The table summarizes the lengths of small effector domains and the initiation factors recruited by them. **(B)** DLR assay measured the activity of Fluc-targeting taRNAs from different recruitment domains in mouse cell line Neuro 2A (N2a). n = 4 biological replicates. **(C)** Schematic of PTV-IIIab-based taRNA, with annotated domains and nucleotide sequence. **(D)** GAG-to-UGU mutations were introduced in the middle of Fluc mRNA-targeting gRNA (g3'-1) to make mis-g3'-1, the activities of these PTV-IIIab-based taRNAs were measured by DLR assay. NT gRNAs was used as a negative control. n = 4 biological replicates. Student's t test was performed in (A). One-way ANOVA followed by Dunnett's multiple comparison test vs. NT was performed in (B) and (C).

To verify that the protein-level increase mediated by taRNA is biologically relevant, two PTV-IIIab-based taRNAs were transfected together into the triple-negative breast cancer cell line, MDA-MB-231 (**Figure 3.12A**), to simultaneously boost the expression of both PTEN and CDKN1A while the cell viabilities were monitored. The dual upregulation of both tumor suppressor genes inhibited cancer cell growth by 54% (**Figure 3.12B**). These data suggest that taRNAs are capable of activating more than one target in tandem, and that the upregulation from taRNA treatment drive meaningful phenotypic shifts in cells.

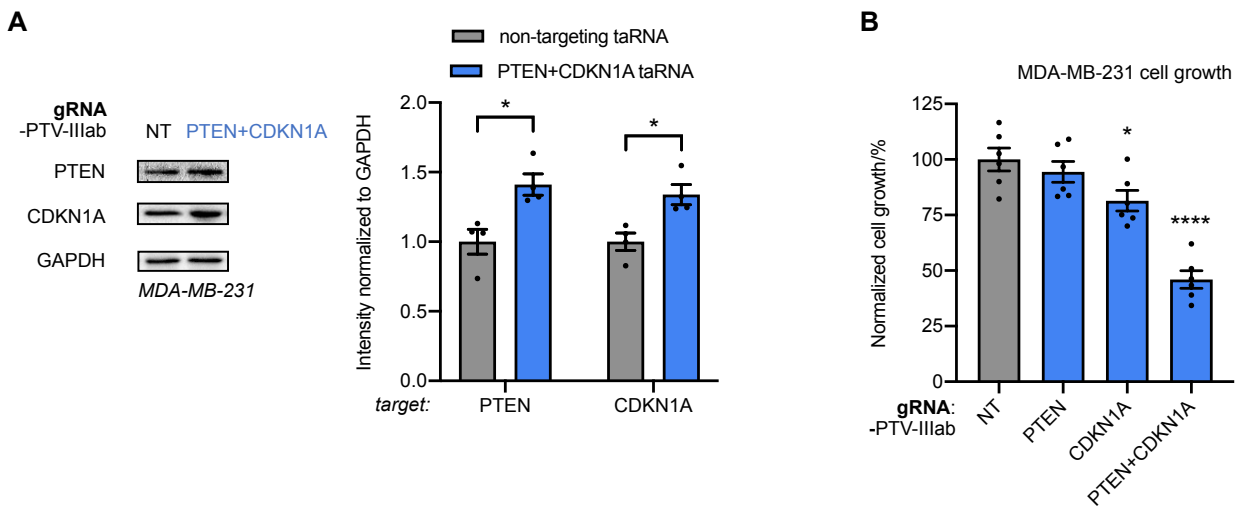

Figure 3.12 PTV-IIIab-based taRNA can be utilized to inhibit cancer cell growth. **(A)** Representative Western blots and quantification of PTEN and CDKN1A increased simultaneously by PTV-IIIab-based taRNAs in MDA-MB-231 cells. n = 4 biological replicates. **(B)** Targeted upregulation of both anti-proliferative proteins PTEN and p21 (encoded by the CDKN1A gene) by PTV-IIIab-based taRNAs simultaneously inhibits MDA-MB-231 cell growth (CCK-8 assay) by more than 50% at 72h post-plating. n = 6 biological replicates. Student's t test was performed in (A). One-way ANOVA followed by Dunnett's multiple comparison test vs. NT was performed in (B).

3.3 Conclusion and Discussion

In summary, here we present "translation-activating RNAs" (taRNAs), a bifunctional RNA-based molecular technology that binds to a specific mRNA of interest and directly upregulates its translation in mammalian cells. We construct taRNAs from a variety of viral or mammalian RNA internal ribosome entry sites (IRESs) and demonstrate gene activation on a suite of target mRNAs in several cell lines. We characterized the guide RNA domain of PTV-based taRNA as 3' UTR preferred and variable for lengths between 30 nt to 50 nt. We truncated the taRNA scaffold to 125 nucleotides, identify two translation initiation factor proteins responsible for taRNA activity, and validate the platform for haploinsufficient disease-related targets, SYNGAP1 and PMP22. The PTV-IIIab based taRNAs are also utilized to boost the translation of two targets simultaneously, and caused mean-

ingful cell function alternations. Overall, the taRNA is a potential platform as therapeutic RNA to treat diseases caused by insufficient gene expression.

The taRNA platform is versatile for a broad range of mRNA targets. Its effector domains can be customized from a collection of full-length IRESs, and IRES subdomains, suggesting that further mining of other viral and mammalian IRESs will further expand the suite of possible taRNA building blocks. The optimal guiding sequences on a target can be flexibly chosen from the 3' UTR, and potentially from 5' UTR, which, in principle, allowing the application of taRNAs on any mRNA-of-interest. This is especially important for targets whose 5' UTR and translation initiation sites offer no suitable binding sites due to their short length or complex structure[138], and targets whose 5' UTR complementary sequences also bind to critical off-targets.

More broadly, genome-wide association studies (GWAS) have revealed hundreds of novel disease-related genes. The taRNA platform, as a generalizable technology to upregulate specific genes, could accelerate both mechanistic studies and test the therapeutic potential of gene targets. For example, ABCA7 haploinsufficiency is associated with an increased risk for both early- and late-onset Alzheimer's disease (AD)[139]. However, the efficient elevation of ABCA7 expression, especially *in vivo*, is difficult, in part because its large size (6.4 kb) exceeds the packaging capacity of AAV57. Activation of ABCA7 expression levels using the taRNAs described here offers a possible strategy to both probe the therapeutic potential of ABCA7 activation in animal models of AD, as well as to provide a starting point for therapeutic development.

3.4 Material and Methods

Cloning All plasmids were cloned using Gibson Assembly and sequenced by the University of Chicago Comprehensive Cancer Center DNA Sequencing and Genotyping Facility. PCR fragments for Gibson Assembly were generated using Q5 Hot Start DNA Poly-

merase (NEB). All IRES sequences were synthesized as gBlocks by IDT. Key plasmids used in this study are listed in **Table 3.1** with links to their vector maps and are available upon request. All guide RNA sequences used in this chapter is listed in **Table 3.2**, and examples of full taRNA sequences are listed in **Table 3.3**.

Mammalian cell culture and transfection For cell culture assays, HEK293T (ATCC), HepG2 (ATCC), MDA-MB-231 (ATCC), NIH/3T3 (ATCC) and Neuro-2a cells (ATCC) were used. Cells were maintained in Dulbecco's Modified Eagle Medium (DMEM, L-glutamine, high glucose, sodium pyruvate, phenol red; Corning) supplemented with 10% fetal bovine serum (FBS; Gemini Benchmark), and 1x penicillin/streptomycin (P/S; Gibco/Life Technologies) in a humidified 37 ℃ incubator with 5% CO2. For all experiments, cells had undergone fewer than 25 passages. For transfections, cells were plated in full media without penicillin/streptomycin and transfected at 70% confluency 18-24h later. The Lipofectamine 2000 (Invitrogen) reagent was used for HEK293T cells and lipofectamine LTX (Invitrogen) with Plus reagent was used for all other cell lines, according to the manufacturer's protocols. Specifically, for endogenous targets, 500 ng taRNA plasmids were used in each well of 24-well plate and 1000 ng for 12-well plate.

Dual-luciferase reporter (DLR) assay To assess changes in protein levels, cells were co-transfected with 12 ng dual luciferase reporter plasmid, and 300 ng of the indicated taRNA expression vector. About 16 h before transfection, cells were plated on 96-well plates (Corning) and allowed to grow to 70%–80% confluency overnight. The next day, cells were transfected with the indicated plasmids by lipofectamine 2000 or LTX depending on the cell type. After 48 h of transfection, luminescence readouts of Firefly and Renilla luciferase were sequentially measured on a Biotek Synergy plate reader as previously described[117] with the following modifications. First, growth media was reduced to 80 µL for every well. Then, 40 µL of 3x firefly assay buffer (Triton Lysis Buffer (150 mM Tris, 75

mM NaCl, 3 mM $MgCl_2$, 0.25% Triton X-100) containing 15 mM DTT, 0.6 mM coenzyme A, 0.45 mM ATP, and 4.2 mg/mL D-luciferin) was added to lyse the cells and to provide the first substrate for firefly luciferase. After a 10 min incubation, the Firefly read was taken and 60 µL 3x Renilla assay buffer (45 mM EDTA, 30 mM sodium pyrophosphate, 1.4 M NaCl, 0.01 mM coelentrazine h (CTZ-h), 0.06 mM PTC124) was added to stop Firefly luciferase activity and provide the substrate for Renilla luciferase. The Renilla read was taken within 5 mins. All experiments conducted in 6 biological replicates had the highest and lowest values omitted. Firefly luciferase luminescence read were divided by the corresponding Renilla luminescence read to generate the normalized change in protein levels of the target Firefly luciferase.

Western blotting The treated cells were washed with DPBS and lysed in RIPA buffer (50 mM Tris, 150 mM NaCl, 1% Triton X-100, 0.5% sodium deoxycholate, 0.1% SDS, 1 mM EDTA, pH 7.4) supplemented with protease inhibitors and phosphatase inhibitors (Santa Cruz sc-45045). After 10 min incubation at room temperature, the lysates were centrifuged to remove debris. Total protein concentration was measured by BCA assay (Thermo Scientific). 10 µg to 35 µg total protein was boiled in protein loading buffer (50 mM Tris pH 6.8, 2% SDS, 10% glycerol, 0.05% bromophenol blue, 100 mM DTT) for 5 min at 70 90 ℃ and loaded onto 8%-12% SDS-PAGE gel according to target protein size. The total protein amount loaded was confirmed to be within linear range of detection for each antibody to detect each target protein. After stacking at 90 V, the gel was run at 140 V until the dye front reached the bottom. The proteins were transferred onto a methanol activated PVDF membrane (pore size 0.45 µm; Immobilon-P from Millipore) using semi-dry transfer apparatus (Bio-rad) or wet transfer system (Bio-rad). Membranes were blocked with 3% BSA in TBST buffer for 1h at room temperature, incubated with primary antibody in 3% BSA-TBST at 4 ℃ overnight, and then washed with TBST buffer (4x 5 mins), followed by corresponding HRP-conjugated secondary antibody incubation

1h at room temperature. The loading control GAPDH and α-tubulin were visualized using 1:2500 HRP-conjugated anti-GAPDH or anti-α-tubulin antibody. Membranes were imaged on a Fluor Chem R (Protein Simple) imager after incubation with SuperSignal West Pico PLUS chemiluminescent substrate (Thermo Scientific). For antibody dilutions and vendor information, see **Table 3.4**.

Quantification of signal intensity on Western blots All image analysis was performed with Fiji/ImageJ. The 16-bit image from chemiluminescence channel was first set to 8-bit, then processed to subtract background using a "rolling ball" algorithm. The radius was set at 50 pixels, which is at least the size of the largest band that is not part of the background, as measured in the images. The band intensity was then measured by ImageJ within the Regions of Interest (ROIs), which is set as the same dimensions for all bands across the same image. The mean intensity is then divided by the corresponding loading control intensity, as the quantified intensity for comparation.

RT-qPCR Cells were plated on 96-well plates (Corning) and transfected at 70% confluency as described above for luciferase assays. Total RNA was harvested 48 h after transfection and isolated using the RNeasy Mini Kit (QIAGEN). After isolation, RNA was reversely transcribed to cDNA using the PrimeScript RT Reagent Kit (TaKaRa). All qPCR reactions were run at 20 µL volumes with at least 3 biological replicates using FastStart Essential DNA Green Master (Roche) and amplified on a LightCycler 96 Instrument (Roche). The qPCR primers were either identified based on previous publications or verified for specificity using NCBI Primer BLAST. Expression levels were calculated using the housekeeping control gene (GAPDH) cycle threshold (C_t) value and the gene of interest C_t value. The relative expression level of one gene was determined by $2^{-\Delta C_t}$, where ΔC_t = C_t (gene of interest) - C_t (GAPDH). Relative expression level for targeted gene was obtained upon dividing the targeted gene expression level of cells experiments treated with

the on-target taRNA by those treated by the non-targeting (NT) taRNA. All qPCR primers can be found in **Table 3.5**.

Polysome profiling and RT-qPCR of fractions For polysome profiling, HEK293T cells were transfected with empty plasmids or PTEN-taRNA expressing vectors and cultured in two 15 cm dishes for 48h. Then, 200 µL of cycloheximide (10 mg/ml) was added to the media at a final concentration of 100 µg/ml and incubated in 37ºC incubator for 5 min. Cells were washed twice with ice-cold PBS containing 100 µg/ml cycloheximide, collected by scrapping, and after centrifugation (200xg for 5 min at 4ºC), the cell pellet was resuspended in 425 µL of a hypotonic lysis buffer (5 mM Tris-HCl [pH 7.5], 2.5 mM $MgCl_2$, 1.5 mM KCl, and protease inhibitor). Next, 5ul of cycloheximide (10 mg/ml), 1 µl of 1 M dithiothreitol (DTT), 100 units of RNase inhibitor, 25 µL of 10% Triton X-100 and 25 µL of sodium deoxycholate were added to the cell suspension and vortexed for 5 second. Lysates were centrifuged at 16,000 g for 7 min at 4ºC and supernatant OD were measured at 260 nm. 500 µL of supernatants were adjusted according to OD and centrifuged through a 10–50% (wt/vol) sucrose gradient at 36,000 rpm for 2 hr at 4℃ in an SW41Ti Rotor (Beckman Coulter). Gradients were fractionated, and optical density at 254 nm was continuously recorded by the Brandel Gradient Fractionation System (BR-188 Density Gradient Fractionation System, MD, USA). Fractions were combined for monosome-, light polysome- and heavy polysome-bound groups. RNA from each group was isolated with Trizol reagent (Invitrogen) according to the manufacturer's protocols. RT-PCR reactions were carried out as described above.

Cell growth assay MDA-MB-231 cells were plated on 24-well plate 18-24h before transfection. The control cells were transfected with 1 µg NT-PTV-IIIab taRNA plasmids, and the experimental cells were transfected with 1 µg PTEN-targeting PTV-IIIab, or 1 µg CDKN1A-targeting PTV-IIIab, or 500 ng PTEN targeting PTV-IIIab taRNA together with

500 ng CDKN1A targeting PTV-IIIab taRNA vectors, using Lipofectamine LTX with Plus reagent (Invitrogen) per well. After 24 hours of transfection, the cells were trypsinized and counted to be plated at 5 x 10^3 cells per well in 100 µL full media without antibiotics in a 96-well plate. The cell growth was determined at 72h post-replating by Cell Counting Kit-8 (CCK-8, abcam). Briefly, 10 µL CCK-8 reagent was added to each well in 96-well plate, and the plate was incubated for 1h at 37 ℃ before its absorbance was measured at 460 nm. The background without any cell was also measured in the wells filled with the 100 µL media and subtracted from each well's read. The cell viability was all normalized to NT control group.

3.5 Supplementary Information

Table 3.1 Representative mammalian expression plasmids used in this chapter.

#	Name	Stock No.	Description	Plasmid Map
1	Dual-luciferase reporter (ATTG)	47-23	PGK-ATTG-Fluc-SV40-Rluc	https://benchling.com/s/seq-ous8G6laHHS2SYCFpyxa
2	Empty vector	44-65	hU6-N/A	https://benchling.com/s/seq-VD4rAeSkTyUkjgkJCjLZ
3	Fluc g3'-1-CrPV	43-48	hU6-Fluc 3' UTR targeting gRNA-1-CrPV IRES	https://benchling.com/s/seq-kEtlcgxXm9fP3npZuCxs
4	Fluc g3'-1-HCV	42-72	hU6-Fluc 3' UTR targeting gRNA-1-HCV IRES	https://benchling.com/s/seq-z2BhpP2uZCeteXGqIiG5
5	Fluc g3'-1-PTV	39-01	hU6-Fluc 3' UTR targeting gRNA-1-PTV-1 IRES	https://benchling.com/s/seq-uBfm5RTqafo0F7mY0SQp
6	Fluc g3'-1-EMCV	42-74	hU6-Fluc 3' UTR targeting gRNA-1-EMCV IRES	https://benchling.com/s/seq-nkTvA6khZ9GPIhGlP9Tb
7	Fluc g3'-1-PV	50-50	hU6-Fluc 3' UTR targeting gRNA-1-PV IRES	https://benchling.com/s/seq-umnhNYPp9Mi74MWqBZEM
8	Fluc g3'-1-FMDV	50-51	hU6-Fluc 3' UTR targeting gRNA-1-FMDV IRES	https://benchling.com/s/seq-9xvL8e34qMYisdweZuy5
9	Fluc g3'-1-c-myc	50-52	hU6-Fluc 3' UTR targeting gRNA-1-c-myc IRES	https://benchling.com/s/seq-CeE1wlKCD5DislhLNkdL
10	PTV	44-64	hU6-PTV-1 IRES	https://benchling.com/s/seq-oMuzM3VOpdyF8hfHjWgQ
11	PTV-Fluc g3'-1	38-81	hU6-PTV-1 IRES- Fluc 3' UTR targeting gRNA-1	https://benchling.com/s/seq-xzhiX8YCAK1bLwaOwxwa
12	Fluc g3'-1-HCV-ΔII	48-28	hU6-Fluc 3' UTR targeting gRNA-1-HCV IRES without domain II	https://benchling.com/s/seq-6AjZq8bGTmjLKBPKZGiX
13	Fluc g3'-1-HCV-IIIabc	48-29	hU6-Fluc 3' UTR targeting gRNA-1-HCV IRES domain IIIabc	https://benchling.com/s/seq-qo58W1AD4phKq7Kgpuyx
14	Fluc g3'-1-HCV-IIIabc^{U228C}	50-53	hU6-Fluc 3' UTR targeting gRNA-1-HCV IRES domain IIIabc-U228C mutation	https://benchling.com/s/seq-9eHFsiOXhsN1kluNlihh
15	Fluc g3'-1-CSFV-IIIabc	50-54	hU6-Fluc 3' UTR targeting gRNA-1-CSFV IRES domain IIIabc	https://benchling.com/s/seq-SWPzsCkR0kFrLMNuWG4f
16	Fluc g3'-1-PTV-IIIab	48-37	hU6-Fluc 3' UTR targeting gRNA-1-PTV-1 IRES domain IIIab	https://benchling.com/s/seq-ybZr3sl0ZFszka3TXzKA
17	Fluc g3'-1-EMCV-JK	51-18	hU6-Fluc 3' UTR targeting gRNA-1-EMCV IRES JK region	https://benchling.com/s/seq-HhgIRgdPyHl5K2ahGB5F
18	AAV transfer plasmid for NT-PTV-IIIab	KJ854	pX601 AAV EF1a-EGFP-hU6-NT-PTV-IIIab	https://benchling.com/s/seq-Qq7YlSO3NFm9H7h0EveC?m=slm-f4OwR9vG26s0BlrxGFM0
19	AAV transfer plasmid for mPTEN-PTV-IIIab	KJ855	pX601 AAV EF1a-EGFP-hU6-mPTEN-PTV-IIIab	https://benchling.com/s/seq-bt6EvPbkH86PwmcG2C7i?m=slm-KefpZET7lxLxddfnsXLS
20	mPTEN-PTV-IIIab with hairpins	59-21	hU6-hp-mPTEN-PTVIIIab-hp	https://benchling.com/s/seq-8Q6v9VKjl5XpEmtka1EP?m=slm-f8kyWBsE44aUlYOPmia4
21	Non-targeting mini with hairpins	62-77	hU6-hp-NT (30nt)-mini-hp	https://benchling.com/s/seq-fNT3YEjcMPqZ0usoeuph?m=slm-pi9HD0pbLazKWCfwRrT7
22	Control with no recruitment domain	72-194	hU6-hp-mSYNGAP1 g4-hp	https://benchling.com/s/seq-2Tw8jxXKaCLECUkmZYvQ?m=slm-zLcpCI6drnWT1PNLqtPw

Table 3.2 Guide RNA sequences used in this chapter.

#	Target	Sequence
1	NT (non-targeting)	UGACAGCCCACAUGGCAUUCCACUUAUCACUGGCAUCCUU
2	Fluc-g5'	GGUGGCUUUACCAACAGUACCGGAUUGCCAAGCUUGGGCU
3	Fluc-gCDS-1	UCCUCCUCGAAGCGGUACAUGAGCACGACCCGAAAGCCGC
4	Fluc-gCDS-2	CUUGCUCACGAAUACGACGGUGGGCUGGCUGAUGCCCAUG
5	Fluc-gCDS-3	AUGGCGCUGGGCCCUUCUUAAUGUUUUUGGCAUCUUCCAU
6	Fluc-gCDS-4	CUGGUUCACACCCAGUGUCUUACCGGUGUCCAAGUCCACC
7	Fluc-gCDS-5	GCCGCCCUUCUUGGCCUUAAUGAGAAUCUCGCGGAUCUUG
8	Fluc-g3'-1	CAGGUCGACUCUAGACUCGAGGCUAGCGAGCUCGUUUAAA
9	Fluc-g3'-2	GCUCAGCGGUGGCAGCAGCCAACUCAGCUUCCUUUCGGGC
10	Fluc-g3'-1-50nt	CAGGUCGACUCUAGACUCGAGGCUAGCGAGCUCGUUUAAA CAACUAGAAU
11	Fluc-g3'-1-30nt	CGACUCUAGACUCGAGGCUAGCGAGCUCGU
12	Fluc-g3'-1-20nt	CUAGACUCGAGGCUAGCGAG
13	Fluc-g3'-1-15nt	CUCGAGGCUAGCGAG
14	g1(PPIB)	CCUGCACAGACGGUCACUCAAAGAAAGAUGUCCCUGUGCC
15	g2(PPIB)	GAAUGUGAGGGGAGUGGGUCCGCUCCACCAGAUGCCAGCA
16	g1(ABCA7)	AUUCCCAGGGCCUCCCCCGCGGCCCCGCAGGGGAGGGAGGC
17	g2(ABCA7)	AGCCCCUCUGCCAGCCUGAGUCCAGGGCUCCUAGGCACUC
18	g1(p21)	AGAGCGGGCCUUUGAGGCCCUCGCGCUUCCAGGACUGCAG
19	g2(p21)	GGGGGGCAGGGGGCGGCCAGGGUAUGUACAUGAGGAGGUG
20	g1(PTEN)	UCAGACUUUUGUAAUUUGUGUAUGCUGAUCUUCAUCAAAA
21	g2(PTEN)	UUAUUCAAGUUUAUUUUCAUGGUGUUUUAUCCCUCUUGAU
22	g1(mSYNGAP1)	GUAGGGUGCACAGGGAAGGAGGUCUGUGAUGCUGGGUGGG
23	g2(mSYNGAP1)	GGUGGGGUGCACAAGGAAGGAGGUCUGUGACGCUGGGUGG
24	g1(mPMP22)	CUAUGCGCGCUCAGAGCCUAGACGGACGGUGCGUCGUCGG
25	g2(mPMP22)	GUUGGUUUUGUUCUCUGGUUUCCUUCCUCCCUCCCUGUGG
26	g2(mPTEN)	CAAAACCCUGUGGAUGUAUAGGGUAAAACAAGAUUGGUCA
27	mis-Fluc-g3'	CAGGUCGACUCUAGACUCACAGCUAGCGAGCUCGUUUAAA
28	g(rSYNGAP1)	GUAGGGUGCACAGGGAAGGAGGUCUGUGAUGCUGGGUGGG

Table 3.3 Examplar RNA sequences of taRNAs used in this chapter.

#	Name	Sequence
1	gRNA-HCV	NNNNNNNNNNNNNNNNNNNNNNNNNNNNNNNNNNNNNNNNuuauu UCCCCUGUGAGGAACUACUGUCUUCACGCAGAAAGCGUCUAGCC AUGGCGUUAGUAUGAGUGUCGUGCAGCCUCCAGGCCCCCCCCUC CCGGGAGAGCCAUAGUGGUCUGCGGAACCGGUGAGUACACCGGA AUUGCCAGGACGACCGGGUCCUUUCUUGGAUCAAUCCCGCUCAA UGCCUGGAGAUUUGGGCGUGCCCCCGCGAGACUGCUAGCCGAGU AGUGUUGGGUCGCGAAAGGCCUUGUGGUACUGCCUGAUAGGGUG CUUGCGAGUGCCCCGGGAGGUCUCGUAGACCGUGCACC
2	gRNA-PTV	NNNNNNNNNNNNNNNNNNNNNNNNNNNNNNNNNNNNNNNNuuauu UACUUGGUUAUGAAUUCAUUGUAUUAACCCCUCUGAAAGACCUGC UCUGGCGCGAGCUAAAGCGCAAUUGUCACCAGGUAUUGCACCAAU GGUGGCGACAGGGUACAGAAGAGCAAGUACUCCUGACUGGGUAAU GGGACUGCAUUGCAUAUCCCUAGGCACCUAUUGAGAUUUCUCUGG GGCCCACCAGCGUGGAGU
3	gRNA-EMCV	NNNNNNNNNNNNNNNNNNNNNNNNNNNNNNNNNNNNNNNNuuauu GAGGGCCCGGAAACCUGGCCCUGUCUUCUUGACGAGCAUUCCUAG GGGUCUUUCCCCUCUCGCCAAAGGAAUGCAAGGUCUGUUGAAUGU CGUGAAGGAAGCAGUUCCUCUGGAAGCUUCUUGAAGACAAACAAC GUCUGUAGCGACCCUUUGCAGGCAGCGGAACCCCCCACCUGGCGA CAGGUGCCUCUGCGGCCAAAAGCCACGUGUAUAAGAUACACCUGC AAAGGCGGCACAACCCCAGUGCCACGUUGUGAGUUGGAUAGUUGU GGAAAGAGUCAAAUGGCUCUCCUCAAGCGUAUUCAACAAGGGGCU GAAGGAUGCCCAGAAGGUACCCCAUUGUAUGGGAUCUGAUCUGGG GCCUCGGUGCACAUGCUUUACAUGUGUUUAGUCGAGGUUAAAAAA ACGUCUAGGCCCC
4	gRNA-HCV-IIIabc	NNNNNNNNNNNNNNNNNNNNNNNNNNNNNNNNNNNNNNNNuuauu UCUGCGGAACCGGUGAGUACACCGGAAUUGCCAGGACGACCGGGU CCUUUCUUGGAUCAAUCCCGCUCAAUGCCUGGAGAUUUGGGCGUG CCCCCGCGAGA
5	gRNA-PTV-IIIab	NNNNNNNNNNNNNNNNNNNNNNNNNNNNNNNNNNNNNNNNuuauu ACUCCUGACUGGGUAAUGGGACUGCAUUGCAUAUCCCUAGGCACC UAUUGAGAUUUCUCUGGGGCCCACCAGCGUGGAGU
6	gRNA-EMCV-JK	NNNNNNNNNNNNNNNNNNNNNNNNNNNNNNNNNNNNNNNNuuauu GGGGCUGAAGGAUGCCCAGAAGGUACCCCAUUGUAUGGGAUCUGA UCUGGGGGCCUCGGUGCACAUGCUUUACAUGUGUUUAGUCGAGGU UAAAAAAACGUCUAGGCCCC

Table 3.4 Antibodies used in this chapter.

#	Target	Vendor	Catalogue Number	Dilution
1	GAPDH (HRP)	Proteintech	HRP-60004	1:5000
2	α-Tubulin (HRP)	Proteintech	HRP-66031	1:5000
3	ABCA7	Proteintech	25339-1-AP	1:1000
4	PTEN	Santa Cruz Biotechnology	sc-7974	1:1000
5	PMP22	Santa Cruz Biotechnology	sc-515199	1:1000
6	PPIB	Santa Cruz Biotechnology	sc-130626	1:1000
7	CDKN1A	Santa Cruz Biotechnology	sc-6246	1:1000
8	SYNGAP1	Invitrogen	PA1-046	1:1000
9	Phospho-p44/42 MAPK (Erk1/2)	Cell Signaling Technology	4370T	1:2000
10	p44/42 MAPK (Erk1/2)	Cell Signaling Technology	4695	1:2000
11	mouse IgG H&L (HRP)	Abcam	ab6728	1:5000
12	rabbit IgG H&L (HRP)	Abcam	ab6721	1:5000

Table 3.5 RT primers in this chapter.

#	Name	Sequence
1	Fluc-qPCR-for	GGATGCTCTCCAGTTCGGCT
2	Fluc-qPCR-rev	ACCAGCGCGGCGAGCTGT
3	Rluc-qPCR-for	CTATTGTCGAGGGAGCTAAGAAG
4	Rluc-qPCR-rev	GCTCTTGATGTACTTACCCATTTC
5	GAPDH-qPCR-for	GTCTCCTCTGACTTCAACAGCG
6	GAPDH-qPCR-rev	ACCACCCTGTTGCTGTAGCCAA
7	PPIB-qPCR-for	AACGCAGGCAAAGACACCAACG
8	PPIB-qPCR-rev	TCTGTCTTGGTGCTCTCCACCT
9	PTEN-qPCR-for	TGAGTTCCCTCAGCCGTTACCT
10	PTEN-qPCR-rev	GAGGTTTCCTCTGGTCCTGGTA
11	ABCA7-qPCR-for	CACTCTTCCGAGAGCTAGACAC
12	ABCA7-qPCR-rev	CTCCATATCTGTGTCCGCAGCA
13	CDKN1A-qPCR-for	AGGTGGACCTGGAGACTCTCAG
14	CDKN1A-qPCR-rev	TCCTCTTGGAGAAGATCAGCCG

CHAPTER 4

RNA-BASED TRANSLATION ACTIVATOR OPTIMIZED FOR NEURONAL GENE-HAPLOINSUFFICIENCY DISEASE

4.1 Introduction

Nucleic-acid-based technologies require adequate chemical modifications to stabilize them from degradation by ribonucleases. In **Chapter 3**, we have engineered an effective translation activating RNA, PTV-IIIab-based taRNA, as small as 125 nt. However, to fully exploit the chemical modifications, the ideal length of taRNA should be less than 100 nt to achieve sufficient yield by oligonucleotide synthesis[140]. At the same time, the taRNA platform will also benefit from improved efficacy, for future *in vivo* and preclinical applications. As shown in **Figure 3.11B**, the PTV-IIIab-based taRNAs effectively upregulate SYNGAP1 expression in N2a cells, therefore we used SYNGAP1 as a testbed to further engineer PTV-IIIab-based taRNA.

SYNGAP1 haploinsufficient diseases are critical unmet medical needs. This gene encodes a protein that localizes to synapses in excitatory neurons, and functions as a Ras/Rap GTPase activating protein (GAP) to attenuate Ras or Rap activity[141]. Heterozygous mutations in *SYNGAP1*, either loss-of-function mutations or premature truncation codons (PTC), are associated with a spectrum of neurodevelopmental disorders (NDDs), including autism and non-syndromic intellectual disability[28]. *SYNGAP1* is the fourth most prevalent gene associated with NDD with concomitant epilepsy, affecting 4/10,000 individuals and accounting for 0.5–1.0% of all NDD cases[80,142]. Although there are no available treatments for NDDs associated with *SYNGAP1* haploinsufficiency, re-expression of SYNGAP1 protein in adult heterozygous knockout mice relieved seizure burden[143], supporting the therapeutics that activate SYNGAP1 expression will be beneficial for patients.

In this chapter, we explore the options for taRNA delivery, including DNA vectors

encoding taRNA packaged in AAV, and *in vitro* transcribed taRNA molecules packaged in LNP. We further engineered PTV-IIIab-based taRNA into an optimized and minimized taRNA, called "mini taRNA", whose core length is only 94 nt, offering improved efficacy in both *in vitro* and *in vivo*. Importantly, we validated the therapeutic potential of taRNAs by rescuing the expression of SYNGAP1 protein in iPSC-neurons generated from a *SYNGAP1*-haploinsufficient patient. Collectively, this improved version of translation-activating RNA, mini taRNA, further demonstrates the therapeutic potential of the taRNA platform.

4.2 Results

4.2.1 taRNA platform is compatible with AAV delivery in vitro

All experiments in **Chapter 3** used plasmids to express taRNAs in transfected cells. However, the delivery of nucleic acid-based technologies for therapy in patients requires alternate strategies, most often adenovirus-associated virus (AAV) or LNPs. We designed mouse PTEN-targeting PTV-IIIab-based taRNAs as a model to compare the delivery options. First, PTV-IIIab-based taRNAs were tested for packaging and delivery by AAV (**Figure 4.1A**). We detected upregulation of PTEN expression in NIH/3T3 cells treated with PTEN-targeting, AAV1-packaged taRNAs (**Figure 4.1B and C**), thus proving the compatibility with AAV delivery system.

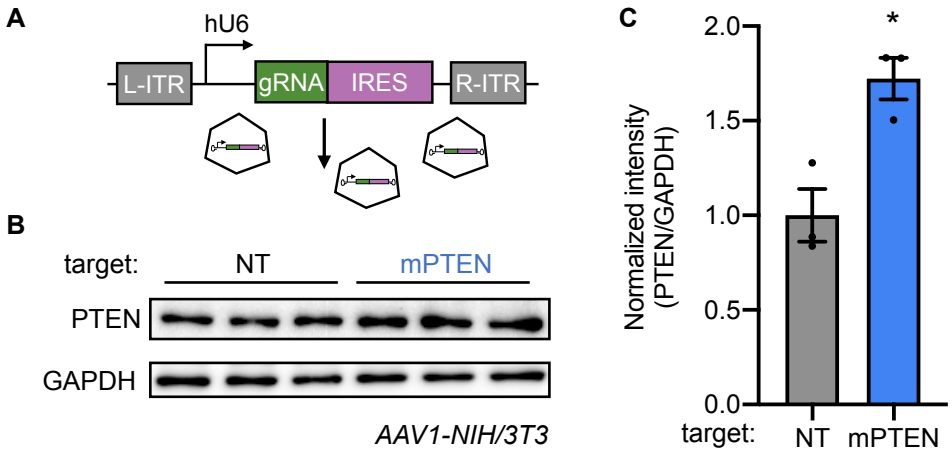

Figure 4.1 taRNA is deliverable by AAV *in vitro*.
(A) Schematic of the transfer plasmid encoding taRNA for AAV packaging. **(B)** Western blots (left) and quantification (right) measuring the increase of mouse PTEN protein amount in NIH/3T3 cells, after transduced for 48h by mPTEN-targeting PTV-IIIab-based taRNA packaged in AAV1. GAPDH is used as loading control and non-targeting PTV-IIIab-based taRNA (NT) in AAV1 is used as negative control. **(C)** Quantifications of (B). Data were normalized to the NT control. n = 3 biological replicates. Bar graph is shown as mean ± SEM with individual data points. Statistical analysis was performed using Student's t test. $^{*}P < 0.05$, $^{**}P < 0.01$, $^{***}P<0.001$, $^{****}P<0.0001$. No asterisk means not significant.

4.2.2 Stabilized taRNA is compatible with LNP delivery in vitro and in vivo

While AAV delivery is important, a strength of the oligo-based taRNA design is the ability to sidestep virus-based delivery systems. To explore non-viral delivery, we turned our attention to delivering *in vitro* transcribed taRNAs packaged in clinically viable LNPs. To protect taRNAs from exonuclease activity, we added stabilizing hairpins to both ends of the taRNA scaffold[144] (**Figure 4.2A**). This hairpin-containing PTV-IIIab-based taRNA was confirmed to be effective when transfected as a DNA vector into N2a cells targeting mouse PTEN, before further development (**Figure 4.2B**).

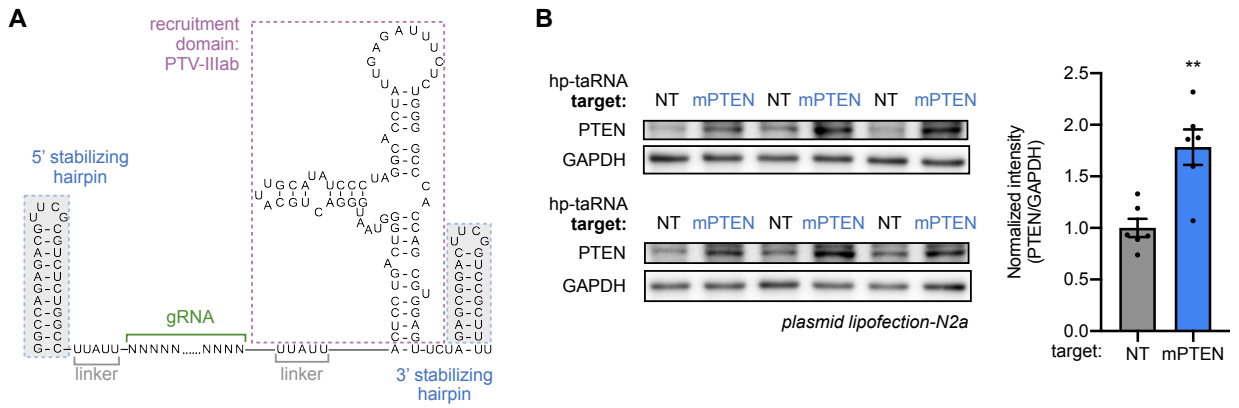

Figure 4.2 taRNA with stabilized hairpins at both ends.
(A) Nucleotide sequence and secondary structure of the PTV-IIIab-based taRNA with stabilizing hairpins added at both 5' and 3' ends. **(B)** Western blots (left) and quantification (right) measuring the increase of mouse PTEN protein in N2a cells, after lipofected for 48h by mPTEN-targeting taRNA stabilized with hairpins at both ends as (A). GAPDH is the loading control and non-targeting taRNA (NT) is the negative control. n = 6 biological replicates. Statistical analysis was performed using Student's t test.

Next, we transcribed the hairpin-PTV-IIIab-based taRNA *in vitro*, encapsulated it in LNPs, and characterized the encapsulation efficiency and LNP diameter (**Figure 4.3A**). These LNPs containing non-targeting (NT) or mouse PTEN targeting (mPTEN) taRNAs were then delivered to N2a cells. During prescreening, we found the optimal dose of mPTEN-targeting taRNA as 500ng (**Figure 4.3B**). This dose of LNP-packaged taRNAs increased PTEN protein levels at 12h post-delivery (**Figure 4.3C and D**). This activation was almost gone by 24h (**Figure 4.3E and F**), indicating that taRNA molecules delivered by LNPs activate target protein production in a transient manner.

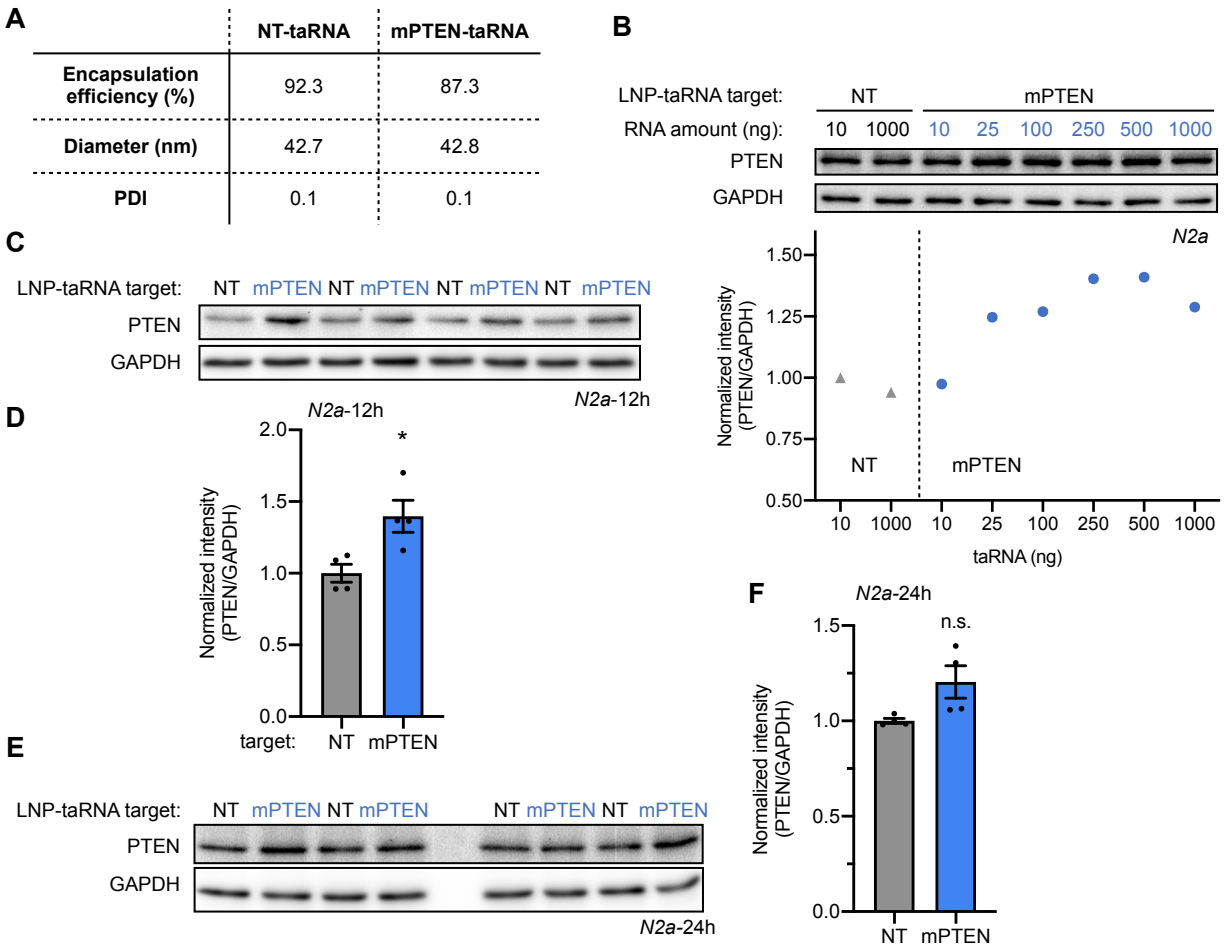

Figure 4.3 LNP-packaged taRNAs activate mouse PTEN expression *in vitro*.
(A) The characterization of LNPs made with NT or mPTEN-targeting taRNAs (PTV-IIIab-based). The encapsulation efficiency was measured by Ribogreen assay, and Dynamic light scattering (DLS) was used to measure diameter and Polydispersity Index (PDI). **(B)** Two doses of NT-taRNA control (gray triangles) and 6 different doses for mPTEN-targeting taRNAs (blue dots) in LNPs were delivered to N2a cells in 12-well plate for 12h before PTEN level was analyzed by western blotting. GAPDH was the loading control, and all value was normalized to that of 10ng NT-taRNA. **(C)** NT or mPTEN-targeting taRNA in LNPs (500 ng) were delivered to N2a cells. After 12h, the cells were lysed and PTEN protein levels measured via western blotting. **(D)** Quantification of **(C)**. Data were normalized to NT control. n=4 biological replicates. **(E)** Western blots showing PTEN protein level measured at 24h post-delivery of NT-taRNA or mPTEN-targeting taRNA by LNPs, in N2a cells. **(F)** Quantification of (E). Data were normalized to NT control. n=4 biological replicates. Statistical analysis was performed using Student's t test.

Moving forward from *in vitro* tests, we delivered the aforementioned LNP-packaged mPTEN-targeting taRNAs to live mice (0.5 mg / kg) by intravenous (i.v.) tail injection to target the liver (**Figure 4.4A**). At 12 h after injection, we resected the liver to analyze protein level and observed an increase of the target PTEN protein by Western blotting (**Figure 4.4B and C**). This result proved that taRNA are effective *in vivo* and can be deployed by LNPs.

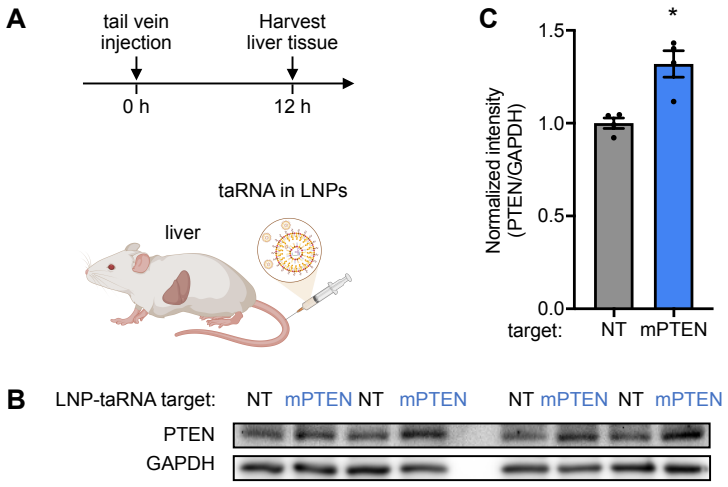

Figure 4.4 LNP-packaged taRNAs activate mouse PTEN expression *in-vivo*.
(A) Illustration of how LNP delivered taRNAs to mouse liver and the time line of experiments. **(B)** Western blots of PTEN from mouse livers harvested as (A). GAPDH is the loading control. **(C)** Quantification of (B). Data were normalized to the NT control. n = 4 biological replicates. Statistical analysis was performed using Student's t test.

4.2.3 LNPs packaged PTV-IIIab taRNAs increase SYNGAP1 expression in mouse cell lines and primary rat neurons

To explore the therapeutic potential of the taRNA platform, we used SYNGAP1 as a testbed, which can be activated by PTV-IIIab-based taRNA (g1 in **Figure 3.11B**). We *in vitro* transcribed the mouse SYNGAP1-targeting stabilized taRNA, encapsulated it in LNPs and characterized the encapsulation (**Figure 4.5A**). The optimal dose of LNP-taRNA for mouse SYNGAP1 upregualtion in N2a cells is also 500ng (**Figure 4.5B**). The

taRNA delivered to N2a cells by LNPs at optimal dose increased SYNGAP1 protein level at 12h post-delivery, and reduced the steady-state phosphorylation level of ERK 1/2, a known downstream signaling target deactivated by SYNGAP1[145] (**Figure 4.5C and D**). This transient effect also started to fade at 24h post-delivery (**Figure 4.5E and F**).

Since SYNGAP1 is widely expressed in excitatory neurons, it is important for taRNA to be functional in neurons to treat *SYNGAP1*-haploinsufficient disorder. We went on to test if taRNAs are deliverable by LNPs and active in primary cortex neurons, which are isolated from rat brains by our collaborators, Dr. Anitha P. Govind and Dr. Okunola Jeyifous, from Prof. William Green's lab. We confirmed that primary rat neurons were amendable to LNP delivery by GFP mRNA (**Figure 4.6A**), and then used the same gRNA for mouse SYNGAP1 (g1) to activate rat SYNGAP1, since the binding sequence is present in the 3' UTR of both species (**Figure 4.6B**). At 12h after LNP-delivery, the taRNA successfully amplified SYNGAP1 expression in rat neurons and reduced steady-state ERK1/2 phosphorylation (**Figure 4.6C and D**), demonstrating the efficacy of the taRNA in primary cells and the potential to treat neuronal haploinsuffiency diseases.

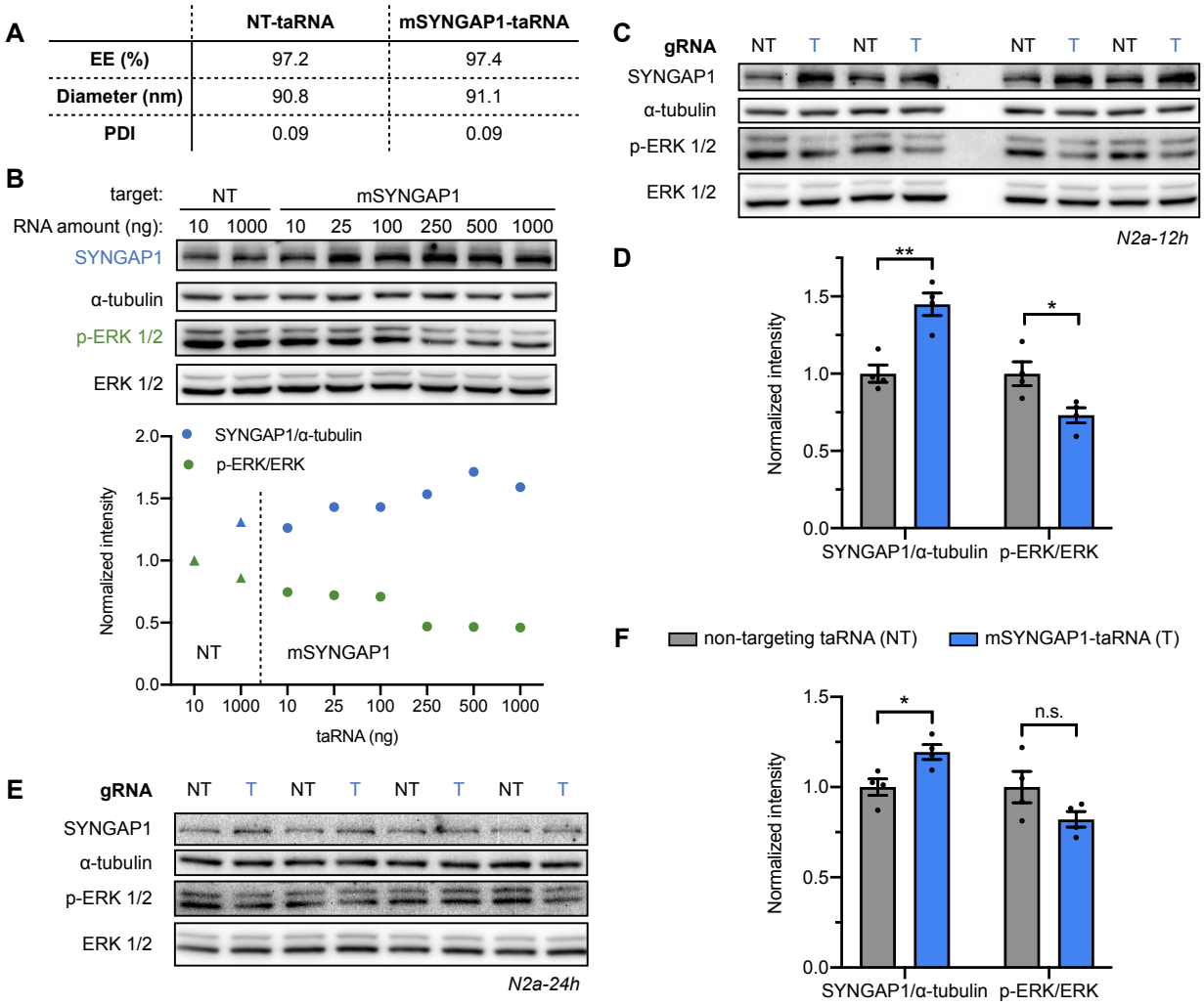

Figure 4.5 LNP-packaged taRNAs activate SYNGAP1 expression in N2a cells.
(A) Characterization of LNPs packaged NT or mouse SYNGAP1-targeting taRNAs (PTV-IIIab-based). The encapsulation efficiency (EE) was measured by Ribogreen assay. Diameter and PDI were measured by Dynamic light scattering. **(B)** Two doses of NT-taRNA control (triangles) and 6 different doses for mSYNGAP1-targeting taRNAs (dots) were delivered via LNPs to N2a cells on 12-well plates. After 12h, SYNGAP1 (blue) and phosphorylated ERK 1/2 (p-ERK 1/2, green) level were measured by Western blotting (upper panel). Quantification (lower panel) used α-tubulin and total ERK 1/2 as loading control respectively. All intensities were normalized to that of 10ng-NT. **(C)** LNP-packaged taRNAs with mouse SYNGAP1 gRNA (T) or non-targeting gRNA (NT) were delivered to N2a cells. Levels of SYNGAP1 protein and phosphorylated ERK 1/2 were evaluated at 12h post-delivery. **(D)** Quantification of (C) with α-tubulin and total ERK 1/2 as loading control respectively. Data were normalized to NT control. n = 4 biological replicates. **(E)** Western blots of the same experiment as in (C) except N2a cells were treated longer, for 24h. **(F)** Quantification of (E). Data were normalized to NT control. n = 4 biological replicates. Statistical analysis was performed using Student's t test.

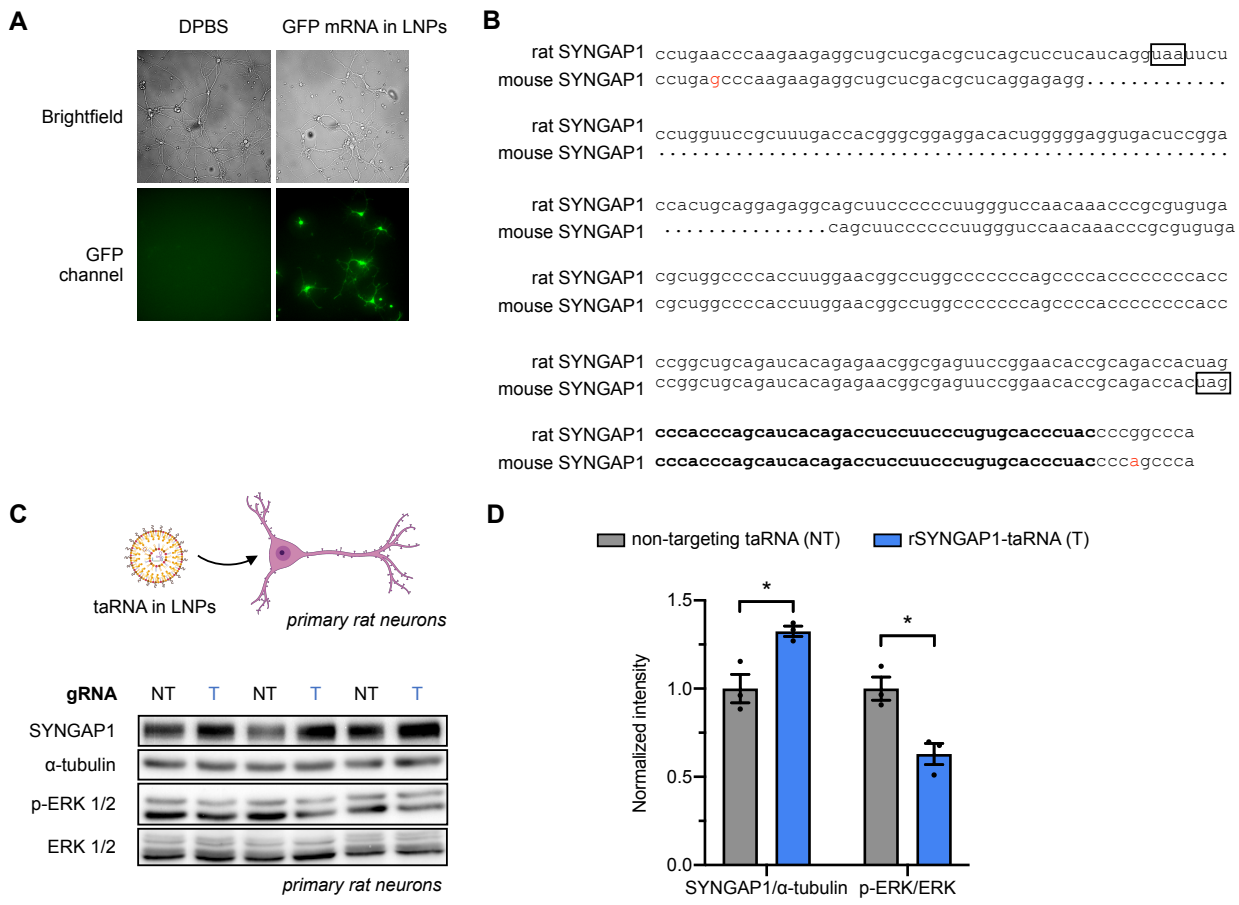

Figure 4.6 LNP-packaged taRNAs activate SYNGAP1 expression in primary neurons from rat cortex.

(A) Representative images of primary rat cortical neurons in brightfield and GFP channel, which were treated with either DPBS control or GFP-mRNA encapsulated in LNPs at day 14. Images were captured and processed using the same settings between DPBS and GFP-treated groups. **(B)** Alignment of partial sequences from rat and mouse SYNGAP1 mRNA. The mismatches are colored in red and missing nucleotides are represented with dots. The stop codon of each transcript is boxed, and the nucleotides recognized by mSYNGAP1 targeting gRNA (g1) is in bold. **(C)** LNP-packaged taRNAs with rat SYNGAP1 gRNA (T) or non-targeting gRNA (NT) were delivered to primary rat neurons. Levels of SYNGAP1 protein and phosphorylated ERK 1/2 were evaluated by Western blotting at 12h post-delivery. **(D)** Quantification of (C) with α-tubulin and total ERK 1/2 as loading control respectively. Data were normalized to NT control. n = 3 biological replicates. Statistical analysis was performed using Student's t test.

4.2.4 Guide RNA optimization for more potent taRNA

Although the PTV-IIIab-based taRNA effectively increases the SYNGAP1 protein by LNP delivery in rat neurons, the efficacy is still not satisfactory. SYNGAP1 expression should increase approximately 100% to address the haploinsufficient condition. Therefore, we sought to optimize the efficacy of PTV-IIIab-based taRNA, starting from the guide domain. In the initial experiment (**Figure 3.11B**), we only tested two gRNAs for SYNGAP1, which may not be optimal for taRNA efficacy. From there, we designed three additional gRNAs on SYNGAP1 3' UTR (**Figure 4.7A**) based on accessibility predictions (see Methods and Materials) and tested them via vectors lipofected into N2a cells. This additional screening revealed that guide 4 (g4) improved the performance of PTV-IIIab-based taRNA, compared to the original guide 1 (g1) (**Figure 4.7B and C**).

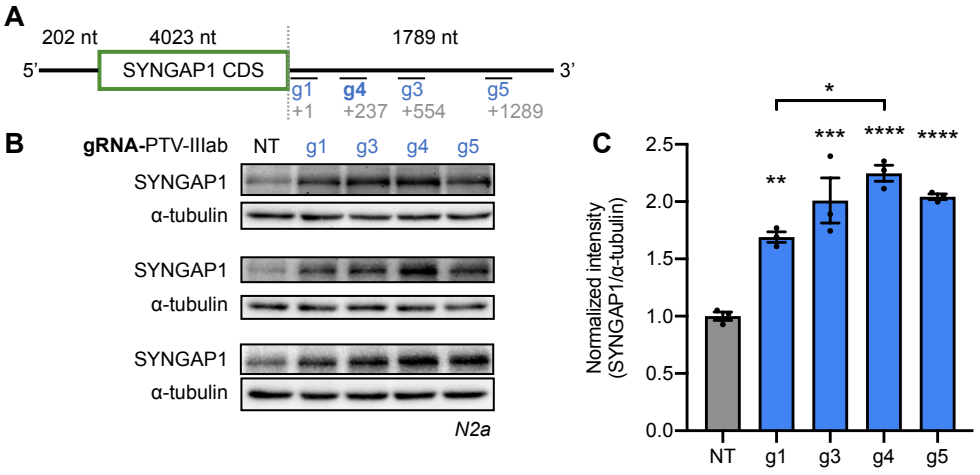

Figure 4.7 Additional screening reveals more potent guide RNAs on SYNGAP1.
(A) The positions of gRNAs (g1, g3, g4, g5) binding sites on mouse SYNGAP1 transcript is indicated by the distance between stop codon and the first nucleic acid of the gRNA (gray). The lengths of 5' UTR, CDS and 3' UTR of mouse SYNGAP1 mRNA are labeled. **(B)** Western blots measuring mouse SYNGAP1 protein levels are shown, with α-tubulin as the loading control. N2a cells were transfected using vectors for PTV-IIIab-based taRNAs with non-targeting (NT) or different gRNAs for mSYNGAP1. **(C)** Quantification of (B). Data were normalized to NT control. n = 3 biological replicates. Statistical analysis was performed using one-way ANOVA with Sidak's multiple comparisons test between all the other groups vs. NT control, and between g1 and g4.

4.2.5 Truncating the effector domain to the mini taRNA

To allow efficient oligonucleotide synthesis of taRNA molecules in the future, the scaffold of taRNA, which consists of the guide RNA domain and the effector domain, needs to be less than 100 nt. We set out to minimize the taRNA scaffold to facilitate manufacture and delivery. We shortened the guide sequence to 30 nt, which we previously found did not impact activity (**Figure 3.5C**), and removed the "linker" sequence entirely. Some extra nucleotides in the lowest stem of the PTV-IIIab domain do not interact with the 48S complex (including eIF3)[134], therefore they were also removed from the effector domain. Combined, these changes generated a 'mini-taRNA' scaffold that is only 94 nt long, excluding the additional hairpins at both ends (**Figure 4.8**).

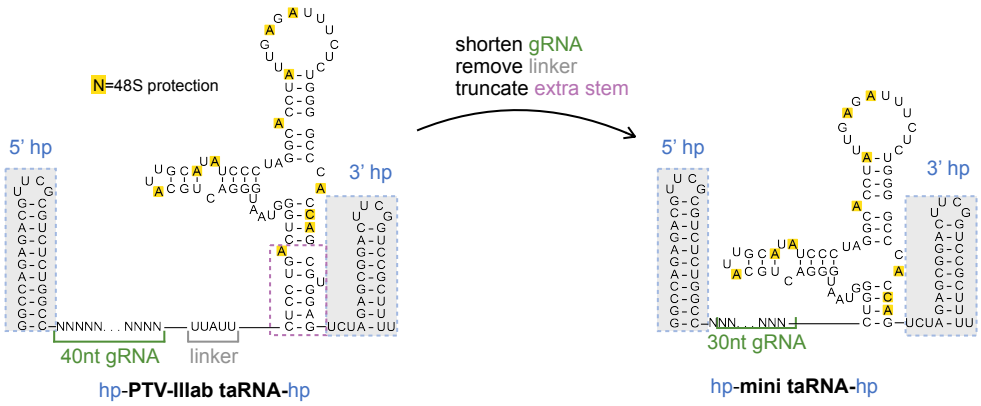

Figure 4.8 Further truncation on PTV-IIIab-based taRNA for a mini taRNA.
Schematic illustrating the engineering of the PTV-IIIab-based taRNA to a minimized taRNA ('mini taRNA'). The detachable stabilizing hairpins at both ends (5' hp and 3' hp), which are not part of the taRNA scaffold, are shadowed in gray. Nucleic acids with the yellow background were known to be protected upon 48S complex binding[134].

The mini taRNA maintained its efficacy in activating mouse SYNGAP1 expression, compared to optimal g4-PTV-IIIab taRNA in N2a cells by plasmid transfection (**Figure 4.9A and B**). Based on this mini taRNA, we made a vector expressing the effective guide RNA (g4) alone, without any effector domain attached, as a negative control. This g4 vector cannot increase mouse SYNGAP1 expression compared to non-targeting mini taRNA,

while the g4-mini taRNA can, confirming that the mini effector domain is indispensable for taRNA function (**Figure 4.9C and D**).

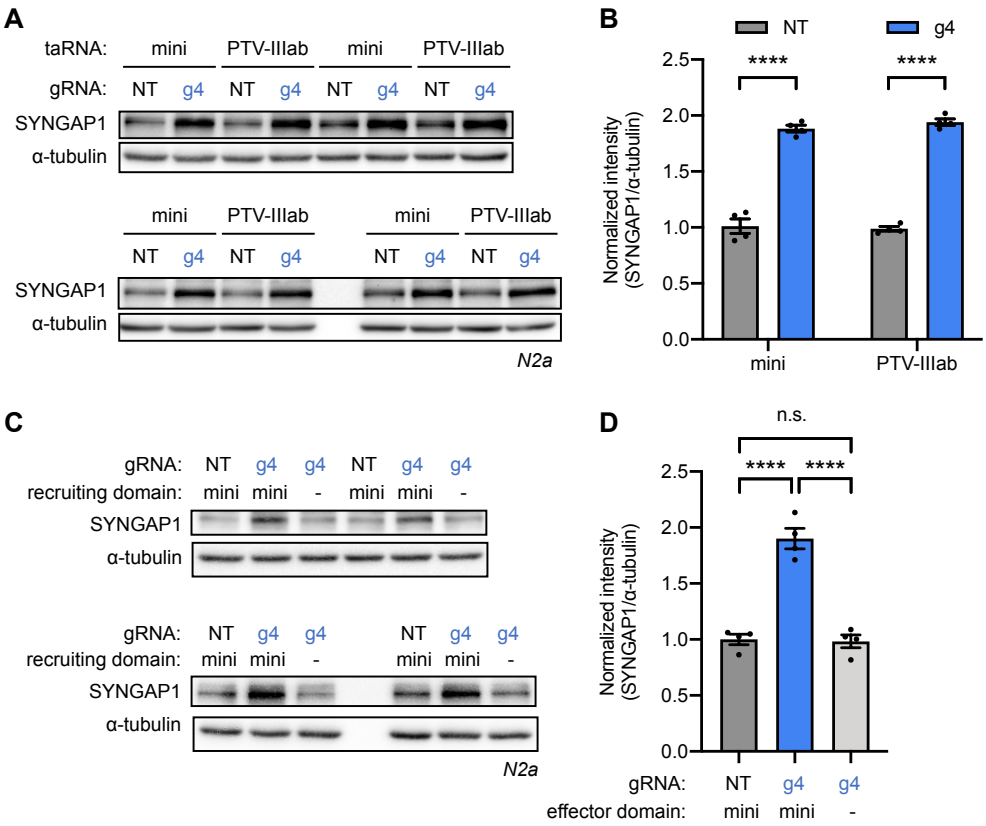

Figure 4.9 Characterization of mini taRNA for mouse SYNGAP1 upregulation. **(A)** Mini- or PTV-IIIab-based taRNAs with NT or g4 were transfected into N2a cells as plasmids, and mouse SYNGAP1 upregulation levels were compared via Western blotting. g4 is the optimized guide RNA from **Figure 4.7**. **(B)** Quantification of (A). Data were normalized to the average intensity of NT-mini and NT-PTV-IIIab controls. n = 4 biological replicates. Statistical analysis was performed using one-way ANOVA with Sidak's multiple comparisons vs. NT control in each group. **(C)** Western blots measuring mouse SYNGAP1 level in N2a cells transfected with vectors for non-targeting mini taRNA, g4-mini taRNA or g4 alone. The α-tubulin is the loading control. **(D)** Quantification of (C). Data were normalized to NT-mini taRNA. n = 4 biological replicates. Statistical analysis was performed using one-way ANOVA followed by Tukey's multiple comparisons.

4.2.6 Mini taRNA increases mouse PTEN expression in vitro and in vivo

As additional validation of mini taRNA effectiveness, we screened more gRNAs targeting mouse PTEN 3' UTR on mini taRNA, and identified two more qualified gRNAs, g4 and g5 (**Figure 4.10A**). The g4-mini taRNA targeting mouse PTEN is then *in vitro* transcribed, packaged into LNPs, and delivered to the mouse liver as described in **Figure 4.7**. It effectively activated PTEN expression compared to NT-mini taRNA and to DPBS control (**Figure 4.10B**), confirming the efficacy of mini taRNA *in vivo*.

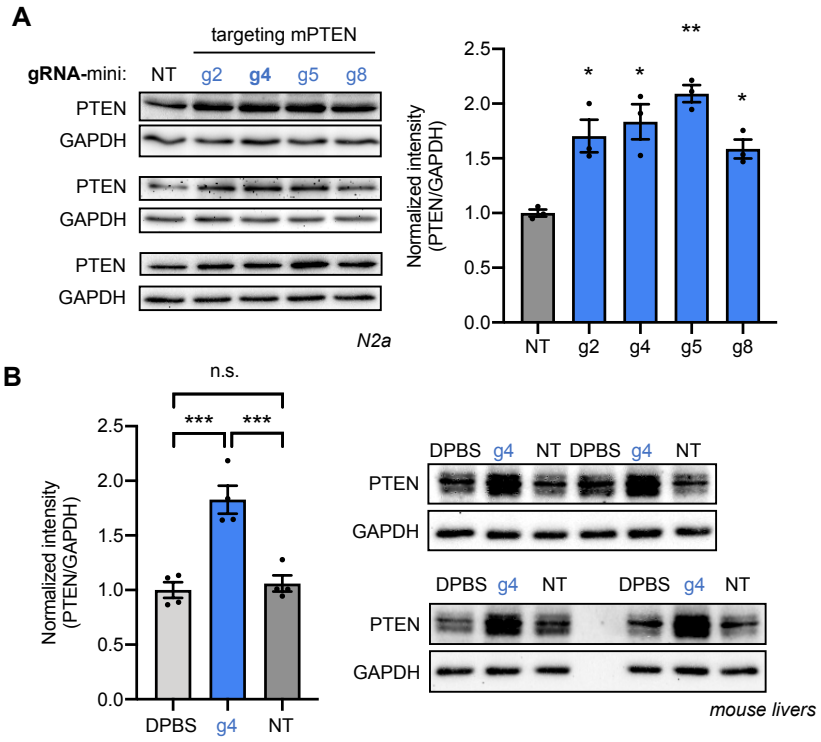

Figure 4.10 Optimized mini taRNA for mouse PTEN *in vitro* and *in vivo*.
(A) Western blots measured mouse PTEN protein in N2a cells, transfected with non-targeting mini taRNAs or with different gRNAs for mPTEN (g2, g4, g5, g8). GAPDH is the loading control. Quantification were normalized to NT-mini. n = 3 biological replicates. **(B)** The non-targeting (NT) or mouse PTEN-targeting (g4) mini taRNAs were packaged into LNPs and delivered to the mouse liver as described in **Figure 4.4A**, and DPBS buffer was injected as empty control. Western blots measuring mouse PTEN protein level from livers are shown with GAPDH as the loading control. Quantification was normalized to DPBS control. n = 4 biological replicates. Statistical analyses were performed using one-way ANOVA followed by Dunnett's multiple comparisons test vs. NT in (A); and by Tukey's multiple comparisons in (B).

4.2.7 Application of mini taRNA to address SYNGAP1-haploinsufficiency in patient cells

Finally, to apply mini taRNA in a disease-relevant cell model, we collaborated with Prof. Alfred L. George and Prof. Jimmy. L. Holder, who generated iPSC-derived cortical neurons from an individual carrying a heterozygous premature stop mutation on *SYNGAP1* (c.3190C>T, p.Q1064X). These haploinsufficient iPSC-neurons were validated to have 50% intensity decrease of SYNGAP1 detected by Western blotting, consistent with the theoretical protein level decrease; and a 25% increase in steady-state ERK1/2 phosphorylation level (**Figure 4.11A**). We identified a gRNA for human SYNGAP1 (T in **Figure 4.11**), which is effective with the mini or PTV-IIIab effector domain as taRNA, in HEK293T cells via plasmid expression (**Figure 4.11B**). This human SYNGAP1-targeting mini taRNA is then *in vitro* transcribed as hairpin-stabilized taRNA and delivered to *SYNGAP1*$^{+/-}$ iPSC-neurons by LNPs. This LNP-packaged mini taRNA successfully increased the amount of SYNGAP1 protein, to a comparable level as in wild-type iPSC-neurons (**Figure 4.11C**). As a downstream signaling readout, we found that taRNA treatment reduced steady-state phosphorylation of ERK1/2 (**Figure 4.11C**), which was over-activated in *SYNGAP1* haploinsufficient iPSC-neurons (**Figure 4.11A**). In conclusion, the mini taRNA system is shown to effectively activate the expression of the target relevant to haploinsufficiency disease in patient-derived neurons.

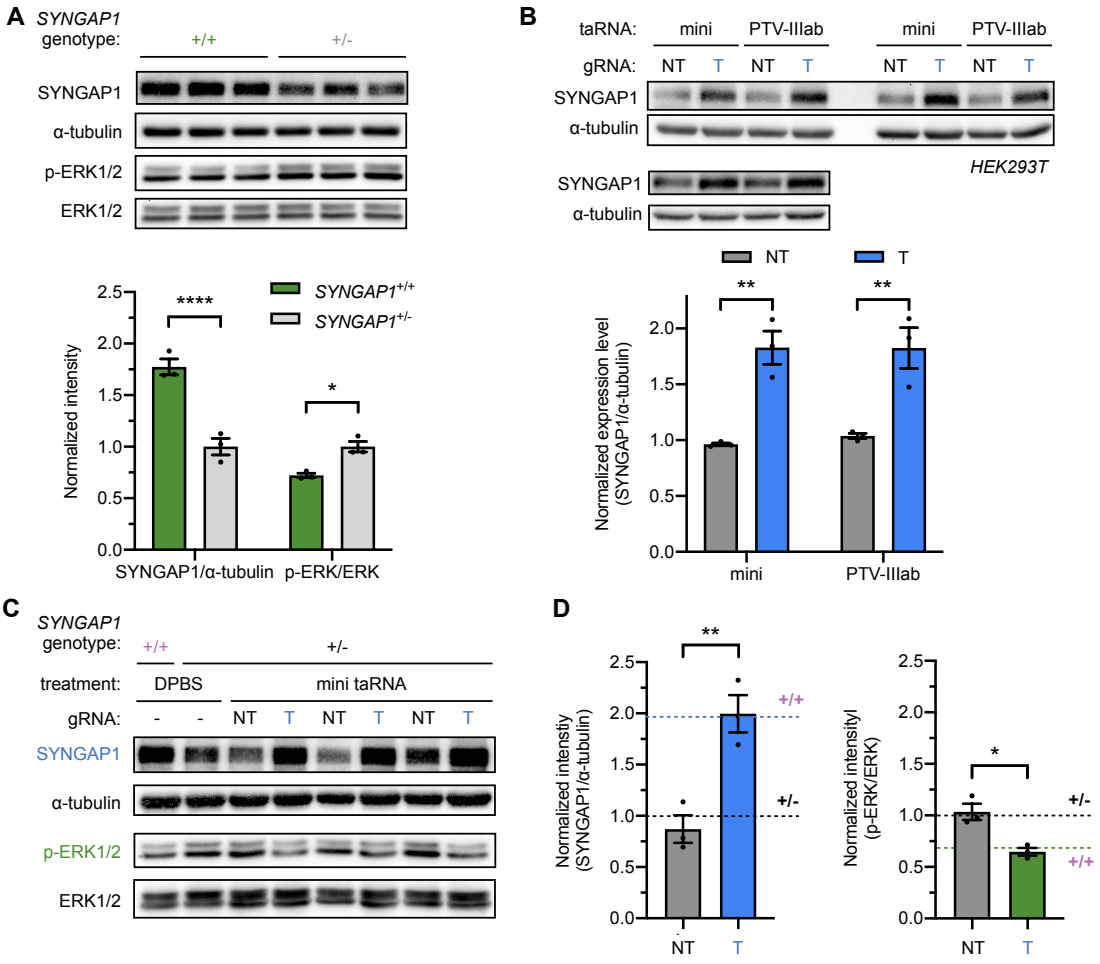

Figure 4.11 Apply SYNGAP1-targeting mini taRNA in patient-derived neurons. **(A)** Western blots of SYNGAP1 and ERK1/2 phosphorylation levels in healthy (+/+, green) or *SYNGAP1* haploinsufficient (+/-, gray) iPSC-neurons. Quantifications are shown in the lower panel, normalized to the *SYNGAP1*$^{+/+}$ level. n = 3 biological replicates. **(B)** Mini- or PTV-IIIab-based taRNAs with NT or hSYNGAP1 targeting gRNA (T) were transfected into HEK293T cells as plasmids, and human SYNGAP1 upregulation levels were compared via Western blotting. α-tubulin is the loading control. Quantification is shown below, and data were normalized to average value of NT-mini and NT-PTV-IIIab. n = 3 biological replicates. **(C)** The hSYNGAP1-targeting mini taRNA (T) and a non-targeted (NT) control was delivered by LNPs to iPSC-neurons. At 12-hour post-delivery, the levels of SYNGAP1 and phosphorylated ERK1/2 were assessed by western blots. Matched iPSC-neurons from patient (+/-) or healthy (+/+) individuals were treated with DPBS and used as a reference (dashed lines in bar graphs). **(D)** Quantifications of (C). Data were normalized to non-targeting control (NT). n=3 biological replicates. Statistical analyses were performed using Student's t test in (A) and (D), using two-way ANOVA with Sidak's multiple comparisons test vs. NT control in (B).

4.3 Conclusion and Discussion

To sum up, this chapter describes that taRNAs are compatible with both viral-delivery using AAVs and non-viral delivery by lipid nanoparticles (LNPs). We focus on LNP-packaged taRNA delivery, validated its effectiveness in cell lines, primary neurons, and *in vivo*. We further optimized the taRNA efficacy by screening more guide RNAs for better performance, and truncated the taRNA to a mini version, whose core taRNA components are less than 100 nt, falling within the range for efficient oligo synthesis. This mini taRNA was also successfully applied to *SYNGAP1* haploinsufficient iPSC-neurons derived from the patient.

The taRNA technology has great potential for therapeutic applications. The relatively modest level of upregulation achieved by taRNA is therapeutically beneficial for genetic haploinsufficiency diseases, as many of these disease-associated genes are dosage sensitive and are likewise pathogenic if elevated too much[29,146]. As a successful target of taRNA, *SYNGAP1* haploinsufficiency is one of the most common causes of intellectual disability with epilepsy[80], with no available treatments. The ongoing efforts focused on splice-switching oligonucleotides (TANGO)[35,60,61] were unable to generate protein activation *in vivo* yet, potentially because of the efficient clearance of SYNGAP1 NMD transcripts in neurons[60]. The taRNA technology presented in this study boosts protein production from productive transcripts and is therefore suitable for SYNGAP1 upregulation. Encouragingly, we found that the level of taRNA-mediated activation in *SYNGAP1* haploinsufficient neurons reached the approximate expression level of wild-type iPSC-neurons, indicating the level of activation, at least in this cell model, is within the range of therapeutic need for such a disease.

The taRNA platform also offers synergistic gene activation possibilities, if applied with multiple guide RNAs binding to the same transcript at different positions, or applied with technologies that increase the amounts of mRNAs, to reach higher levels of activation,

if needed. Finally, because taRNAs act directly on existing transcripts, the activity of taRNAs is inherently limited to cells where SYNGAP1 mRNAs are present, which is a key advantage of targeting translation as a gene activation strategy.

4.4 Material and Methods

Cloning All plasmids were cloned using Gibson Assembly and sequenced by the University of Chicago Comprehensive Cancer Center DNA Sequencing and Genotyping Facility. PCR fragments for Gibson Assembly were generated using Q5 Hot Start DNA Polymerase (NEB). All IRES sequences were synthesized as gBlocks by IDT. Key plasmids used in this study are listed in **Table 3.1** and **Table 4.1** with links to their vector maps and are available upon request. Additional guide RNA sequences are listed in **Table 4.2**, and examples of full taRNA sequences are listed in **Table 4.3**.

Mammalian cell culture and transfection For cell culture assays, HEK293T (ATCC), NIH/3T3 (ATCC) and Neuro-2a cells (ATCC) were used. Cells were maintained in Dulbecco's Modified Eagle Medium (DMEM, L-glutamine, high glucose, sodium pyruvate, phenol red; Corning) supplemented with 10% fetal bovine serum (FBS; Gemini Benchmark), and 1x penicillin/streptomycin (P/S; Gibco/Life Technologies) in a humidified 37 ℃ incubator with 5% CO2. For all experiments, cells had undergone fewer than 25 passages. For transfections, cells were plated in full media without penicillin/streptomycin and transfected at 70% confluency 18-24h later. The Lipofectamine 2000 (Invitrogen) reagent was used for HEK293T cells and lipofectamine 3000 (Invitrogen) with P3000 reagent was used for all other cell lines, according to the manufacturer's protocols. Specifically, for endogenous targets, 500 ng taRNA plasmids were used in each well of 24-well plate and 1000 ng for 12-well plate.

Western blotting The treated cells were washed with DPBS and lysed in RIPA buffer (50 mM Tris, 150 mM NaCl, 1% Triton X-100, 0.5% sodium deoxycholate, 0.1% SDS, 1 mM EDTA, pH 7.4) supplemented with protease inhibitors and phosphatase inhibitors (Santa Cruz sc-45045). After 10 min incubation at room temperature, the lysates were centrifuged to remove debris. Total protein concentration was measured by BCA assay (Thermo Scientific). 10 µg to 35 µg total protein was boiled in protein loading buffer (50 mM Tris pH 6.8, 2% SDS, 10% glycerol, 0.05% bromophenol blue, 100 mM DTT) for 5 min at 70 90 ℃ and loaded onto 8%-12% SDS-PAGE gel according to target protein size. The total protein amount loaded was confirmed to be within linear range of detection for each antibody to detect each target protein. After stacking at 90 V, the gel was run at 140 V until the dye front reached the bottom. The proteins were transferred onto a methanol activated PVDF membrane (pore size 0.45 µm; Immobilon-P from Millipore) using wet transfer apparatus (Bio-rad). Membranes were blocked with 3% BSA in TBST buffer for 1h at room temperature, incubated with primary antibody in 3% BSA-TBST at 4 ℃ overnight, and then washed with TBST buffer (4x 5 mins), followed by corresponding HRP-conjugated secondary antibody incubation 1h at room temperature. The loading control GAPDH and α-tubulin were visualized using 1:2500 HRP-conjugated anti-GAPDH or anti-α-tubulin antibody. Membranes were imaged on a Fluor Chem R (Protein Simple) imager after incubation with SuperSignal West Pico PLUS chemiluminescent substrate (Thermo Scientific). For antibody dilutions and vendor information, see **Table 3.4**.

Quantification of signal intensity on Western blots All image analysis was performed with Fiji/ImageJ. The 16-bit image from chemiluminescence channel was first set to 8-bit, then processed to subtract background using a “rolling ball” algorithm. The radius was set at 50 pixels, which is at least the size of the largest band that is not part of the background, as measured in the images. The band intensity was then measured by ImageJ within the Regions of Interest (ROIs), which is set as the same dimensions for all bands across the

same image. The mean intensity is then divided by the corresponding loading control intensity, as the quantified intensity for comparation.

AAV production and purification HEK293T cells were seeded in 100-mm or 150-mm plates. Twenty-four hours after seeding, cells were co-transfected with AAV transfer plasmids, helper plasmids (Addgene 112867), and Rep/Cap plasmids (Addgene 112862 for AAV1, 112865 for AAV9) in a 1:1:1 molar ratio using 3 µg of acidified (0.1 N HCl) polyethylenimine (PEI) per 1 µg of DNA69. The total amount of DNA transfected into cells in 100-mm or 150-mm plate is 13 or 36 µg, respectively. Culture media was replaced 24 hours after transfection. Starting from 48 hours-post transfection, cell culture media was collected every day for 3 days. AAV particles were precipitated from collected media using PEG-it Virus Precipitation Solution (System Biosciences, LV810A-1) following manufacture's protocol, and stored at 4 ℃ until use within in a week.

AAV transduction The titer of AAV was determined by qPCR using ITR primers (Fwd: GGAACCCCTAGTGATGGAGTT, Rev: CGGCCTCAGTGAGCGA). NIH/3T3 cells were seeded in 24-well plates at 0.1 x 10^6 cells/well at least 24 hours before transduction. On the day of transduction, cell culture media was replaced with AAV particles diluted in 150 µl fresh DMEM with 10% FBS without antibiotics, at multiplicity of infection (MOI) of 500,000 vg/cell. Six hours after incubation, 500 µl fresh DMEM with 10% FBS without antibiotics was added into each well. Cells were harvested 72 hours post transduction and subjected to western blot analysis.

***In vitro* transcription of mRNA and taRNA** DNA templates containing the T7 RNAP promoter were either from suitable plasmids or synthesized by IDT and were amplified by PCR prior to transcription. The template for mRNA transcription has a poly(A) tail (120 adenine nucleotides) added at its 3' end using a long reverse primer during PCR.

For a 250 µL reaction, 6 µg purified template was incubated with 1x transcription buffer (40 mM Tris-HCl, 2 mM spermidine, 10 mM NaCl), 25 mM $MgCl_2$, 10 mM DTT, 40U SUPERaseIn, 4 mM of each NTP, and 40 mg/mL T7 RNAP at 37℃ overnight. The next day, the resulting mixture was DNaseI digested in 1x DNaseI buffer (ThermoFisher) for 30 min at 37℃, and then RNA was purified using RNA Clean & Concentrator-25 (RCC-25) Kits (Zymo). For mRNAs, the eluted product was 5'-capped with ScriptCap Cap 1 Capping System (Cell Script). For taRNAs, per 10 µg eluted product was treated with 25 units alkaline phosphatase, Calf Intestinal (Quick CIP, NEB) at 37℃ for 3 hours, to remove its 5'-triphosphate for less toxicity and immunogenicity in cells[147]. The product was purified again with RCC-25 kit and checked for purity on 8M urea-PAGE gel before storage or use.

LNP formulation and characterization Nanoparticles for mPTEN-targeting taRNAs, including for delivery to mouse liver *in vivo*, were produced using the GenVoy-ILM kit (Precision NanoSystems) on a NanoAssemblr Ignite device according to the manufacturer's protocol. Briefly, 1.5 mL of taRNA at 174 µg/mL in PNI buffer provided with GenVoy-ILM kit was mixed with 0.5 mL GenVoy-ILM proprietary lipid mix under controlled conditions on Ignite device to form RNA-LNPs, which was then diluted in 78 mL DPBS buffer and re-concentrated via Amicon Ultra-15 Centrifugal Filter Units (10,000 MWCO, MilliPore). The mean diameters and polydispersity index (PDI) of the LNPs after concentration were determined by dynamic light scattering (DLS, Wyatt DynaPro NanoStar) using 25 µL of particles. Each sample were analyzed for 10 runs and averaged. The LNP solutions were then filtered through sterile syringe filters (0.22um, Acrodisc) for use.

Nanoparticles for SYNGAP1-targeting taRNAs, including for primary rat neurons or iPSC-neurons, were produced with the Neuro9 kit (Precision NanoSystems) on a Nano Assemblr Spark device (Precision NanoSystems). Briefly, 32 µL of taRNA at 930 µg/mL in FB1, 48 Formulation Buffer 2 (FB2, Precision NanoSystems) and 16 µL Nanoparticle

mix was mixed under the control of NanoAssemblr Spark device with setting 4. The RNA-LNPs are immediately added to 96 µL FB2 to be ready for characterization and use. The mean diameters and PDI of the LNPs were also determined by DLS.

The encapsulation efficiencies and concentrations of LNPs were measured using Quant-it RiboGreen RNA Assay Kit (Invitrogen). The taRNA-LNPs were incubated either in TE buffer or in Triton buffer (1% Triton X-100 in TE buffer) for 10 mins. Ribogreen reagent was then added to each incubated sample and fluorescence signal was recorded. The unencapsulated RNA amount (F_u) was determined with TE buffer incubated LNPs, and the total RNA amount (F_t) was the value from Triton buffer lysed samples. The encapsulation efficiency (%) = (F_t - F_u)/ F_t x 100.

LNP delivery of taRNAs to N2a cells About 16 h before delivery, N2a cells were plated on the 12-well plate (Corning) in full DMEM media without antibiotics, and reached 70 75% confluency at the delivery time. For each well, the indicated amount of taRNAs in LNPs were diluted with sterile DPBS buffer to make the final volume as 100 µL, which is then added dropwise to the cells. After indicated time of incubation, the cells were harvested for further analysis.

LNP delivery of taRNAs to mouse liver *in vivo* Female BALB/C mice (aged 5-6 weeks, Charles River Laboratories) received intravenous (tail vein) injections of LNPs containing 0.5 mg/kg stable hairpin-containing PTV-IIIab-based or mini taRNA (Fig. 4a), which was either non-targeting or mouse PTEN targeting. Mice were sacrificed 12h post-injection, and the liver was harvested and flash-frozen with liquid nitrogen for biochemical analysis. All animal experiments were performed following the protocols approved by the University of Chicago Institutional Animal Care and Use Committee.

Primary neuronal culture and LNP delivery Primary cultures of rat cortical neurons were prepared as described71 using Neurobasal Media (NBM), 4% (v/v) B27, and 0.125 mM L-glutamine (all from Thermo Fisher Scientific, Waltham, MA). Dissociated cortical neurons from E18 Sprague Dawley rat pups were plated in six-well plates coated with poly-D-lysine (Sigma, St Louis, MO). For western blots, 0.4×10^6 cells were plated in each well. At day 8 of culture, 1 µg taRNAs encapsulated in LNPs were added and cells were incubated for 12 h before they were harvested for western blots. For imaging, the neurons were plated at 0.25×10^6 cells per well, and at day 14 of culture, 1 µg GFP mRNA encapsulated by LNPs was added to each well, and the images were taken on an inverted epifluorescence microscope (Lieca DMi8) with a 20x objective, a Hamamatsu Orca-Flash 4.0 camera, and a 300 W Xenon light source (Sutter Lamda XL).

Generation and validation of induced pluripotent stem cells An individual heterozygous for a premature termination codon mutation (c.3190C>T, p.Q1064X) in SYNGAP1 was described previously[148]. Peripheral blood mononuclear cells from this individual were reprogrammed to induced pluripotent stem cells (iPSC) by transducing cells with Sendai virus encoding Kof4, Oct3/4, Sox2 and Myc (Cyto-Tune, ThermoFisher). Selected iPSC clonal lines were shown to be pluripotent with the Pluritest (ThermoFisher) and immunostaining for pluripotency markers. Cell lines had a normal karyotype and were free from mycoplasma infection.

Neuronal differentiation from human iPSCs and LNP delivery to iPSC-neurons Human iPSC-derived cortical excitatory neurons were generated by neurogenin-2 (NGN2) induction with modifications[149]. Briefly, human iPSCs in suspension were transduced by separate lentiviral vectors encoding neuogenin-2 driven by a tetracycline-inducible promoter (TetO-NGN2), reverse tetracycline-controlled transactivator (rtTA) and red fluorescent protein (RFP) then plated on matrigel-coated plates in mTeSR medium con-

taining 10 µM Y27632 (StemCell technologies). Cells were maintained in a transitional medium from knockout serum replacement to neural induction medium with the supplements LDN-193189 (100 nM, Stemgent, Lexington, MA), SB431542 (10 µM, StemGent), and XAV939 (2 µM, Sigma-Aldrich, St. Louis, MO). NGN2 and RFP expression were induced by 2 µg/ml doxycycline one day prior to a 48 hour selection in puromycin (2 µg/ml). After day 5, induced neuronal cells were plated over mouse glial cells cultured on poly-D-lysine/laminin coated 6-well tissue culture plates, and continually maintained in Neurobasal medium supplemented with N2, B27, BDNF (10 ng/ml, PeproTech, Rocky Hill, NJ) and doxycycline (2 µg/ml) for 33 to 55 days. At the time of treatment, 250ng taRNAs encapsulated in LNPs or DPBS at the same volume were added to each 6-well plate. Cells were incubated for 12 h before they were harvested for western blots as described above.

4.5 Supplementary Information

Table 4.1 Representative mammalian expression plasmids used in this chapter besides those in Table 3.1.

#	Name	Stock No.	Description	Plasmid Map
1	Non-targeting mini with hairpins	62-77	hU6-hp-NT (30nt)-mini-hp	https://benchling.com/s/seq-fNT3YEjcMPqZ0usoeuph?m=slm-pi9HD0pbLazKWCfwRrT7
2	Control with no recruitment domain	72-194	hU6-hp-mSYNGAP1 g4-hp	https://benchling.com/s/seq-2Tw8jxXKaCLECUkmZYvQ?m=slm-zLcpCI6drnWT1PNLqtPw

Table 4.2 taRNA guide RNA sequences used in this chapter besides those in Table 3.2.

#	Target	Sequence
1	NT(30nt)	GCCCACAUGGCAUUCCACUUAUCACUGGCA
2	g3(mSYNGAP1)	UUCUGGGUGGGGAGAGUUAAUGUAAGAGUG
3	g4(mSYNGAP1)	AGUGAAGGGGUCUGUGUGGGGUAGGUGGUG
4	g5(mSYNGAP1)	GGGUGUAUGUAGAGGGUUAGACCGAAGGAG
5	g4(mPTEN)	UGAAGAAUUAUAAAAUAUUUAAGGAGAAAA
6	g5(mPTEN)	GCAUACUGAAUAAAUCAUUGUCAAAUUUUC
7	g8(mPTEN)	AUUUUAUCCCUCUUGAUAAGAAAAAAAAAA
8	g(hSYNGAP1)	AUUACAACAGCCAAAGAAGAGAGAAGGAAG

Table 4.3 Example RNA sequences of taRNAs used in this chapter besides those in Table 3.3.

#	Name	Sequence
1	hairpin-gRNA-PTV-IIIab-hairpin	ggccagagacguucgcgucucuggccuuauuNNNNNNNNNNNNNNNNNNNNNNNNNNNNNNNNNNNNNNNNuuauuACUCCUGACUGGGUAAUGGGACUGCAUUGCAUAUCCCUAGGCACCUAUUGAGAUUUCUCUGGGGCCCACCAGCGUGGAGUucuagagcggacuucgguccgcuuuu
2	hairpin-gRNA-PTV-IIIab-hairpin	ggccagagacguucgcgucucuggccuuauuNNNNNNNNNNNNNNNNNNNNNNNNNNNNNNNNNNNNNNNNCUGGGUAAUGGGACUGCAUUGCAUAUCCCUAGGCACCUAUUGAGAUUUCUCUGGGGCCCACCAGUCUAGAgcggacuucgguccACCAGCGUGGAGUucuagagcggacuucgguccgcuuuu

CHAPTER 5

SUMMARY AND PERSPECTIVES

5.1 Expanding chemical biology approaches to study *S*-palmitoylation

The addition of a long chain palmitoyl group onto protein cysteines, known as *S*-palmitoylation, alters protein hydrophobicity dynamically by writer protein DHHC PATs and 'earser' protein ATPs. This palmitoylation-depalmitoylation cycle can mediate inter-compartment shuttling of proteins, such as the oncogene protein HRas and NRas[150]; and can alter protein-protein interactions to release active proteins, such as transcription factor RFX3[4]. In this thesis, we also find that this dynamic regulation can switch PRDX5 activity on and off, by directly modifying the active site cysteine. Such significant biological consequences, plus the wide-ranging and diverse modified protein substrates, makes *S*-palmitoylation an important aspect for study in neurobiology[151], cancer[6], and immunology[152].

Despite the broad interest, the whole *S*-palmitoylation field has been held back due to the lack of a straightforward detection method to evaluate the level of palmitoylation on the target protein. The canonical acyl-based exchange assay (ABE) is a solid method for measuring the amount of palmitoylated proteins„ which has been used as the basic assay in almost every palmitoylation[14] related research, including this thesis. However, the assay procedure is extensively long and requires repeated protein precipitation and resuspension, which introduces technical errors and severely delays the research progress. Attempts were made to image peptide substrate trafficking as indicator for *S*-palmitoylation level, which has been applied to membrane proteins shutting between cellular compartments with known palmitoylation motifs[150,153], but not suitable for all other proteins.

The depalmitoylation probes (DPPs) have offered a new angle to study the dynamic

regulation by directly assessing the activity of eraser enzymes in live cells, in real time, which are also handy and robust. Although the first successful probe, DPP-2, had to substitute a C_8 lipid chain for the natural C_{16} lipid to permit utility in live cells, in Chapter 2, we further developed DPP-5, whose additional succinylated piperazine on the probe scaffold improved solubility eventually allowed the highly hydrophobic C_{16} lipid substrate.

All previous DPPs do not have preferences for subcellular localization, providing no information on *S*-palmitoylation regulation in each cell compartment. In this thesis, we show the first mitochondria-targeted DPPs, mitoDPP-2 and mitoDPP-3, which revealed that APT1 has depalmitoylation activity in mitochondria.

On the other hand, the research on writer proteins for *S*-palmitoylation, DHHC-PATs, is hindered by the lack of a specific inhibitor[9]. The most recognized pan-inhibitor of DHHC, 2-romopalmitate (2BP), has been shown to efficiently inhibit *S*-acylation *in vitro* and in cells[154,155]. However, this inhibitor is not only cytotoxic in long-term treatment, it also targets many proteins other than DHHC PATs[156,157], including the *S*-palmitoylation 'erase' protein, APTs[158]. Our lab and others have developed improved inhibitors for a subset of DHHC PATs, with eased cell toxicity and improved target specificity[159,160]. These new inhibitors still have a handful of off-targets other than DHHC family proteins. Future research on improved pan-DHHC inhibitors is needed. Given the complicated functional redundancy within DHHC PATs, a more complete set of isoenzyme selective DHHC inhibitors will also be appreciated to profoundly promote the research about *S*-palmitoylation and potentially turned into new therapeutics.

5.2 Seeking hidden eraser proteins for *S*-palmitoylation

Discovery of unknown palmitoylation erase proteins is needed to fully understand the functions and dynamic regulations on palmitoylated protein substrates. In contrast to the large family of writer protein, DHHC PATs, the depalmitoylases are still underre-

ported. Several research reported the dynamic regulation and function of palmitoylated proteins, but could not identify the responsible eraser enzymes, such as a transcription factor RFX3[161] and a potassium channel GIRK[162], which prevented further study of regulation mechanisms on these substrates.

Following the characterization of new DPP probes, in Chapter 2, I described the identification and study of a previously unknown mitochondrial depalmitoylase, ABHD10, using these new probes. This enzyme was only reported to catalyze the deglucuronidation on acyl glucuronide (AcMPAG) before[94,95], without known endogenous substrates. From screening via DPP-2, we figured ABHD10 exhibits deacylation activity. Using DPP-5, we validated and characterized its depalmitoylation activity *in vitro* and in live cells. We found the antioxidant enzyme, PRDX5, is a endogenous substrate of ABHD10 and the palmitoyl group masks PRDX5 active site cysteine to tune its activity. The antioxidant function of PRDX5 inspired us to uncover the important role of ABHD10 on regulating mitochondrial redox homeostasis.

Apparently, ABHD10 is not the only yet-to-be-discovered depalmitoylase. In our screening efforts to identify new depalmitoylases, other proteins of the ABHD family also exhibited deacylation activity in addition to ABHD10, including ABHD3, ABHD6, ABHD9 (**Figure 2.8**). Further research could validate the depalmitoylation activity of these candidates, identify their endogenous protein substrates, and expand the knowledge of biological implications of dynamic palmitoylation cycles. In particular, ABHD3 is a single-pass type II membrane protein with little annotation on its function[163]. No membrane enzyme is known as depalmitoylase yet, although many palmitoylated proteins are membrane proteins[164]. This ABHD3, if validated, may reveal new mechanisms of how depalmitoylation affects protein function.

We found that PRDX5 is a depalmitoylation substrate for ABHD10, but there could be more mitochondrial proteins as its substrates, waiting to be identified. Given our findings

that ABHD10 is needed for oxidation-stress response, ABHD10 may play an important role in tumor growth, as hypoxia and oxidation stress are common characteristics of solid tumors[165]. The study of the impacts of ABHD10 on tumor growth may bring in new anti-tumor therapeutics. Furthermore, we obtained the crystal structure of ABHD10 at high resolution, which can facilitate the development of specific inhibitors targeting this enzyme, for research related to cell redox homeostasis and possibly anti-tumor drugs.

5.3 Innovative translation-activating technologies

Recent nucleic acid-based technologies (NBTs) have opened vast new opportunities for protein upregulation, which was historically difficult to achieve via small-molecule drugs. Although several NBTs to increase functional transcripts have advanced into clinical trials[50,62,67] or have already been approved as a successful drug[32], those aimed at modulating protein translation pathways are comparably under-developed. The translation process is the final output of an mRNA following its transcription, splicing, modifications, trafficking, and degradation. The approaches affecting translation processes result in direct effects on functional protein production, ignoring all complicated regulations that happen to the mRNA target, and can be combined with all other approaches regulating at the RNA level.

In Chapters 3 and 4, I described the development of 'translation-activating RNAs' (taRNAs), a programmable RNA platform that up-regulates the translation process of various mRNA targets in mammalian systems both *in vitro* and *in vivo*. taRNAs are synthetic modular molecules, consisting of a guide sequence domain that can be flexibly chosen from complementary sequences of the 3'UTR in a target mRNA; and an effector domain that recruits selective eIFs that are effective for accelerating the translation process.

The 3' UTR targeting feature grants extended guide RNA choices, because, on average, mammalian mRNAs have longer 3' UTRs than their 5' UTRs[113]. This is an important

advantage since we showed that different guide sequences generate taRNAs with different levels of effectiveness. Additionally, multiple effective guide sequences on the same mRNA target allow synergistic effects to boost protein production robustly and possibly to a higher level. For some specific mRNAs, the flexibility of guide RNA choices may yield translation upregulation on selective transcript isoform. These are all potential future directions to explore.

Nonetheless, the taRNA platform is not restricted to targeting 3' UTR, as the taRNA based on PTV-IRES was effective using 5' UTR guide RNA (**Figure 3.5B**). In the future, one can re-screen the IRESs library focused on 5' UTR targeting guide RNAs, to identify effector domains that are effective and prefer 5' UTR targeting as new taRNAs. The new scaffold of taRNA may reveal novel translation machinery that is effective for recruitment for translation activation and can be applied together with 3' UTR-targeting taRNAs to test synergistic effects.

As there are many more structured RNA elements that drive mRNA translation, which we did not screen[166], in this proof-of-concept work, more effector domains are waiting to be identified and validated for the expanded taRNA platform in the future. Beyond the natural RNA elements, one could also build artificial effector domains from, for example, aptamers. RNA aptamers are short, single-stranded RNA molecules that can selectively bind to a specific target, including proteins, with high affinity and specificity[167]. Aptamers are usually selected from libraries of RNA molecules through SELEX, and are not always inhibitors of their binding targets[168]. There are known non-inhibitory aptamers for eIF4G[169], which was an effective eIF to activate the translation of the target mRNA when recruited by EMCV-JK-based taRNA (**Figure 3.9**). SELEX can be performed on other eIFs or eIF4G to generate more aptamer candidates to test as taRNA effector domains in the future.

Beyond the limitations of an RNA-based scaffold, it will be groundbreaking if bifunc-

tional small molecules, or small molecules combined with short oligos, can achieve programmable translation activation on the mRNA target. This requires small molecules to recruit active eIFs, specifically to a target of interest. Our work presented in Chapter 3 has confirmed the effectiveness of eIF3 and eIF4G as candidate targets to be recruited for translation activation. Future research could focus on creating small molecules for these two protein complexes as targets. To bind specific mRNA targets, it is easy to utilize short complementary oligos; or possibly small molecules, which have been realized on a handful of special mRNAs with structural RNA elements[170].

Finally, we demonstrate that taRNAs can increase protein synthesis from a variety of mRNAs of interest in human and mouse cells, and showcase the efficacy of taRNA on a haploinsufficient gene target, *SYNGAP1*, in a disease cell model. Given the programmability of the taRNA platform, it can be readily engineered to act on other disease-related gene expression in the future.

5.4 Delivery of translation-activating RNAs for clinical applications

The taRNAs can immediately plug into existing AAV delivery pipelines for therapeutic development in cases where long-term gene expression changes are the goal. We also demonstrated the efficacy of LNP-delivered taRNAs as non-modified RNAs in primary neurons, iPSC-neurons, and mouse model, proving that the utility of taRNAs can be dramatically expanded with non-viral, oligo-based delivery approaches. In recent years, significant progress has been made in designing LNPs to deliver mRNA or small interfering RNA (siRNA) for clinical applications[171,172].

Unmodified oligonucleotides do not have optimal pharmacokinetic properties, mainly because of their degradation by ribonucleases. Recent advances around chemical modifications of oligos, such as internucleotide bond modifications by phosphorothioate (PS); and 2' ribose substitutions by 2'-O-methyl (2'-OMe), 2'-O-methoxyethyl (2'-MOE) or 2'-

fluoro, enhance nuclease resistance and serum stability[173]. Modifications such as locked nucleic acids (LNAs) can also enhance the binding affinity to target RNA in vivo[174]. The taRNA system can plug into related oligo-based pipelines for gene knockdown[171], editing[175,176], and splicing[55], adding an approach for targeted gene activation to the repertoire of NBT strategies. In Chapter 4, we built a mini taRNA scaffold of 94 nt, which falls into a suitable length for oligo synthesis and chemical modifications. In the future, adequate modifications of mini taRNA can enhance its stability and reduce its immunogenicity. These improvements in the engineering, chemistry, and delivery of taRNAs will pave the way toward a broader clinical deployment.

REFERENCES

1. Hernandez, J. L.; Majmudar, J. D.; Martin, B. R. Profiling and Inhibiting Reversible Palmitoylation. *Current Opinion in Chemical Biology* **2013**, *17*, 20–26.

2. Dekker, F. J.; Rocks, O.; Vartak, N.; Menninger, S.; Hedberg, C. et al. Small-Molecule Inhibition of APT1 Affects Ras Localization and Signaling. *Nat Chem Biol* **2010**, *6*, 449–56.

3. Brownlee, C.; Heald, R. Importin Alpha Partitioning to the Plasma Membrane Regulates Intracellular Scaling. *Cell* **2019**, *176*, 805–815 e8.

4. Chan, P.; Han, X.; Zheng, B.; DeRan, M.; Yu, J. et al. Autopalmitoylation of TEAD Proteins Regulates Transcriptional Output of the Hippo Pathway. *Nat Chem Biol* **2016**, *12*, 282–9.

5. Chen, S.; Zhu, B.; Yin, C.; Liu, W.; Han, C. et al. Palmitoylation-Dependent Activation of MC1R Prevents Melanomagenesis. *Nature* **2017**, *549*, 399–403.

6. Ko, P. J.; Dixon, S. J. Protein Palmitoylation and Cancer. *EMBO Rep* **2018**, *19*.

7. Zareba-Koziol, M.; Figiel, I.; Bartkowiak-Kaczmarek, A.; Wlodarczyk, J. Insights Into Protein S-Palmitoylation in Synaptic Plasticity and Neurological Disorders: Potential and Limitations of Methods for Detection and Analysis. *Front Mol Neurosci* **2018**, *11*, 175.

8. Sobocinska, J.; Roszczenko-Jasinska, P.; Ciesielska, A.; Kwiatkowska, K. Protein Palmitoylation and Its Role in Bacterial and Viral Infections. *Front Immunol* **2017**, *8*, 2003.

9. Lan, T.; Delalande, C.; Dickinson, B. C. Inhibitors of DHHC Family Proteins. *Current Opinion in Chemical Biology* **2021**, *65*, 118–125.

10. Duncan, J. A.; Gilman, A. G. A Cytoplasmic Acyl-Protein Thioesterase That Removes Palmitate from G Protein Alpha Subunits and P21(RAS). *J Biol Chem* **1998**, *273*, 15830–7.

11. Lin, D. T.; Conibear, E. ABHD17 Proteins Are Novel Protein Depalmitoylases That Regulate N-Ras Palmitate Turnover and Subcellular Localization. *Elife* **2015**, *4*, e11306.

12. Long, J. Z.; Cravatt, B. F. The Metabolic Serine Hydrolases and Their Functions in Mammalian Physiology and Disease. *Chem Rev* **2011**, *111*, 6022–63.

13. Yokoi, N.; Fukata, Y.; Sekiya, A.; Murakami, T.; Kobayashi, K. et al. Identification of PSD-95 Depalmitoylating Enzymes. *J Neurosci* **2016**, *36*, 6431–44.

14. Wan, J.; Roth, A. F.; Bailey, A. O.; Davis, N. G. Palmitoylated Proteins: Purification and Identification. *Nat Protoc* **2007**, *2*, 1573–84.

15. Forrester, M. T.; Hess, D. T.; Thompson, J. W.; Hultman, R.; Moseley, M. A. et al. Site-Specific Analysis of Protein S-acylation by Resin-Assisted Capture [S]. *Journal of Lipid Research* **2011**, *52*, 393–398.

16. Percher, A.; Ramakrishnan, S.; Thinon, E.; Yuan, X.; Yount, J. S. et al. Mass-Tag Labeling Reveals Site-Specific and Endogenous Levels of Protein S-fatty Acylation. *Proceedings of the National Academy of Sciences* **2016**, *113*, 4302–4307.

17. Charron, G.; Wilson, J.; Hang, H. C. Chemical Tools for Understanding Protein Lipidation in Eukaryotes. *Current Opinion in Chemical Biology* **2009**, *13*, 382–391.

18. Martin, B. R.; Wang, C.; Adibekian, A.; Tully, S. E.; Cravatt, B. F. Global Profiling of Dynamic Protein Palmitoylation. *Nat Methods* **2011**, *9*, 84–9.

19. Yap, M. C.; Kostiuk, M. A.; Martin, D. D. O.; Perinpanayagam, M. A.; Hak, P. G. et al. Rapid and Selective Detection of Fatty Acylated Proteins Using ω-Alkynyl-Fatty Acids and Click Chemistry [S]. *Journal of Lipid Research* **2010**, *51*, 1566–1580.

20. Kathayat, R. S.; Elvira, P. D.; Dickinson, B. C. A Fluorescent Probe for Cysteine Depalmitoylation Reveals Dynamic APT Signaling. *Nat Chem Biol* **2017**, *13*, 150–152.

21. Kathayat, R. S.; Dickinson, B. C. Measuring S-Depalmitoylation Activity In Vitro and In Live Cells with Fluorescent Probes. *Methods Mol Biol* **2019**, *2009*, 99–109.

22. Beck, M. W.; Kathayat, R. S.; Cham, C. M.; Chang, E. B.; Dickinson, B. C. Michael Addition-Based Probes for Ratiometric Fluorescence Imaging of Protein S-depalmitoylases in Live Cells and Tissues. *Chemical Science* **2017**, *8*, 7588–7592.

23. Blanc, M.; David, F.; Abrami, L.; Migliozzi, D.; Armand, F. et al. SwissPalm: Protein Palmitoylation Database. *F1000Res* **2015**, *4*, 261.

24. Adachi, N.; Hess, D. T.; McLaughlin, P.; Stamler, J. S. S-Palmitoylation of a Novel Site in the B2-Adrenergic Receptor Associated with a Novel Intracellular Itinerary. *The Journal of Biological Chemistry* **2016**, *291*, 20232–20246.

25. Hou, J.; Zhang, H.; Liu, J.; Zhao, Z.; Wang, J. et al. YTHDF2 Reduction Fuels Inflammation and Vascular Abnormalization in Hepatocellular Carcinoma. *Mol Cancer* **2019**, *18*, 163.

26. Cochran, J. N.; Geier, E. G.; Bonham, L. W.; Newberry, J. S.; Amaral, M. D. et al. Non-Coding and Loss-of-Function Coding Variants in TET2 Are Associated with Multiple Neurodegenerative Diseases. *Am J Hum Genet* **2020**, *106*, 632–645.

27. Matharu, N.; Rattanasopha, S.; Tamura, S.; Maliskova, L.; Wang, Y. et al. CRISPR-mediated Activation of a Promoter or Enhancer Rescues Obesity Caused by Haploinsufficiency. *Science* **2019**, *363*.

28. Berryer, M. H.; Hamdan, F. F.; Klitten, L. L.; Moller, R. S.; Carmant, L. et al. Mutations in SYNGAP1 Cause Intellectual Disability, Autism, and a Specific Form of Epilepsy by Inducing Haploinsufficiency. *Hum Mutat* **2013**, *34*, 385–94.

29. Li, J.; Parker, B.; Martyn, C.; Natarajan, C.; Guo, J. The PMP22 Gene and Its Related Diseases. *Mol Neurobiol* **2013**, *47*, 673–98.

30. Crooke, S. T.; Baker, B. F.; Crooke, R. M.; Liang, X. H. Antisense Technology: An Overview and Prospectus. *Nat Rev Drug Discov* **2021**, *20*, 427–453.

31. Roberts, T. C.; Langer, R.; Wood, M. J. A. Advances in Oligonucleotide Drug Delivery. *Nat Rev Drug Discov* **2020**, *19*, 673–694.

32. Finkel, R. S.; Mercuri, E.; Darras, B. T.; Connolly, A. M.; Kuntz, N. L. et al. Nusinersen versus Sham Control in Infantile-Onset Spinal Muscular Atrophy. *N Engl J Med* **2017**, *377*, 1723–1732.

33. Khorkova, O.; Stahl, J.; Joji, A.; Volmar, C. H.; Wahlestedt, C. Amplifying Gene Expression with RNA-targeted Therapeutics. *Nat Rev Drug Discov* **2023**, 1–23.

34. Sahin, U.; Kariko, K.; Tureci, O. mRNA-based Therapeutics–Developing a New Class of Drugs. *Nat Rev Drug Discov* **2014**, *13*, 759–80.

35. Lim, K. H.; Han, Z.; Jeon, H. Y.; Kach, J.; Jing, E. et al. Antisense Oligonucleotide Modulation of Non-Productive Alternative Splicing Upregulates Gene Expression. *Nat Commun* **2020**, *11*, 3501.

36. Modarresi, F.; Faghihi, M. A.; Lopez-Toledano, M. A.; Fatemi, R. P.; Magistri, M. et al. Inhibition of Natural Antisense Transcripts in Vivo Results in Gene-Specific Transcriptional Upregulation. *Nat Biotechnol* **2012**, *30*, 453–9.

37. Li, L. C.; Okino, S. T.; Zhao, H.; Pookot, D.; Place, R. F. et al. Small dsRNAs Induce Transcriptional Activation in Human Cells. *Proc Natl Acad Sci U S A* **2006**, *103*, 17337–42.

38. Janowski, B. A.; Younger, S. T.; Hardy, D. B.; Ram, R.; Huffman, K. E. et al. Activating Gene Expression in Mammalian Cells with Promoter-Targeted Duplex RNAs. *Nat Chem Biol* **2007**, *3*, 166–73.

39. Liang, X. H.; Sun, H.; Shen, W.; Wang, S.; Yao, J. et al. Antisense Oligonucleotides Targeting Translation Inhibitory Elements in 5' UTRs Can Selectively Increase Protein Levels. *Nucleic Acids Res* **2017**, *45*, 9528–9546.

40. Liang, X. H.; Shen, W.; Sun, H.; Migawa, M. T.; Vickers, T. A. et al. Translation Efficiency of mRNAs Is Increased by Antisense Oligonucleotides Targeting Upstream Open Reading Frames. *Nat Biotechnol* **2016**, *34*, 875–80.

41. Zucchelli, S.; Fasolo, F.; Russo, R.; Cimatti, L.; Patrucco, L. et al. SINEUPs Are Modular Antisense Long Non-Coding RNAs That Increase Synthesis of Target Proteins in Cells. *Front Cell Neurosci* **2015**, *9*, 174.

42. Yao, Y.; Jin, S.; Long, H.; Yu, Y.; Zhang, Z. et al. RNAe: An Effective Method for Targeted Protein Translation Enhancement by Artificial Non-Coding RNA with SINEB2 Repeat. *Nucleic Acids Res* **2015**, *43*, e58.

43. Verdera, H. C.; Kuranda, K.; Mingozzi, F. AAV Vector Immunogenicity in Humans: A Long Journey to Successful Gene Transfer. *Molecular Therapy* **2020**, *28*, 723–746.

44. Cao, J.; Choi, M.; Guadagnin, E.; Soty, M.; Silva, M. et al. mRNA Therapy Restores Euglycemia and Prevents Liver Tumors in Murine Model of Glycogen Storage Disease. *Nature Communications* **2021**, *12*, 3090.

45. Rowe, S. M.; Zuckerman, J. B.; Dorgan, D.; Lascano, J.; McCoy, K. et al. Inhaled mRNA Therapy for Treatment of Cystic Fibrosis: Interim Results of a Randomized, Double-blind, Placebo-controlled Phase 1/2 Clinical Study. *Journal of Cystic Fibrosis* **2023**,

46. Barbier, A. J.; Jiang, A. Y.; Zhang, P.; Wooster, R.; Anderson, D. G. The Clinical Progress of mRNA Vaccines and Immunotherapies. *Nature Biotechnology* **2022**, *40*, 840–854.

47. Belbellaa, B.; Reutenauer, L.; Messaddeq, N.; Monassier, L.; Puccio, H. High Levels of Frataxin Overexpression Lead to Mitochondrial and Cardiac Toxicity in Mouse Models. *Molecular Therapy - Methods & Clinical Development* **2020**, *19*, 120–138.

48. Van Alstyne, M.; Tattoli, I.; Delestrée, N.; Recinos, Y.; Workman, E. et al. Gain of Toxic Function by Long-Term AAV9-mediated SMN Overexpression in the Sensorimotor Circuit. *Nature Neuroscience* **2021**, *24*, 930–940.

49. Hu, B.; Zhong, L.; Weng, Y.; Peng, L.; Huang, Y. et al. Therapeutic siRNA: State of the Art. *Signal Transduction and Targeted Therapy* **2020**, *5*, 1–25.

50. Reebye, V.; Huang, K. W.; Lin, V.; Jarvis, S.; Cutilas, P. et al. Gene Activation of CEBPA Using saRNA: Preclinical Studies of the First in Human saRNA Drug Candidate for Liver Cancer. *Oncogene* **2018**, *37*, 3216–3228.

51. Sarker, D.; Plummer, R.; Meyer, T.; Sodergren, M. H.; Basu, B. et al. MTL-CEBPA, a Small Activating RNA Therapeutic Upregulating C/EBP-α, in Patients with Advanced Liver Cancer: A First-in-Human, Multicenter, Open-Label, Phase I Trial. *Clinical Cancer Research* **2020**, *26*, 3936–3946.

52. Ohno, S.-i.; Oikawa, K.; Tsurui, T.; Harada, Y.; Ono, K. et al. Nuclear microRNAs Release Paused Pol II via the DDX21-CDK9 Complex. *Cell Reports* **2022**, *39*.

53. Cao, H.; Meng, X.; Wang, X.; Liang, Z. In *RNA Activation*; Li, L.-C., Ed.; Advances in Experimental Medicine and Biology; Springer: Singapore, 2017; pp 41–51.

54. Chen, M.; Manley, J. L. Mechanisms of Alternative Splicing Regulation: Insights from Molecular and Genomics Approaches. *Nature Reviews Molecular Cell Biology* **2009**, *10*, 741–754.

55. Havens, M. A.; Hastings, M. L. Splice-Switching Antisense Oligonucleotides as Therapeutic Drugs. *Nucleic Acids Res* **2016**, *44*, 6549–63.

56. Wheeler, T. M.; Lueck, J. D.; Swanson, M. S.; Dirksen, R. T.; Thornton, C. A. Correction of ClC-1 Splicing Eliminates Chloride Channelopathy and Myotonia in Mouse Models of Myotonic Dystrophy. *The Journal of Clinical Investigation* **2007**, *117*, 3952–3957.

57. Hinrich, A. J.; Jodelka, F. M.; Chang, J. L.; Brutman, D.; Bruno, A. M. et al. Therapeutic Correction of ApoER2 Splicing in Alzheimer's Disease Mice Using Antisense Oligonucleotides. *EMBO Molecular Medicine* **2016**, *8*, 328–345.

58. Lareau, L. F.; Brooks, A. N.; Soergel, D. A. W.; Meng, Q.; Brenner, S. E. The Coupling of Alternative Splicing and Nonsense-Mediated mRNA Decay. *Advances in Experimental Medicine and Biology* **2007**, *623*, 190–211.

59. Preußner, M.; Smith, H. L.; Hughes, D.; Zhang, M.; Emmerichs, A.-K. et al. ASO Targeting RBM3 Temperature-Controlled Poison Exon Splicing Prevents Neurodegeneration in Vivo. *EMBO molecular medicine* **2023**, *15*, e17157.

60. Dawicki-McKenna, J. M.; Felix, A. J.; Waxman, E. A.; Cheng, C.; Amado, D. A. et al. Mapping PTBP2 Binding in Human Brain Identifies SYNGAP1 as a Target for Therapeutic Splice Switching. *Nat Commun* **2023**, *14*, 2628.

61. Yang, R.; Feng, X.; Arias-Cavieres, A.; Mitchell, R. M.; Polo, A. et al. Upregulation of SYNGAP1 Expression in Mice and Human Neurons by Redirecting Alternative Splicing. *Neuron* **2023**, *111*, 1637–1650 e5.

62. Han, Z.; Chen, C.; Christiansen, A.; Ji, S.; Lin, Q. et al. Antisense Oligonucleotides Increase Scn1a Expression and Reduce Seizures and SUDEP Incidence in a Mouse Model of Dravet Syndrome. *Sci Transl Med* **2020**, *12*.

63. Bartel, D. P. MicroRNAs: Genomics, Biogenesis, Mechanism, and Function. *Cell* **2004**, *116*, 281–297.

64. Pelechano, V.; Steinmetz, L. M. Gene Regulation by Antisense Transcription. *Nature Reviews Genetics* **2013**, *14*, 880–893.

65. Krützfeldt, J.; Rajewsky, N.; Braich, R.; Rajeev, K. G.; Tuschl, T. et al. Silencing of microRNAs in Vivo with 'Antagomirs'. *Nature* **2005**, *438*, 685–689.

66. Raue, R.; Frank, A.-C.; Syed, S. N.; Brüne, B. Therapeutic Targeting of MicroRNAs in the Tumor Microenvironment. *International Journal of Molecular Sciences* **2021**, *22*, 2210.

67. Hsiao, J.; Yuan, T. Y.; Tsai, M. S.; Lu, C. Y.; Lin, Y. C. et al. Upregulation of Haploinsufficient Gene Expression in the Brain by Targeting a Long Non-coding RNA Improves Seizure Phenotype in a Model of Dravet Syndrome. *EBioMedicine* **2016**, *9*, 257–277.

68. Barbosa, C.; Peixeiro, I.; Romão, L. Gene Expression Regulation by Upstream Open Reading Frames and Human Disease. *PLOS Genetics* **2013**, *9*, e1003529.

69. Bastide, A.; Karaa, Z.; Bornes, S.; Hieblot, C.; Lacazette, E. et al. An Upstream Open Reading Frame within an IRES Controls Expression of a Specific VEGF-A Isoform. *Nucleic Acids Research* **2008**, *36*, 2434–2445.

70. Occhi, G.; Regazzo, D.; Trivellin, G.; Boaretto, F.; Ciato, D. et al. A Novel Mutation in the Upstream Open Reading Frame of the CDKN1B Gene Causes a MEN4 Phenotype. *PLoS genetics* **2013**, *9*, e1003350.

71. Wiestner, A.; Schlemper, R. J.; van der Maas, A. P.; Skoda, R. C. An Activating Splice Donor Mutation in the Thrombopoietin Gene Causes Hereditary Thrombocythaemia. *Nature Genetics* **1998**, *18*, 49–52.

72. Mansur, A. T.; Elcioglu, N. H.; Redler, S.; Serdar, Z. A.; Cetinel, S. et al. Marie Unna Hereditary Hypotrichosis: A Turkish Family with Loss of Eyebrows and a U2HR Mutation. *American Journal of Medical Genetics. Part A* **2010**, *152A*, 2628–2633.

73. Carrieri, C.; Cimatti, L.; Biagioli, M.; Beugnet, A.; Zucchelli, S. et al. Long Non-Coding Antisense RNA Controls Uchl1 Translation through an Embedded SINEB2 Repeat. *Nature* **2012**, *491*, 454–457.

74. Patrucco, L.; Chiesa, A.; Soluri, M. F.; Fasolo, F.; Takahashi, H. et al. Engineering Mammalian Cell Factories with SINEUP Noncoding RNAs to Improve Translation of Secreted Proteins. *Gene* **2015**, *569*, 287–293.

75. Bon, C.; Luffarelli, R.; Russo, R.; Fortuni, S.; Pierattini, B. et al. SINEUP Non-Coding RNAs Rescue Defective Frataxin Expression and Activity in a Cellular Model of Friedreich's Ataxia. *Nucleic Acids Research* **2019**, *47*, 10728–10743.

76. Espinoza, S.; Scarpato, M.; Damiani, D.; Managò, F.; Mereu, M. et al. SINEUP Noncoding RNA Targeting GDNF Rescues Motor Deficits and Neurodegeneration in a Mouse Model of Parkinson's Disease. *Molecular Therapy* **2020**, *28*, 642–652.

77. Espinoza, S.; Bon, C.; Valentini, P.; Pierattini, B.; Matey, A. T. et al. SINEUPs: A Novel Toolbox for RNA Therapeutics. *Essays Biochem* **2021**, *65*, 775–789.

78. Sellars, E.; Gabra, M.; Salmena, L. The Complex Landscape of PTEN mRNA Regulation. *Cold Spring Harbor Perspectives in Medicine* **2020**, *10*, a036236.

79. Islam, M. A.; Xu, Y.; Tao, W.; Ubellacker, J. M.; Lim, M. et al. Restoration of Tumour-Growth Suppression in Vivo via Systemic Nanoparticle-Mediated Delivery of PTEN mRNA. *Nature Biomedical Engineering* **2018**, *2*, 850–864.

80. Deciphering Developmental Disorders, S. Large-Scale Discovery of Novel Genetic Causes of Developmental Disorders. *Nature* **2015**, *519*, 223–8.

81. Dong, J. Y.; Fan, P. D.; Frizzell, R. A. Quantitative Analysis of the Packaging Capacity of Recombinant Adeno-Associated Virus. *Hum Gene Ther* **1996**, *7*, 2101–12.

82. Rumbaugh, G.; Adams, J. P.; Kim, J. H.; Huganir, R. L. SynGAP Regulates Synaptic Strength and Mitogen-Activated Protein Kinases in Cultured Neurons. *Proceedings of the National Academy of Sciences* **2006**, *103*, 4344–4351.

83. Gou, G.; Roca-Fernandez, A.; Kilinc, M.; Serrano, E.; Reig-Viader, R. et al. SynGAP Splice Variants Display Heterogeneous Spatio-Temporal Expression and Subcellular Distribution in the Developing Mammalian Brain. *J Neurochem* **2020**, *154*, 618–634.

84. Kim, J. H.; Liao, D.; Lau, L. F.; Huganir, R. L. SynGAP: A Synaptic RasGAP That Associates with the PSD-95/SAP90 Protein Family. *Neuron* **1998**, *20*, 683–91.

85. Kostiuk, M. A.; Corvi, M. M.; Keller, B. O.; Plummer, G.; Prescher, J. A. et al. Identification of Palmitoylated Mitochondrial Proteins Using a Bio-Orthogonal Azido-Palmitate Analogue. *FASEB J* **2008**, *22*, 721–32.

86. Tang, M.; Lu, L.; Huang, Z.; Chen, L. Palmitoylation Signaling: A Novel Mechanism of Mitochondria Dynamics and Diverse Pathologies. *Acta Biochim Biophys Sin (Shanghai)* **2018**, *50*, 831–833.

87. Maynard, T. M.; Meechan, D. W.; Dudevoir, M. L.; Gopalakrishna, D.; Peters, A. Z. et al. Mitochondrial Localization and Function of a Subset of 22q11 Deletion Syndrome Candidate Genes. *Mol Cell Neurosci* **2008**, *39*, 439–51.

88. Shen, L. F.; Chen, Y. J.; Liu, K. M.; Haddad, A. N. S.; Song, I. W. et al. Role of S-Palmitoylation by ZDHHC13 in Mitochondrial Function and Metabolism in Liver. *Sci Rep* **2017**, *7*, 2182.

89. Knoops, B.; Goemaere, J.; Van der Eecken, V.; Declercq, J. P. Peroxiredoxin 5: Structure, Mechanism, and Function of the Mammalian Atypical 2-Cys Peroxiredoxin. *Antioxid Redox Signal* **2011**, *15*, 817–29.

90. Murphy, M. P. Targeting Lipophilic Cations to Mitochondria. *Biochimica Et Biophysica Acta* **2008**, *1777*, 1028–1031.

91. Dickinson, B. C.; Chang, C. J. A Targetable Fluorescent Probe for Imaging Hydrogen Peroxide in the Mitochondria of Living Cells. *J Am Chem Soc* **2008**, *130*, 9638–9.

92. Kathayat, R. S.; Cao, Y.; Elvira, P. D.; Sandoz, P. A.; Zaballa, M. E. et al. Active and Dynamic Mitochondrial S-depalmitoylation Revealed by Targeted Fluorescent Probes. *Nat Commun* **2018**, *9*, 334.

93. Rhee, H. W.; Zou, P.; Udeshi, N. D.; Martell, J. D.; Mootha, V. K. et al. Proteomic Mapping of Mitochondria in Living Cells via Spatially Restricted Enzymatic Tagging. *Science* **2013**, *339*, 1328–1331.

94. Ito, Y.; Fukami, T.; Yokoi, T.; Nakajima, M. An Orphan Esterase ABHD10 Modulates Probenecid Acyl Glucuronidation in Human Liver. *Drug Metab Dispos* **2014**, *42*, 2109–16.

95. Iwamura, A.; Fukami, T.; Higuchi, R.; Nakajima, M.; Yokoi, T. Human Alpha/Beta Hydrolase Domain Containing 10 (ABHD10) Is Responsible Enzyme for Deglucuronidation of Mycophenolic Acid Acyl-Glucuronide in Liver. *J Biol Chem* **2012**, *287*, 9240–9.

96. Won, S. J.; Davda, D.; Labby, K. J.; Hwang, S. Y.; Pricer, R. et al. Molecular Mechanism for Isoform-Selective Inhibition of Acyl Protein Thioesterases 1 and 2 (APT1 and APT2). *ACS Chem Biol* **2016**, *11*, 3374–3382.

97. Devedjiev, Y.; Dauter, Z.; Kuznetsov, S. R.; Jones, T. L.; Derewenda, Z. S. Crystal Structure of the Human Acyl Protein Thioesterase I from a Single X-ray Data Set to 1.5 A. *Structure* **2000**, *8*, 1137–46.

98. Martin, B. R.; Cravatt, B. F. Large-Scale Profiling of Protein Palmitoylation in Mammalian Cells. *Nat Methods* **2009**, *6*, 135–8.

99. Rhee, S. G.; Kil, I. S. Multiple Functions and Regulation of Mammalian Peroxiredoxins. *Annu Rev Biochem* **2017**, *86*, 749–775.

100. Sugimoto, H.; Hayashi, H.; Yamashita, S. Purification, cDNA Cloning, and Regulation of Lysophospholipase from Rat Liver. *J Biol Chem* **1996**, *271*, 7705–11.

101. Amara, N.; Foe, I. T.; Onguka, O.; Garland, M.; Bogyo, M. Synthetic Fluorogenic Peptides Reveal Dynamic Substrate Specificity of Depalmitoylases. *Cell Chem Biol* **2019**, *26*, 35–47 e7.

102. Parvez, S.; Long, M. J. C.; Poganik, J. R.; Aye, Y. Redox Signaling by Reactive Electrophiles and Oxidants. *Chem Rev* **2018**, *118*, 8798–8888.

103. Corvi, M. M.; Soltys, C. L.; Berthiaume, L. G. Regulation of Mitochondrial Carbamoyl-Phosphate Synthetase 1 Activity by Active Site Fatty Acylation. *J Biol Chem* **2001**, *276*, 45704–12.

104. Frohlich, M.; Dejanovic, B.; Kashkar, H.; Schwarz, G.; Nussberger, S. S-Palmitoylation Represents a Novel Mechanism Regulating the Mitochondrial Targeting of BAX and Initiation of Apoptosis. *Cell Death Dis* **2014**, *5*, e1057.

105. Qiu, T.; Kathayat, R. S.; Cao, Y.; Beck, M. W.; Dickinson, B. C. A Fluorescent Probe with Improved Water Solubility Permits the Analysis of Protein S-Depalmitoylation Activity in Live Cells. *Biochemistry* **2018**, *57*, 221–225.

106. McCoy, A. J.; Grosse-Kunstleve, R. W.; Adams, P. D.; Winn, M. D.; Storoni, L. C. et al. Phaser Crystallographic Software. *J Appl Crystallogr* **2007**, *40*, 658–674.

107. Peng, J.; Xu, J. RaptorX: Exploiting Structure Information for Protein Alignment by Statistical Inference. *Proteins* **2011**, *79 Suppl 10*, 161–71.

108. Kallberg, M.; Wang, H.; Wang, S.; Peng, J.; Wang, Z. et al. Template-Based Protein Structure Modeling Using the RaptorX Web Server. *Nat Protoc* **2012**, *7*, 1511–22.

109. Adams, P. D.; Afonine, P. V.; Bunkoczi, G.; Chen, V. B.; Davis, I. W. et al. PHENIX: A Comprehensive Python-based System for Macromolecular Structure Solution. *Acta Crystallogr D Biol Crystallogr* **2010**, *66*, 213–21.

110. Emsley, P.; Lohkamp, B.; Scott, W. G.; Cowtan, K. Features and Development of Coot. *Acta Crystallogr D Biol Crystallogr* **2010**, *66*, 486–501.

111. Mailliot, J.; Martin, F. Viral Internal Ribosomal Entry Sites: Four Classes for One Goal. *Wiley Interdiscip Rev RNA* **2018**, *9*.

112. Hellen, C. U.; Sarnow, P. Internal Ribosome Entry Sites in Eukaryotic mRNA Molecules. *Genes Dev* **2001**, *15*, 1593–612.

113. Mignone, F.; Gissi, C.; Liuni, S.; Pesole, G. Untranslated Regions of mRNAs. *Genome Biol* **2002**, *3*, REVIEWS0004.

114. Komar, A. A.; Hatzoglou, M. Cellular IRES-mediated Translation: The War of ITAFs in Pathophysiological States. *Cell Cycle* **2011**, *10*, 229–40.

115. Jackson, R. J.; Hellen, C. U.; Pestova, T. V. The Mechanism of Eukaryotic Translation Initiation and Principles of Its Regulation. *Nat Rev Mol Cell Biol* **2010**, *11*, 113–27.

116. Wang, X.; Zhao, B. S.; Roundtree, I. A.; Lu, Z.; Han, D. et al. N(6)-Methyladenosine Modulates Messenger RNA Translation Efficiency. *Cell* **2015**, *161*, 1388–99.

117. Rauch, S.; He, E.; Srienc, M.; Zhou, H.; Zhang, Z. et al. Programmable RNA-Guided RNA Effector Proteins Built from Human Parts. *Cell* **2019**, *178*, 122–134 e12.

118. Rauch, S.; He, C.; Dickinson, B. C. Targeted m(6)A Reader Proteins To Study Epitranscriptomic Regulation of Single RNAs. *J Am Chem Soc* **2018**, *140*, 11974–11981.

119. Luo, E. C.; Nathanson, J. L.; Tan, F. E.; Schwartz, J. L.; Schmok, J. C. et al. Large-Scale Tethered Function Assays Identify Factors That Regulate mRNA Stability and Translation. *Nat Struct Mol Biol* **2020**, *27*, 989–1000.

120. Jaafar, Z. A.; Kieft, J. S. Viral RNA Structure-Based Strategies to Manipulate Translation. *Nat Rev Microbiol* **2019**, *17*, 110–123.

121. Truniger, V.; Miras, M.; Aranda, M. A. Structural and Functional Diversity of Plant Virus 3'-Cap-Independent Translation Enhancers (3'-CITEs). *Front Plant Sci* **2017**, *8*, 2047.

122. Paek, K. Y.; Hong, K. Y.; Ryu, I.; Park, S. M.; Keum, S. J. et al. Translation Initiation Mediated by RNA Looping. *Proc Natl Acad Sci U S A* **2015**, *112*, 1041–6.

123. Acevedo, J. M.; Hoermann, B.; Schlimbach, T.; Teleman, A. A. Changes in Global Translation Elongation or Initiation Rates Shape the Proteome via the Kozak Sequence. *Sci Rep* **2018**, *8*, 4018.

124. Lozano, G.; Martínez-Salas, E. Structural Insights into Viral IRES-dependent Translation Mechanisms. *Current Opinion in Virology* **2015**, *12*, 113–120.

125. Kieft, J. S.; Zhou, K.; Jubin, R.; Doudna, J. A. Mechanism of Ribosome Recruitment by Hepatitis C IRES RNA. *RNA* **2001**, *7*, 194–206.

126. Kerr, C. H.; Jan, E. Commandeering the Ribosome: Lessons Learned from Dicistroviruses about Translation. *Journal of Virology* **2016**, *90*, 5538–5540.

127. Ji, H.; Fraser, C. S.; Yu, Y.; Leary, J.; Doudna, J. A. Coordinated Assembly of Human Translation Initiation Complexes by the Hepatitis C Virus Internal Ribosome Entry Site RNA. *Proc Natl Acad Sci U S A* **2004**, *101*, 16990–5.

128. Jan, E.; Sarnow, P. Factorless Ribosome Assembly on the Internal Ribosome Entry Site of Cricket Paralysis Virus. *J Mol Biol* **2002**, *324*, 889–902.

129. Steinberg, S.; Stefansson, H.; Jonsson, T.; Johannsdottir, H.; Ingason, A. et al. Loss-of-Function Variants in ABCA7 Confer Risk of Alzheimer's Disease. *Nat Genet* **2015**, *47*, 445–7.

130. Pisarev, A. V.; Chard, L. S.; Kaku, Y.; Johns, H. L.; Shatsky, I. N. et al. Functional and Structural Similarities between the Internal Ribosome Entry Sites of Hepatitis C Virus and Porcine Teschovirus, a Picornavirus. *J Virol* **2004**, *78*, 4487–97.

131. Lukavsky, P. J. Structure and Function of HCV IRES Domains. *Virus Res* **2009**, *139*, 166–71.

132. Cai, Q.; Todorovic, A.; Andaya, A.; Gao, J.; Leary, J. A. et al. Distinct Regions of Human eIF3 Are Sufficient for Binding to the HCV IRES and the 40S Ribosomal Subunit. *J Mol Biol* **2010**, *403*, 185–96.

133. Hashem, Y.; des Georges, A.; Dhote, V.; Langlois, R.; Liao, H. Y. et al. Hepatitis-C-virus-like Internal Ribosome Entry Sites Displace eIF3 to Gain Access to the 40S Subunit. *Nature* **2013**, *503*, 539–43.

134. Easton, L. E.; Locker, N.; Lukavsky, P. J. Conserved Functional Domains and a Novel Tertiary Interaction near the Pseudoknot Drive Translational Activity of Hepatitis C Virus and Hepatitis C Virus-like Internal Ribosome Entry Sites. *Nucleic Acids Res* **2009**, *37*, 5537–49.

135. Imai, S.; Kumar, P.; Hellen, C. U.; D'Souza, V. M.; Wagner, G. An Accurately Preorganized IRES RNA Structure Enables eIF4G Capture for Initiation of Viral Translation. *Nat Struct Mol Biol* **2016**, *23*, 859–64.

136. Chamond, N.; Deforges, J.; Ulryck, N.; Sargueil, B. 40S Recruitment in the Absence of eIF4G/4A by EMCV IRES Refines the Model for Translation Initiation on the Archetype of Type II IRESs. *Nucleic Acids Res* **2014**, *42*, 10373–84.

137. Chance, P. F.; Alderson, M. K.; Leppig, K. A.; Lensch, M. W.; Matsunami, N. et al. DNA Deletion Associated with Hereditary Neuropathy with Liability to Pressure Palsies. *Cell* **1993**, *72*, 143–51.

138. Leppek, K.; Das, R.; Barna, M. Functional 5' UTR mRNA Structures in Eukaryotic Translation Regulation and How to Find Them. *Nat Rev Mol Cell Biol* **2018**, *19*, 158–174.

139. Allen, M.; Lincoln, S. J.; Corda, M.; Watzlawik, J. O.; Carrasquillo, M. M. et al. ABCA7 Loss-of-Function Variants, Expression, and Neurologic Disease Risk. *Neurol Genet* **2017**, *3*, e126.

140. LeProust, E. M.; Peck, B. J.; Spirin, K.; McCuen, H. B.; Moore, B. et al. Synthesis of High-Quality Libraries of Long (150mer) Oligonucleotides by a Novel Depurination Controlled Process. *Nucleic Acids Research* **2010**, *38*, 2522–2540.

141. Gamache, T. R.; Araki, Y.; Huganir, R. L. Twenty Years of SynGAP Research: From Synapses to Cognition. *The Journal of Neuroscience: The Official Journal of the Society for Neuroscience* **2020**, *40*, 1596–1605.

142. Mignot, C.; von Stülpnagel, C.; Nava, C.; Ville, D.; Sanlaville, D. et al. Genetic and Neurodevelopmental Spectrum of SYNGAP1-associated Intellectual Disability and Epilepsy. *Journal of Medical Genetics* **2016**, *53*, 511–522.

143. Creson, T. K.; Rojas, C.; Hwaun, E.; Vaissiere, T.; Kilinc, M. et al. Re-Expression of SynGAP Protein in Adulthood Improves Translatable Measures of Brain Function and Behavior. *eLife* **2019**, *8*, e46752.

144. Paul, C. P.; Good, P. D.; Winer, I.; Engelke, D. R. Effective Expression of Small Interfering RNA in Human Cells. *Nat Biotechnol* **2002**, *20*, 505–8.

145. Komiyama, N. H.; Watabe, A. M.; Carlisle, H. J.; Porter, K.; Charlesworth, P. et al. SynGAP Regulates ERK/MAPK Signaling, Synaptic Plasticity, and Learning in the Complex with Postsynaptic Density 95 and NMDA Receptor. *J Neurosci* **2002**, *22*, 9721–32.

146. Collins, R. L.; Glessner, J. T.; Porcu, E.; Lepamets, M.; Brandon, R. et al. A Cross-Disorder Dosage Sensitivity Map of the Human Genome. *Cell* **2022**, *185*, 3041–3055 e25.

147. Wienert, B.; Shin, J.; Zelin, E.; Pestal, K.; Corn, J. E. In Vitro-Transcribed Guide RNAs Trigger an Innate Immune Response via the RIG-I Pathway. *PLoS Biol* **2018**, *16*, e2005840.

148. Jimenez-Gomez, A.; Niu, S.; Andujar-Perez, F.; McQuade, E. A.; Balasa, A. et al. Phenotypic Characterization of Individuals with SYNGAP1 Pathogenic Variants Reveals a Potential Correlation between Posterior Dominant Rhythm and Developmental Progression. *J Neurodev Disord* **2019**, *11*, 18.

149. Zhang, Y.; Pak, C.; Han, Y.; Ahlenius, H.; Zhang, Z. et al. Rapid Single-Step Induction of Functional Neurons from Human Pluripotent Stem Cells. *Neuron* **2013**, *78*, 785–98.

150. Rocks, O.; Peyker, A.; Kahms, M.; Verveer, P. J.; Koerner, C. et al. An Acylation Cycle Regulates Localization and Activity of Palmitoylated Ras Isoforms. *Science* **2005**, *307*, 1746–1752.

151. Fukata, Y.; Fukata, M. Protein Palmitoylation in Neuronal Development and Synaptic Plasticity. *Nature Reviews Neuroscience* **2010**, *11*, 161–175.

152. Zhang, Y.; Qin, Z.; Sun, W.; Chu, F.; Zhou, F. Function of Protein S-Palmitoylation in Immunity and Immune-Related Diseases. *Frontiers in Immunology* **2021**, *12*, 661202.

153. Rocks, O.; Gerauer, M.; Vartak, N.; Koch, S.; Huang, Z.-P. et al. The Palmitoylation Machinery Is a Spatially Organizing System for Peripheral Membrane Proteins. *Cell* **2010**, *141*, 458–471.

154. Jennings, B. C.; Nadolski, M. J.; Ling, Y.; Baker, M. B.; Harrison, M. L. et al. 2-Bromopalmitate and 2-(2-Hydroxy-5-Nitro-Benzylidene)-Benzo[b]Thiophen-3-One Inhibit DHHC-mediated Palmitoylation in Vitro. *Journal of Lipid Research* **2009**, *50*, 233–242.

155. Webb, Y.; Hermida-Matsumoto, L.; Resh, M. D. Inhibition of Protein Palmitoylation, Raft Localization, and T Cell Signaling by 2-Bromopalmitate and Polyunsaturated Fatty Acids*. *Journal of Biological Chemistry* **2000**, *275*, 261–270.

156. Zheng, B.; DeRan, M.; Li, X.; Liao, X.; Fukata, M. et al. 2-Bromopalmitate Analogues as Activity-Based Probes to Explore Palmitoyl Acyltransferases. *Journal of the American Chemical Society* **2013**, *135*, 7082–7085.

157. Davda, D.; El Azzouny, M. A.; Tom, C. T. M. B.; Hernandez, J. L.; Majmudar, J. D. et al. Profiling Targets of the Irreversible Palmitoylation Inhibitor 2-Bromopalmitate. *ACS chemical biology* **2013**, *8*, 1912–1917.

158. Pedro, M. P.; Vilcaes, A. A.; Tomatis, V. M.; Oliveira, R. G.; Gomez, G. A. et al. 2-Bromopalmitate Reduces Protein Deacylation by Inhibition of Acyl-Protein Thioesterase Enzymatic Activities. *PloS One* **2013**, *8*, e75232.

159. Azizi, S.-A.; Lan, T.; Delalande, C.; Kathayat, R. S.; Banales Mejia, F. et al. Development of an Acrylamide-Based Inhibitor of Protein S-Acylation. *ACS Chemical Biology* **2021**, *16*, 1546–1556.

160. Hong, J. Y.; Malgapo, M. I. P.; Liu, Y.; Yang, M.; Zhu, C. et al. High-Throughput Enzyme Assay for Screening Inhibitors of the ZDHHC3/7/20 Acyltransferases. *ACS Chemical Biology* **2021**, *16*, 1318–1324.

161. Chen, B.; Niu, J.; Kreuzer, J.; Zheng, B.; Jarugumilli, G. K. et al. Auto-Fatty Acylation of Transcription Factor RFX3 Regulates Ciliogenesis. *Proceedings of the National Academy of Sciences* **2018**, *115*, E8403–E8412.

162. Jia, L.; Chisari, M.; Maktabi, M. H.; Sobieski, C.; Zhou, H. et al. A Mechanism Regulating G Protein-Coupled Receptor Signaling That Requires Cycles of Protein Palmitoylation and Depalmitoylation. *The Journal of Biological Chemistry* **2014**, *289*, 6249–6257.

163. Long, J. Z.; Cisar, J. S.; Milliken, D.; Niessen, S.; Wang, C. et al. Metabolomics Annotates ABHD3 as a Physiologic Regulator of Medium-Chain Phospholipids. *Nature chemical biology* **2011**, *7*, 763–765.

164. Charollais, J.; Van Der Goot, F. G. Palmitoylation of Membrane Proteins (Review). *Molecular Membrane Biology* **2009**, *26*, 55–66.

165. Muz, B.; de la Puente, P.; Azab, F.; Azab, A. K. The Role of Hypoxia in Cancer Progression, Angiogenesis, Metastasis, and Resistance to Therapy. *Hypoxia* **2015**, *3*, 83–92.

166. Chen, C.-K.; Cheng, R.; Demeter, J.; Chen, J.; Weingarten-Gabbay, S. et al. Structured Elements Drive Extensive Circular RNA Translation. *Molecular Cell* **2021**, *81*, 4300–4318.e13.

167. Keefe, A. D.; Pai, S.; Ellington, A. Aptamers as Therapeutics. *Nature Reviews Drug Discovery* **2010**, *9*, 537–550.

168. Darmostuk, M.; Rimpelova, S.; Gbelcova, H.; Ruml, T. Current Approaches in SELEX: An Update to Aptamer Selection Technology. *Biotechnology Advances* **2015**, *33*, 1141–1161.

169. Miyakawa, S.; Oguro, A.; Ohtsu, T.; Imataka, H.; Sonenberg, N. et al. RNA Aptamers to Mammalian Initiation Factor 4G Inhibit Cap-Dependent Translation by Blocking the Formation of Initiation Factor Complexes. *RNA* **2006**, *12*, 1825–1834.

170. Childs-Disney, J. L.; Yang, X.; Gibaut, Q. M. R.; Tong, Y.; Batey, R. T. et al. Targeting RNA Structures with Small Molecules. *Nature Reviews Drug Discovery* **2022**, *21*, 736–762.

171. Setten, R. L.; Rossi, J. J.; Han, S. P. The Current State and Future Directions of RNAi-based Therapeutics. *Nat Rev Drug Discov* **2019**, *18*, 421–446.

172. Hou, X.; Zaks, T.; Langer, R.; Dong, Y. Lipid Nanoparticles for mRNA Delivery. *Nature Reviews Materials* **2021**, *6*, 1078–1094.

173. Ochoa, S.; Milam, V. T. Modified Nucleic Acids: Expanding the Capabilities of Functional Oligonucleotides. *Molecules* **2020**, *25*, 4659.

174. Bhattacharyya, J.; Maiti, S.; Muhuri, S.; Nakano, S.-i.; Miyoshi, D. et al. Effect of Locked Nucleic Acid Modifications on the Thermal Stability of Noncanonical DNA Structure. *Biochemistry* **2011**, *50*, 7414–7425.

175. Merkle, T.; Merz, S.; Reautschnig, P.; Blaha, A.; Li, Q. et al. Precise RNA Editing by Recruiting Endogenous ADARs with Antisense Oligonucleotides. *Nat Biotechnol* **2019**, *37*, 133–138.

176. Qu, L.; Yi, Z.; Zhu, S.; Wang, C.; Cao, Z. et al. Programmable RNA Editing by Recruiting Endogenous ADAR Using Engineered RNAs. *Nat Biotechnol* **2019**, *37*, 1059–1069.